Front propagation and mode-locking in Coupled Map Lattices

Ricardo Carretero-González

Thesis submitted for the degree of
Doctor of Philosophy

Supervisors: Dr. F. Vivaldi and Dr. D.K. Arrowsmith
Department of Mathematical Sciences
Queen Mary and Westfield College
August 1997

Front propagation and mode-locking in Coupled Map Lattices

Ph. D. Thesis, R. Carretero-González

Abstract

We study the propagation of coherent signals through bistable one-way and diffusive Coupled Map Lattices (CML). We describe a simple mechanism that allows interfaces to travel along the lattice, without damping or dispersion. This mechanism relies on a non-decreasing bistable local map with two stable fixed points. The state of the lattice is then set as a step state between the stable points and it is seen to advance along the lattice with a well-defined velocity that depends on the coupling parameter ε. For some local maps the velocity is shown to have ε-intervals where it is mode-locked to a rational value.

In order to understand the mode-locking phenomenon we introduce a continuous piece-wise linear local map. We show how the dynamics of the whole lattice (infinite system) may be reduced to a one-dimensional auxiliary map. The auxiliary map is a circle-like map whose rotation number corresponds to the velocity of the travelling interface. We introduce symbolic dynamics to fully understand the mode-locking of the rotation number. We prove that the velocity of the travelling interface has a Devil's staircase (a fractal staircase) dependence on the coupling parameter. The Devil's staircase is mode-locked to rational plateaus and may be fully described via Farey sequences and modular transformations.

Finally we give some numerical examples depicting mode-locking of the velocity for a wider range of couplings and local maps and we study the dependence of plateau sizes on the coupling interaction range. The mode-locking of the velocity in CML allows an interface to travel at a constant speed despite parametric perturbations giving structural stability to the front propagation and is present in a very wide range of CMLs.

Acknowledgments

I am delighted to acknowledge the support and encouragement of many people during the development of my Ph.D. research project.

My deepest gratitude goes to my supervisors Franco Vivaldi and David Arrowsmith for all their help and encouragement during my stay at QMW. They provided me with continuous ideas and feedback towards the development of my research and always found time to discuss any new problems or results. I would also like to thank the examinors P.A. Glendinning and D.A. Rand for providing me with useful comments, corrections and relevant bibliographic material towards the refinement of this manuscript.

I am extremely thankful to Dr. Alvaro Salas Brito and Dr. Noemi Núñez Yépez for their continuous academic and moral support throughout all my undergraduate and postgraduate studies. I would also like to thank Dr. Carmen Cisneros Gudiño for her unconditional support and for sponsoring my application for a DGAPA-UNAM scholarship.

This research would have been impossible to conduct without the financial support of the following bodies. I am very grateful to the Dirección General de Asuntos del Personal Académico (DGAPA), Universidad Nacional Autónoma de México (UNAM) for the award of a scholarship giving me the opportunity to pursue my Ph.D. studies abroad. I would also like to thank the 'Programa de Financiamento Compartido 1993/94' of The British Council for their financial support in paying my first year tuition fees. I also acknowledge the Committee of Vice-Chancellors and Principals, London for the Overseas Research Student (ORS) award which provided partial remission of my tuition fees.

To all the people that I have met in London and thereabouts, all my best regards. In particular, thanks to the people at Arbery Road, especially Christine and Ianis for all the pleasant hours we spent chatting together. The same for you Martin. Thanks to Santi for his friendship and for providing a refuge in Cambridge. To all my football mates, "thumbs up" for the good matches. Thanks to everyone at the Department of Mathematics that made my time at QMW so enjoyable. I particularly wish to thank Vaggelis and Tom for the true friendship they have shown to me and for all the trips, footy matches, nights out, etc. that we have spent, and will continue to spend, together.

To all my UNAM friends, thanks for keeping in touch and for all the mutual visits we have paid each other around the globe.

Thanks to the Spanish-speaking bunch that I have met in London. To Xochitl and Tostado, Gerardo O., Gerardo Ivar, Diana, Marc, Dan, Brita, Juan, Raul and Axa-power for all the lunches, meals and parties we have been to together. Without you guys it would not have been the same...

I would like to thank my family for their continuing love and support despite our being on opposite sides of the Atlantic.

I would especially like to thank Alexandra for everything we have shared. You have been an endless source of inspiration and an invaluable friend, not only during my Ph.D., but throughout all my independent life. I have fully enjoyed all the time we have spent in London and travelling all over Europe. Te amo.

Ricardo Carretero

Contents

0 Introduction **11**

1 Homogeneous states **15**

1.1 Homogeneous states and their stability 15

1.2 Stability of homogeneous states in one-way CMLs 16

1.3 Stability of homogeneous states in diffusive CMLs 19

1.4 Stability of periodic homogeneous states 21

2 Localized states and propagating fronts **23**

2.1 Localized states 23

2.2 Travelling velocity and basic properties 26

3 Travelling wave fronts **33**

3.1 A bistable local map f 33

3.2 Travelling wave fronts in one-way CMLs 35

3.3 Travelling wave fronts in diffusive CMLs 38

3.4 Mode-locking of the travelling velocity 45

4 A piece-wise linear local map **47**

4.1 The piece-wise linear local map 47

4.2 The auxiliary map and its symbolic dynamics 52

4.2.1 The auxiliary map for an increasing step state 52

4.2.2 The auxiliary map for a decreasing step state 58

4.2.3 Symbolic dynamics of minimal 1-states 58

4.3 The travelling velocity 62

4.3.1 Existence of the travelling velocity 62

4.3.2 Continuity of the travelling velocity 65

4.3.3 The travelling velocity is non-decreasing 66

4.3.4 The velocity tree 66

4.4 Mode-locking of the auxiliary map 68

4.4.1 Mode-locking 68

4.4.2 Linear stability of periodic non gap orbits 73

4.4.3 Stability diagram of the auxiliary map 75
4.4.4 Velocity in the zero-gap case 77
4.5 Representing the velocity tree with an integral lattice 80
4.5.1 The integral lattice 80
4.5.2 Concatenating sequences using the lattice representation 84
4.5.3 Concatenating a family of sequences 87
4.5.4 Unimodular transformations and envelopes 87

5 Higher order interface dynamics **93**
5.1 High order dynamics of minimal states 93
5.1.1 Convergence to minimal states 93
5.1.2 Two-dimensional auxiliary map 96
5.1.3 The tongues for the two-dimensional case 98
5.1.4 Higher order dynamics 102
5.2 Mode-locking for smooth maps 105
5.2.1 Mode-locking in one-way CMLs 105
5.2.2 Mode-locking in diffusive CMLs 108
5.3 Width of the mode-locking plateaus 110
5.3.1 Mode-locking versus number of sites in the interface 112
5.3.2 Mode-locking versus range of interaction 116

6 Conclusions and final remarks **121**

List of Figures

1.1 Homogeneous regions outside the localized zones 15
1.2 Eigenvalues for the linear stability of a fixed homogeneous state 18

2.1 The position of the centre of mass μ increases with ε 28

3.1 A bistable continuous map f 34
3.2 Evolution of an initial minimal mass step state for zero coupling 34
3.3 Competing dynamics in the interface in a one-way CML 35
3.4 Travelling step state and kink in a one-way CML 36
3.5 Velocity of the front in a one-way CML with cubic local map 37
3.6 The family of cubic local maps used in the one-way CML 38
3.7 ε_c vs. the derivative at the unstable point 39
3.8 The stationary front shape in a diffusive CML 40
3.9 The rescaled stationary profiles 40
3.10 Front velocity in a diffusive CML with a non-symmetric map 42
3.11 Travelling direction of an interface in a diffusive CML 43
3.12 Propagating kink in an asymmetric diffusive CML 44
3.13 The hyperbolic tangent local map 45
3.14 Velocity in a one-way CML with the hyperbolic tangent local map 46

4.1 The piece-wise linear local map $f_a(x)$ 47
4.2 Velocity curves for the piece-wise linear local map 48
4.3 Reduction of minimal mass states 49
4.4 The interface of a minimal mass step state 49
4.5 Reduction of X_{t+1} with 4 different cases 51
4.6 The maps f_0 and f_1 51
4.7 Two sites entering the unstable regime 53
4.8 The (ε, a)-region where the gap is non-negative 54
4.9 Dynamics of minimal 1-states when $\varepsilon < \varepsilon_c$ 55
4.10 The 3 possibilities of evolution of a minimal 1-state. 56
4.11 The auxiliary map $\Phi_{\varepsilon,a}$ 57

4.12 Reduction of the dynamics for minimal 1-states 57
4.13 The auxiliary map $\Upsilon_{\varepsilon,a}$ 58
4.14 Symbolic dynamics of the auxiliary map 59
4.15 Symbolic dynamics for an orbit of the auxiliary map 59
4.16 Symbolic dynamics for a periodic orbit of the auxiliary map 61
4.17 Lift of the auxiliary map 62
4.18 If $\varepsilon' > \varepsilon$ then $\Upsilon_{\varepsilon',a}(x) \geq \Upsilon_{\varepsilon,a}(x)$ 66
4.19 Velocity tree 67
4.20 Parameter space regions where $v = 0, 1, 1/2$ 68
4.21 Period 5 orbit of the auxiliary map 69
4.22 Parametric stability of a gap orbit 70
4.23 Velocity of the travelling interface for $a = 2/5$ 70
4.24 Mode-locking region for $v = 2/5$. 71
4.25 Arnold's tongues in the (ε, a)-plane 72
4.26 Unstable region for a periodic non gap orbit 73
4.27 Examples of unstable regions for periodic non gap orbits 74
4.28 Bifurcation diagram of the auxiliary map for constant a 76
4.29 Paths in the parameter space for the bifurcation diagrams 77
4.30 Bifurcation diagram of the auxiliary map for constant γ 78
4.31 The auxiliary map $\Phi'_{\varepsilon,a}$ 79
4.32 Velocity curve for the zero-gap case 80
4.33 The Farey tree 81
4.34 There exists many different possible paths in the integral lattice 82
4.35 The correct path in the integral lattice giving the coding sequence 83
4.36 Another method giving the correct path in the integral lattice 83
4.37 The symbolic sequence for the mediant 84
4.38 Upper and lower envelopes for $v(\varepsilon, a = 0.4)$ 90

5.1 The discretization induces a changing number of interfacial sites 94
5.2 Sites belonging to the interface 94
5.3 Minimal N-states layers in the parameter space 95
5.4 Any initial condition tends to a minimal N-state 96
5.5 Possible evolution combinations of a minimal 2-state 97
5.6 The auxiliary map Ω for the two-dimensional case 97
5.7 Tree sites entering in the interface 98
5.8 Plot of $\Omega_1(x_1, x_2)$ and $\Omega_2(x_1, x_2)$ for $(\varepsilon, a) = (0.365, 0.7)$ 99
5.9 The two possible orbits giving $v = 1/2$ in the two-dimensional case 100

5.10 The $v = 1/2$ tongues in the minimal 2-state layer 101
5.11 Principal mode-locking tongues in the minimal 2-state layer 101
5.12 Tongues in the high dimensional minimal N-state layers 103
5.13 Successive states of the lattice in the $v = 1/3$ tongue 104
5.14 Bifurcation diagram of the interfacial sites in the $v = 1/3$ tongues 105
5.15 Arnold's tongues for the hyperbolic tangent local map 106
5.16 Velocity curve for the hyperbolic tangent local map with $\nu = 2/5$ 106
5.17 Enlargement around $v = 1/3$ for the hyperbolic local map 107
5.18 Taking an ε-value near a mode-locking plateau 108
5.19 Delay map of the central site for the hyperbolic tangent local map 109
5.20 The second iterate of the logistic map 109
5.21 Velocity for the second iterate of the logistic map in a diffusive CML 110
5.22 Enlargement of the velocity for the second iterate of the logistic map 111
5.23 Delay map for the logistic local map in a diffusive CML 112
5.24 Number of interfacial sites for the hyperbolic tangent local map 113
5.25 Width of the travelling interface for the hyperbolic tangent local map 113
5.26 Size of the $v = 1/3$ plateau as a function of ν 114
5.27 Size of the $v = 1/3$ plateau for small ν using more iterations 115
5.28 The hyperbolic tangent tends to a square step function 115
5.29 Restriction on the dynamics as the interfacial domain is increased 116
5.30 Number of sites in the interface vs. the range of the coupling 116
5.31 Number of sites in the interface vs. coupling parameters 117
5.32 Effect of N_l onto the mode-locked plateaus 118

Chapter 0

Introduction

An interesting feature of coupled map lattices [1, 2] is the widespread occurrence of the so-called *spatio-temporal chaos* [3, 4], which is irregular behaviour in space as well as time. Equally interesting is the appearance of coherent structures from an apparently decorrelated medium [5, 6, 7]. For example, an interface separating two different phases may travel along the lattice [8, 9, 10, 11]. The movement of such a front depends on the strength of the coupling between lattice sites. This work is concerned with investigating some aspects of this phenomenon, in particular the mode-locking of the travelling velocity for some coupling parameter intervals.

Let us start by defining a coupled map lattice. Consider an infinite, one-dimensional, collection of cells with a local dynamical variable $x_t(i)$, characterizing the state of the i-th cell at time t. Both i and t are integers. The state of the lattice at time t is given by the state vector

$$X_t = \{x_t(i)\} = (\ldots, x_t(i-1), x_t(i), x_t(i+1), \ldots). \tag{0.1}$$

The function that gives the state of the i-th cell at time $t+1$ as a function of the state (0.1) is given by

$$x_{t+1}(i) = F_i(\ldots, x_t(i-1), x_t(i), x_t(i+1), \ldots), \tag{0.2}$$

where the function F_i contains the information of the local dynamics in each cell as well of the interaction between them. Equation (0.2) gives the components of the global map $\mathbf{F}$:

$$\mathbf{F} = (\ldots, F_{-1}, F_0, F_1, \ldots) \qquad X_{t+1} = \mathbf{F}(X_t).$$

The global map $\mathbf{F}$ is then called a *coupled map lattice* (CML). We introduce here one-dimensional CMLs but the model may be easily generalized to higher dimensions. A CML is then a dynamical system with discrete time, discrete space and continuous state. In contrast with CMLs, cellular automata (CA) have discrete time, discrete space and *discrete* state, thus we could think that CMLs are an extension of CA to continuous state. Moreover, the phenomenology of CA and CMLs could be extremely similar and one may even try to use CMLs instead of CA [12, 13].

We consider *homogeneous* CMLs, so that the map $F_i = F$ is the same for all cells and therefore the evolution of the lattice is given by

$$x_{t+1}(i) = F(\ldots, x_t(i-1), x_t(i), x_t(i+1), \ldots). \tag{0.3}$$

A physically meaningful interaction will have typically a limited range, with decreasing strength for distant neighbours. Coupling l left neighbours and r right neighbours gives the general formula

$$x_{t+1}(i) = (1-\varepsilon) f_i(x_t(i)) + \sum_{\substack{k=-l \\ k\neq 0}}^{r} \varepsilon_k f_{i+k}(x_t(i+k)), \tag{0.4}$$

where f_i are real, one-dimensional, maps. Typically one asks that $\sum \varepsilon_k = \varepsilon$ as a conservation law, since failure to do so may lead to non-boundedness of the state as time tends to infinity. The coefficients ε_k are called the *coupling parameters* and they define the weight that every neighbour is contributing towards the coupling sum. The neighbouring coupling switches the exchange of 'information' between sites. The coupling parameter must satisfy $0 \leq \varepsilon \leq 1$ in order to maintain the same sign of the information exchange.

The CML (0.4) may be seen as acting in two separate stages: firstly with the so called *local dynamics* (or *local maps*) via the real maps f_i and secondly with the *coupling dynamics* in terms of the weighted sum. The model (0.4) reflects a non-homogeneous coupling dynamics because the maps f_i could be different. Since we are interested in the study of signal propagation through the lattice, a more reasonable model would have an homogeneous dynamics permitting the signal to travel coherently, therefore we choose the maps f_i to be all identical to f. The dynamics of the CML is then reduced to the *local map* f plus the coupling interaction. The simplest interactions, nearest neighbours, give

$$x_{t+1}(i) = (1-\varepsilon) f(x_t(i)) + \frac{\varepsilon}{2}\left(f(x_t(i-1)) + f(x_t(i+1))\right) \tag{0.5}$$

and

$$x_{t+1}(i) = (1-\varepsilon) f(x_t(i)) + \varepsilon f(x_t(i-1)), \tag{0.6}$$

which are called *diffusive* and *one-way* CML respectively. The diffusive CML corresponds to a nearest neighbour interaction including, with the same weight, the left and the right neighbours giving a non-preferential propagating direction. The term diffusive comes from the analogy with the partial differential equation for diffusion [14], where the second spatial derivative of the dynamical variable may be approximated, by applying a finite difference method, to $x_t(i-1) - 2x_t(i) + x_t(i+1)$ and by rewriting (0.5) as

$$x_{t+1}(i) = f(x_t(i)) + \frac{\varepsilon}{2}\left(f(x_t(i-1)) - 2f(x_t(i)) + f(x_t(i+1))\right)$$

one sees the similarity, and thus, the parameter ε is often called the *diffusive parameter*. The direction of information of propagation in a diffusive CML is determined by the local map since the coupling is symmetrical. On the other hand, the one-way CML couples sites with their left neighbours only, giving a preferred travelling direction: from left to right.

Equations (0.5) and (0.6) are the most widespread models of CML and they only contain a single coupling parameter value ε. The CMLs were introduced by Kaneko [15, 16] as a paradigm for the study of fully-developed turbulence and pattern formation. Since then, CMLs have been used in a very wide range of subjects such as: chemical interfaces [8], traffic flow [17], sea scattering [18], patch population dynamics [19, 20], extended ecosystems [21, 22], cardiac tissue [23], AIDS genetic evolution [24, 25], computational systems [26], convection [27], turbulent flows [28, 29], open flows [30, 31], etc.

In this work we consider the propagation of localized wave fronts along diffusive and one-way CMLs. In chapter 1 we establish the linear stability of homogeneous states and

periodic ones. Chapter 2 is dedicated to the precise definitions of localized states and step states (localized wave fronts) and to establish some of their basic properties. In chapter 3 a simple mechanism, a bistable local map, is introduced enabling us to propagate wave fronts in a coherent way along the lattice in both, diffusive and one-way, CMLs. The first examples of mode-locking of the velocity are shown. Chapter 4 is devoted towards the complete understanding of the mode-locking of the velocity, in order to do so, we study a one-parameter family of piece-wise linear local maps for a one-way CML. We find that the dynamics of the whole lattice may be reduced to a one-dimensional circle-like map, allowing us to reduce the dynamics from a potentially infinite system to a one-dimensional one. For this particular piece-wise linear local map it is possible to show that the velocity of the travelling wave front is equivalent to the rotation number of the auxiliary map for the particular case when only one site is in the interfacial zone. We show that for each value of the parameters the velocity of the interface is well-defined, and we use it to characterize the structure of the parameter space. The travelling velocity is found to be mode-locked to rational values. Moreover we show that the graph of the velocity as a function of the coupling parameter is a fractal staircase —a Devil's staircase. Using symbolic dynamics on the auxiliary map one can code the plateaus of the Devil's staircase by hierarchies and find the envelopes for every family of plateaus. The self-similar structure of the Devil's staircase is then unveiled by means of the Farey series and unimodular transformations via their envelopes.

In chapter 5 we present the mode-locking phenomenon with the piece-wise linear map when more than one site is in the interface. The CML is then reduced to a N-dimensional system, where N is the number of sites in the interface and a similar mode-locking phenomenon occurs in this case. We depict several examples of diffusive and one-way CMLs with smooth local maps where the mode-locking structure prevails. Furthermore, we explain how mode-locking is affected —the parametric domains where the velocity is mode-locked decrease in size— as the range of the coupling is increased. In the limit where the coupling range tends to infinity, that is when we tend to a spatially continuous system, the width of the plateaus tends to zero. However, the evidence presented in this work should support the conclusion that the mode-locking phenomenon of travelling wave fronts in CML is the rule rather than the exception. The mode-locking of the travelling front with respect to the system parameters —coupling parameters and local map parameters— provides structural stability emphasizing the fact that the front propagation is stable under external perturbations.

Chapter 1

Homogeneous states

Before analyzing in detail the propagation of signals through the lattice it is important to study the existence and stability of homogeneous states. This is because a travelling front must be localized in some sense (cf. next chapter for precise definitions) and then must have homogeneous ('flat') regions (cf. figure 1.1) outside of the localized region. We shall therefore address this chapter to the study of fixed homogeneous states and we generalize the results for homogeneous periodic orbits.

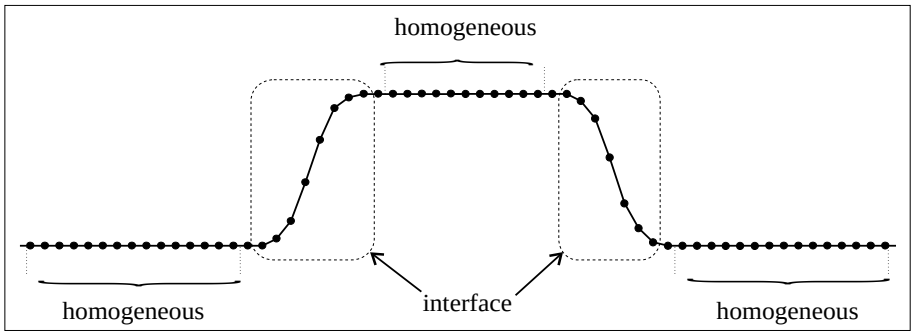

Figure 1.1: For a travelling front, outside of the localized regions, the lattice is homogeneous.

In the case of uncoupled sites ($\varepsilon = 0$), the dynamics of a local state —the state in a single lattice point— is completely determined by the initial condition and the local map f at that site, and it is totally independent from what is happening at all the other sites. Thus the dynamics when $\varepsilon = 0$ reduces to the study of the one-dimensional map f at each lattice point. When the coupling parameter ε is non-zero the interaction between sites enriches the dynamics, and a local fixed point (a fixed point of f) may not exist anymore or change its stability for the whole configuration of the lattice. In this section we focus our attention to the study of states of the whole lattice that are homogeneous.

1.1 Homogeneous states and their stability

The simplest of all CML states is the *homogeneous state*, that is a state $X_t = \{x_t(i)\}$ that has the same configuration at all lattice points, *i.e.* $x_t(i) = x_t \ \forall i$. Let us consider the following

quite general model of CML:

$$x_{t+1}(i) = (1-\varepsilon)f(x_t(i)) + \sum_{\substack{k=-l \\ k\neq 0}}^{r} \varepsilon_k f(x_t(i+k)) \tag{1.1}$$

such that $\sum \varepsilon_k = \varepsilon$ as a conservation law. Equation (1.1) couples l left neighbours and r right neighbours with coefficients ε_k.

Suppose we set up the initial configuration of the lattice such that all the sites have the same value $x_0(i) = x_0$, and start iterating the CML. After one iteration, the state at every lattice is

$$\begin{aligned} x_1(i) &= (1-\varepsilon)f(x_0(i)) + \sum_{\substack{k=-l \\ k\neq 0}}^{r} \varepsilon_k f(x_0(i+k)) \\ &= (1-\varepsilon)f(x_0) + f(x_0) \sum_{\substack{k=-l \\ k\neq 0}}^{r} \varepsilon_k \\ &= (1-\varepsilon)f(x_0) + \varepsilon f(x_0) \\ &= f(x_0). \end{aligned}$$

Therefore if we start with an homogeneous state $X_0 = \{x_0\}$ the state of the lattice at any consecutive time t will be homogeneous and equal to $X_t = \{f^t(x_0)\}$. In particular this is true for the one-way (0.6) and diffusive (0.5) CML.

Now suppose that x^* is a fixed point of the local map f, $f(x^*) = x^*$, and that the initial state of the lattice is homogeneous and equal to x^*. Then the whole configuration of the lattice will remain $X_t = \{x^*\}$ at any time, *i.e.* we have a homogeneous fixed state. The main question now concerns the stability of such homogeneous states: does the stability of f at x^* determines the stability of the homogeneous state? The answer turns out to be yes. Let us perform the linear stability analysis for the one-way and diffusive CMLs.

1.2 Stability of homogeneous states in one-way CMLs

We consider the case of periodic boundary conditions, but the main stability result is not altered if we take an infinite lattice. We write the one-way CML in matrix form for a lattice of N sites:

$$X_{t+1} = J_1 \cdot X_t \tag{1.2}$$

with

$$J_1 = \begin{pmatrix} (1-\varepsilon)f & 0 & \cdots & \varepsilon f \\ \varepsilon f & (1-\varepsilon)f & \cdots & 0 \\ \vdots & \ddots & \ddots & \vdots \\ 0 & \cdots & \varepsilon f & (1-\varepsilon)f \end{pmatrix}. \tag{1.3}$$

In order to find the stability of (1.2) for the homogeneous state $\{x^*\}$ one has to find the eigenvalues of the linearized mapping J_1' of J_1 at x^*:

$$J_1' = \begin{pmatrix} (1-\varepsilon)f'(x^*) & 0 & \cdots & \varepsilon f'(x^*) \\ \varepsilon f'(x^*) & (1-\varepsilon)f'(x^*) & \cdots & 0 \\ \vdots & \ddots & \ddots & \vdots \\ 0 & \cdots & \varepsilon f'(x^*) & (1-\varepsilon)f'(x^*) \end{pmatrix}$$

$$= f'(x^*) \begin{pmatrix} 1-\varepsilon & 0 & \cdots & \varepsilon \\ \varepsilon & 1-\varepsilon & \cdots & 0 \\ \vdots & \ddots & \ddots & \vdots \\ 0 & \cdots & \varepsilon & 1-\varepsilon \end{pmatrix}.$$

The eigenvalues λ of J_1' are found by solving the characteristic equation $|J_1' - \lambda \mathbf{1}_N)|=0$, where we denote $|\cdot|$ as the determinant and $\mathbf{1}_N$ is the $N \times N$ unit matrix. To this end, define the matrix

$$M \equiv \frac{(J_1' - \lambda \mathbf{1}_N)}{\varepsilon f'(x^*)}.$$

Letting

$$\alpha \equiv \frac{(1-\varepsilon) - \dfrac{\lambda}{f'(x^*)}}{\varepsilon}$$

gives a simple form for M:

$$M = \begin{pmatrix} \alpha & 0 & \cdots & 1 \\ 1 & \alpha & \cdots & 0 \\ \vdots & \ddots & \ddots & \vdots \\ 0 & \cdots & 1 & \alpha \end{pmatrix}.$$

The case $\alpha = 0$ is trivial: all the eigenvalues are equal to one and the homogeneous state is marginally unstable. For the non-trivial case, requiring $\alpha \neq 0$ and by repeated addition of $(-1)^k(1/\alpha^k)$ times the $(N+1-k)$-th row to the first row we end up with the diagonalized matrix

$$M' = \begin{pmatrix} \alpha + \frac{(-1)^{N-1}}{\alpha^{N-1}} & 0 & \cdots & 0 \\ 1 & \alpha & \cdots & 0 \\ \vdots & \ddots & \ddots & \vdots \\ 0 & \cdots & 1 & \alpha \end{pmatrix},$$

whose eigenvalues satisfy

$$\alpha^{N-1}\left(\alpha + \frac{(-1)^{N-1}}{\alpha^{N-1}}\right) = 0$$

$$\Rightarrow \quad \alpha^N = (-1)^N.$$

Note that the solution $\alpha = 0$ is discarded since we required $\alpha \neq 0$, and therefore the eigenvalues of M' are the N-th roots of (-1) given by $\{\exp(\pi + 2(k-1)\pi/N)\}_{k=1,\ldots,N}$. Thus, the

eigenvalues λ_k of J_1' satisfy

$$\frac{(1-\varepsilon) - \dfrac{\lambda_k}{f'(x^*)}}{\varepsilon} = \exp(\pi + \frac{2(k-1)\pi}{N}),$$

and hence,

$$\begin{aligned} \lambda_k &= f'(x^*)\left((1-\varepsilon) - \varepsilon(\cos(\pi + 2(k-1)\pi/N) + i\sin(\pi + 2(k-1)\pi/N))\right) \\ &= f'(x^*)\left((1-\varepsilon) + \varepsilon(\cos(2(k-1)\pi/N) + i\sin(2(k-1)\pi/N))\right). \end{aligned} \tag{1.4}$$

The geometrical representation of the eigenvalues λ_k is that they form the vertices of the regular N-polygon centered at $(1-\varepsilon)f'(x^*)$ of radius $\varepsilon f'(x^*)$ with the first vertex located at the point $f'(x^*)$. In figure 1.2 we have the eigenvalues in the complex plane for $N = 6$; note that we rescale the figure by the factor $f'(x^*)$.

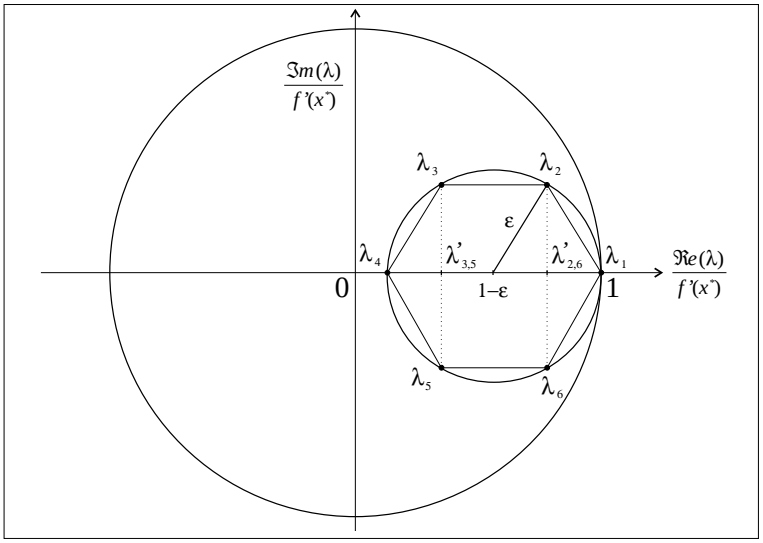

Figure 1.2: Eigenvalues for the linear stability analysis of a fixed homogeneous state in a one-way (λ_k) and a diffusive (λ_k') CML. The eigenvalues for the diffusive case are the real part of the eigenvalues for the one-way case. The modulo for all the eigenvalues is at most $f'(x^*)$, so if the fixed point x^* of the local map f is stable so is the homogeneous fixed state.

It should be clear from the geometrical representation that if $f'(x^*) < 1$ then all the eigenvalues have modulus less than 1. In fact, by construction, all the eigenvalues satisfy

$$|\lambda_k| \leq \left|f'(x^*)\right|. \tag{1.5}$$

Therefore we have proved the following result for the stability of homogeneous states in one-way CML.

Theorem 1.2.1 *An homogeneous state $X_t = \{x^*\}$ of a one-way CML is linearly stable provided that the fixed point x^* is linearly stable for the local map f.*

1.3 Stability of homogeneous states in diffusive CMLs

For a diffusive CML the stability analysis may be performed by a similar diagonalization of the corresponding linearized mapping. However we give here an alternative proof, by relating the eigenvalues of the diffusive CML to the ones of the one-way CML.

The dynamics of a diffusive CML may be written in a matrix form as

$$X_{t+1} = J_2 \cdot X_t \tag{1.6}$$

with

$$J_2 = \begin{pmatrix} (1-\varepsilon)f & (\varepsilon/2)f & 0 & \cdots & (\varepsilon/2)f \\ (\varepsilon/2)f & (1-\varepsilon)f & (\varepsilon/2)f & \cdots & 0 \\ \vdots & \ddots & \ddots & \ddots & \vdots \\ 0 & 0 & \cdots & (1-\varepsilon)f & (\varepsilon/2)f \\ (\varepsilon/2)f & 0 & \cdots & (\varepsilon/2)f & (1-\varepsilon)f \end{pmatrix}, \tag{1.7}$$

whose linearization about the fixed $x = x^*$ point gives

$$J_2' = \begin{pmatrix} (1-\varepsilon)f'(x^*) & (\varepsilon/2)f'(x^*) & 0 & \cdots & (\varepsilon/2)f'(x^*) \\ (\varepsilon/2)f'(x^*) & (1-\varepsilon)f'(x^*) & (\varepsilon/2)f'(x^*) & \cdots & 0 \\ \vdots & \ddots & \ddots & \ddots & \vdots \\ 0 & 0 & \cdots & (1-\varepsilon)f'(x^*) & (\varepsilon/2)f'(x^*) \\ (\varepsilon/2)f'(x^*) & 0 & \cdots & (\varepsilon/2)f'(x^*) & (1-\varepsilon)f'(x^*) \end{pmatrix}.$$

Let us now establish a relation between J_1' and J_2' using permutation matrices. Let us define P_N^+ to be the right permutation $N \times N$ matrix and P_N^- the left permutation matrix. The matrices have the following form

$$P_N^+ = \begin{pmatrix} 0 & 1 & 0 & \cdots & 0 \\ 0 & 0 & 1 & \cdots & 0 \\ \vdots & \ddots & \ddots & \ddots & \vdots \\ 0 & 0 & \cdots & 0 & 1 \\ 1 & 0 & \cdots & 0 & 0 \end{pmatrix}$$

$$P_N^- = \begin{pmatrix} 0 & 0 & 0 & \cdots & 1 \\ 1 & 0 & 0 & \cdots & 0 \\ \vdots & \ddots & \ddots & \ddots & \vdots \\ 0 & 0 & \cdots & 0 & 0 \\ 0 & 0 & \cdots & 1 & 0 \end{pmatrix},$$

that is $\{P_N^+\}_{ij} = \delta_{i,j-1}$ and $\{P_N^-\}_{ij} = \delta_{i,j+1}$, where δ is the Kronecker delta modulo N. The effect of these permutation matrices on a periodic lattice of N sites, is to permute cyclically (shift with periodic boundary conditions) to the right (P_N^+) or to the left (P_N^-) the whole lattice.

Using the permutation matrices it is easy to rewrite the stability matrices as

$$\begin{aligned} \tilde{J}'_1 &= (1-\varepsilon)\mathbf{1}_N + \varepsilon P \\ \tilde{J}'_2 &= (1-\varepsilon)\mathbf{1}_N + \varepsilon\frac{(P+P^{-1})}{2}, \end{aligned} \tag{1.8}$$

where, in order to simplify the notation, we have normalized the stability matrices $\tilde{J}'_{1,2} \equiv J'_{1,2}/f'(x^*)$, redefined $P \equiv P_N^-$ and used the fact that $(P_N^-)^{-1} = P_N^+$.

Let us introduce the operator $Eig(M)$ that gives the eigenvalues of the matrix M. With this notation the eigenvalues of the stability matrices are

$$\begin{aligned} Eig(\tilde{J}'_1) &= Eig\left[(1-\varepsilon)\mathbf{1}_N + \varepsilon P\right] \\ Eig(\tilde{J}'_2) &= Eig\left[(1-\varepsilon)\mathbf{1}_N + \varepsilon\frac{(P+P^{-1})}{2}\right]. \end{aligned} \tag{1.9}$$

On the other hand, the eigenvalues of P are the solutions of

$$|P - \mathbf{1}_N\lambda| = 0, \tag{1.10}$$

that after transposing reads

$$\left|P^\dagger - \mathbf{1}_N^\dagger\lambda\right| = 0 \tag{1.11}$$

but $\mathbf{1}_N^\dagger = \mathbf{1}_N$ and because $|P| = 1$ we have that $P^{-1} = P^\dagger$. Thus eq. (1.11) reads

$$\left|P^{-1} - \mathbf{1}_N\lambda\right| = 0. \tag{1.12}$$

Multiplying (1.10) and (1.12) yields

$$\begin{aligned} & |P - \mathbf{1}_N\lambda|\left|P^{-1} - \mathbf{1}_N\lambda\right| = 0 \\ \Rightarrow\ & \left|PP^{-1} - \lambda P^{-1} - \lambda P + \mathbf{1}_N\lambda^2\right| = 0 \\ \Rightarrow\ & |2\lambda|\left|\tfrac{\frac{1}{\lambda}+\lambda}{2}\mathbf{1}_N - \frac{(P+P^{-1})}{2}\right| = 0 \\ \Rightarrow\ & \left|\Re e(\lambda)\mathbf{1}_N - \frac{(P+P^{-1})}{2}\right| = 0, \end{aligned} \tag{1.13}$$

where we use the fact that the eigenvalues of the permutation matrices have modulus equal to one and thus it is easy to show that $((1/\lambda)+\lambda)/2 = \Re e(\lambda)$, where $\Re e(\lambda)$ denotes the real part of λ. The last equation of (1.13) now reads

$$Eig\left(\frac{(P+P^{-1})}{2}\right) = \Re e(Eig(P)). \tag{1.14}$$

Using (1.14) in (1.9) we finally obtain an equation that relates the eigenvalues of the one-way case to the diffusive one:

$$\begin{aligned} & Eig(\tilde{J}'_2) &&= \Re e(Eig(\tilde{J}'_1)) \\ \Rightarrow\ & Eig(J'_2) &&= \Re e(Eig(J'_1)) \\ \Rightarrow\ & \lambda'_k &&= \Re e(\lambda_k) \\ & &&= f'(x^*)\,\Re e\,[(1-\varepsilon) + \varepsilon(\cos(2(k-1)\pi/N) \\ & &&\quad + i\,\sin(2(k-1)\pi/N))], \end{aligned} \tag{1.15}$$

where we denote by λ'_k the eigenvalues of the stability matrix J'_2. Therefore taking the real part of the eigenvalues of the stability matrix, for the homogeneous case of a one-way CML, gives the eigenvalues for the diffusive CML case. This gives a simple way of relating the the stability of the two models. As an illustration we depict the eigenvalues of both the diffusive CML and the one-way CML for $N = 6$ in figure 1.2.

Again it is straightforward to show (cf. (1.5)) that the eigenvalues for the stability of homogeneous states in diffusive CML satisfy

$$|\lambda'_k| = |\Re e(\lambda_k)| \leq |f'(x^*)|\,. \tag{1.16}$$

Hence we have the theorem for the stability of homogeneous states in diffusive CML:

Theorem 1.3.1 *A homogeneous state $X_t = \{x^*\}$ of a diffusive CML is linearly stable provided that the fixed point x^* is linearly stable for the local map f.*

1.4 Stability of periodic homogeneous states

Up to now we have given the conditions for homogeneous fixed states to be stable in both one-way and diffusive CML. There are however other forms of homogeneous states, like periodic homogeneous states or even more complex states like the spatially periodic ones. We first address the question of stability of periodic homogeneous states.

Consider a periodic orbit $(x_0, x_1, \ldots, x_p = x_0)$ of period p of the local map f and construct the periodic homogeneous state $X_t = \{x_t\}$. In this case the stability matrices $J'_{1,2}(X)$ for the periodic homogeneous state are given by the multiplication of the stability matrices $J'_{1,2}(x_i)$ along the periodic orbit. Recall that the subscripts 1 and 2 correspond to the one-way CML and the diffusive CML respectively. Therefore,

$$\begin{aligned} J'_{1,2}(X) &= \prod_{i=1}^{p} J'_{1,2}(x_i) \\ &= \eta \prod_{i=1}^{p} \tilde{J}'_{1,2}(x_i) \\ \Rightarrow \quad \tilde{J}'_{1,2}(X) &= \prod_{i=1}^{p} \tilde{J}'_{1,2}(x_i), \end{aligned}$$

where again we are using the normalized matrices $\tilde{J}'_{1,2}(x_i) = J'_{1,2}(x_i)/f'(x_i)$ and we define the global normalized stability matrix $\tilde{J}'_{1,2}(X) \simeq J'_{1,2}(X)/\eta$ with $\eta \equiv \prod_{i=1}^{p} f'(x_i)$ being the multiplier of the periodic orbit of the local map f. A closer inspection to the matrices $\tilde{J}'_{1,2}(x_i)$ reveals that they do not depend anymore on the orbit since the factors $f'(x_i)$ have been absorbed by the normalization, thus the matrices $\tilde{J}'_{1,2}(x_i)$ are exactly the same matrices $\tilde{J}'_{1,2}$ defined in (1.8). Therefore the global stability matrices reduces to

$$\tilde{J}'_{1,2}(X) = \left(\tilde{J}'_{1,2}\right)^p,$$

and because $Eig\left((\tilde{J}'_{1,2})^p\right) = \left(Eig(\tilde{J}'_{1,2})\right)^p$, the eigenvalues for the homogeneous periodic state are

$$Eig(J'_{1,2}(X)) = \eta \left(Eig(J'_{1,2})\right)^p . \tag{1.17}$$

Consider again the geometrical representation of the eigenvalues (cf. figure 1.2), the eigenvalues of $J'_{1,2}(X)$ fall again in the circle of radius ε centered at $1-\varepsilon$ (but they are rotated w.r.t. the ones of $J'_{1,2}$ because of the power p in (1.17)) with a rescaling factor of η instead of $f'(x^*)$. Thus if the multiplier of the periodic orbit η is less than 1 then all the eigenvalues of the homogeneous periodic orbit are contracting. The formal result for periodic homogeneous states reads

Theorem 1.4.1 *An homogeneous periodic orbit $\{X_t\}_{t=1,\dots,p}$ with $X_i = \{x_i\}$ of a one-way or diffusive CML is linearly stable provided that the periodic orbit $\{x_i\}_{i=1,p}$ of the local map f is linearly stable.*

Though the stability for homogeneous and periodic states has already been extensively studied [10, 11, 32, 33, 34] we thought of giving a straightforward proof leading to a very simple geometrical representation of the eigenvalues. For our purpose the only relevant case is the homogeneous state, however, more complex structures like spatio-temporally periodic states could appear so we refer the reader interested in their stability to the above papers.

Chapter 2

Localized states and propagating fronts

In this chapter we introduce some notation and definitions of localized states in CMLs and establish some of their basic properties as a framework for the propagation of fronts.

2.1 Localized states

Let $\Delta x_t(i) = |x_t(i+1) - x_t(i)|$. The *mass* $M(X_t)$ of a state X_t is defined as the total variation of the local states

$$M_t = M(X_t) = \sum_{i=-\infty}^{\infty} \Delta x_t(i). \tag{2.1}$$

Since $M_t \geq \max\{x_i\} - \min\{x_i\}$ we restrict our attention to states with positive finite mass; a zero-mass state is a uniform state (x_i = constant) and an infinite mass state is spread over an infinite region (therefore not localized) or has at least one $x_i = \pm\infty$. Thus we consider states where the sum (2.1) is finite.

For each lattice site $i \in \mathbb{Z}$ we define the probability

$$p_t(i) \;=\; \frac{\Delta x_t(i)}{M_t}, \tag{2.2}$$

which is normalized and gives the relative amount of 'mass' concentrated along the lattice. In order to describe a mass distribution we use the *mean* μ and the *variance* σ of the variable i with respect to the probability distribution (2.2):

$$\mu_t = \mu(X_t) = \sum_{i=-\infty}^{\infty} i\, p_t(i)$$
$$\sigma_t^2 = \sigma(X_t)^2 = \sum_{i=-\infty}^{\infty} (i-\mu_t)^2\, p_t(i).$$

The quantity μ_t corresponds to the *centre of mass* of the state X_t, and σ_t to its *width*. The centre of mass and the width give, respectively, the average position and spread of the distribution.

A state X_t with finite centre of mass and width is said to be *localized*. If, in addition, there exists a positive constant $\kappa < 1$ such that $\Delta x_t(i) = O(\kappa^{|i|})$, then the state is *exponentially localized*. For an exponentially localized state, not only the mean and variance exist, but also all central moments of the distribution (2.2). The above definitions of centre of mass and width are a natural description for the evolution of travelling wave fronts. Nevertheless it will be more useful for our purpose, as we shall see in chapters 4 and 5, to think of the number of interfacial sites instead of its width and to take its centre of mass at the central site of the interface. Nonetheless, for the numerical experiments —computation of the travelling velocity for example— we will continue to use the definition of centre of mass in order to locate the interface position.

We are interested in localized states that can model wave fronts. So we define a *step state* to be a localized state for which the configuration $\{x_t(i)\}$ is asymptotic, for $i \to \pm\infty$, to two distinct fixed points of f [35]:

$$\lim_{i\to\pm\infty} x_t(i) = x^*_\pm; \qquad f(x^*_\pm) = x^*_\pm. \tag{2.3}$$

The mass of a step state is then bounded from below

$$M(X_t) \geq \Delta x^* = |x^*_+ - x^*_-|. \tag{2.4}$$

The simplest such state is a *pure step state*, that is, a step function between the two fixed points

$$P(k) \equiv x_t(i) = \begin{cases} x^*_- & \text{if} \quad i \leq k \\ x^*_+ & \text{if} \quad i > k. \end{cases} \tag{2.5}$$

For this pure state $\mu(P(k)) = k$ and $\sigma(P(k)) = 0$. It is plain that a pure state is a fixed point of the CML when $\varepsilon = 0$ since all local states $\{x_i\}$ are fixed points of the local map. Moreover, an initial condition that is any combination of fixed points of the local map is a fixed point of the CML when $\varepsilon = 0$.

A step state has *minimal mass* or *minimal variation*, *i.e.* $M(x_t) = \Delta x^*$ (cf. (2.4)), if and only if its local states are ordered, that is if $x_t(i) \leq x_t(i{+}1)$ when $x^*_- < x^*_+$ (or $x_t(i) \geq x_t(i{+}1)$ when $x^*_- > x^*_+$) for all i.

Proposition 2.1.1 *If the local map f of a CML (one-way or diffusive) is a non-decreasing function (if $x^*_- < x^*_+$) or non-increasing (if $x^*_- > x^*_+$) then if X_t is a minimal mass state then so is X_{t+1}.*

Proof. We prove it by induction for a diffusive CML with a non-decreasing f and an increasing minimal mass state. For non-increasing f and one-way CML the proofs are very similar. Take a minimal mass state $X_0 = \{x_0(i)\}$:

$$\cdots \leq x_0(-1) \leq x_0(0) \leq x_0(1) \leq \cdots.$$

Suppose that the configuration of the CML at time t is that of a minimal mass state:

$$x_t(j) \leq x_t(j+1) \quad \forall\, j \in \mathbb{Z} \tag{2.6}$$

then

$$\frac{\varepsilon}{2} f(x_t(j)) \leq \frac{\varepsilon}{2} f(x_t(j+1)) \tag{2.7}$$

and

$$(1-\varepsilon)f(x_t(j)) \leq (1-\varepsilon)f(x_t(j+1)), \tag{2.8}$$

since f is non-decreasing and $0 \leq \varepsilon \leq 1$. Adding (2.8) with $j = i$ and (2.7) with $j = i-1$ and $j = i+1$ leads to

$$\begin{aligned} & (1-\varepsilon)f(x_t(i)) + \tfrac{\varepsilon}{2}\left(f(x_t(i-1)) + f(x_t(i+1))\right) \\ \leq\ & (1-\varepsilon)f(x_t(i+1)) + \tfrac{\varepsilon}{2}\left(f(x_t(i)) + f(x_t(i+2))\right), \end{aligned}$$

thus

$$x_{t+1}(i) \leq x_{t+1}(i+1).$$

Therefore the minimal mass condition is preserved under iteration if f is a non-decreasing function. For the case of a non-increasing f the inverted inequalities hold. □

The global dynamics causes the centre of mass and the width of a localized state to evolve. In this respect, two points need consideration. Firstly, the existence of the probability p_t does not automatically imply that of p_{t+1}, and secondly, the image of a localized state is not necessarily localized. To achieve the above conditions, we impose some mild restrictions on the local map f as well on the state X_t. The importance of the states defined above is that their properties (minimal mass and localization) are invariant under the dynamics of the CML under those restrictions.

Lemma 2.1.2 *Let X_t be a localized state of a one-way CML, let $x^*_\pm = \lim_{i\to\pm\infty} x_t(i)$, and let $M(X_{t+1}) \neq 0$. Then, if f is bounded and continuous at $x^*_\pm$, X_{t+1} is a localized state. If, in addition, X_t is exponentially localized, so is X_{t+1}.*

Proof. We begin considering the case $i \to \infty$. Because X_t is localized, x^*_+ is finite. Moreover, since f is continuous at x^*_+, then there exists a constant $\rho > 0$ and an integer N such that, for all $i \geq N$ we have $|f(x_t(i+1)) - f(x_t(i))| < \rho|x_t(i+1) - x_t(i)|$, whence

$$\begin{aligned} \Delta x_{t+1}(i) &= |(1-\varepsilon)\, f(x_t(i+1)) + \varepsilon\, f(x_t(i)) - (1-\varepsilon)\, f(x_t(i)) - \varepsilon\, f(x_t(i-1))| \\ &\leq (1-\varepsilon)\,|f(x_t(i+1)) - f(x_t(i))| \,+\, \varepsilon\,|f(x_t(i)) - f(x_t(i-1))| \\ &< \rho\,(1-\varepsilon)\,|x_t(i+1) - x_t(i)| \,+\, \rho\varepsilon\,|x_t(i) - x_t(i-1)| \\ &= \rho\,(1-\varepsilon)\,\Delta x_t(i) \,+\, \rho\varepsilon \Delta x_t(i-1), \qquad i > N. \end{aligned} \tag{2.9}$$

Then, from absolute convergence

$$\sum_{i=N+1}^{\infty} \Delta x_{t+1}(i) \,<\, \rho(1-\varepsilon) \sum_{i=N+1}^{\infty} \Delta x_t(i) \,+\, \rho\varepsilon \sum_{i=N+1}^{\infty} \Delta x_t(i-1) < \infty.$$

A similar inequality holds for $i \to -\infty$. From the above and the fact that any finite sum of $\Delta x_{t+1}(i)$ is bounded (because f is bounded) it follows that M_{t+1} is finite (and non-zero, by hypothesis), so that the probability p_{t+1} exists. Finally, multiplying both sides of the inequality (2.9) by i and by i^2, respectively, and summing over $i > N$ shows that μ_{t+1} and σ_{t+1} are finite, whence X_{t+1} is localized.

If X_t is exponentially localized, then there exist positive constants c and $\kappa < 1$ for which

$$\Delta x_t(i) < c\kappa^i. \tag{2.10}$$

Combining the above with (2.9) we obtain

$$\Delta x_{t+1}(i) \;<\; \kappa^i c\rho\left((1-\varepsilon)+\frac{\varepsilon}{\kappa}\right), \qquad i > N. \tag{2.11}$$

A similar estimate holds for negative i, showing that X_{t+1} is exponentially localized (possibly with a larger constant c). □

From Lemma 2.1.2 and the fact that the mass of a step state is bounded (cf. (2.4)) we obtain immediately

Corollary 2.1.3 *Let X_t be a step state of a one-way CML, and let f be bounded and continuous at $x^*_\pm$. Then X_{t+1} is a step state. If, in addition, X_t is exponentially localized, so is X_{t+1}.*

This last property comes from the *bistability* of the CML, that is the local map f to have two fixed points $x^*_\pm$ that support the step state. We are dealing with CML models with nearest-neighbour coupling, so it is impossible for any kind of signal, originated from the coupling, to travel faster than one site per time step (unit velocity). On the other hand, the bistability allows a state of the form

$$X_t = (\ldots, x^*_-, x^*_-, x_t(k), \ldots, x_t(k+l), x^*_+, x^*_+, \ldots), \tag{2.12}$$

with k and l fixed, to evolve after s iterations to

$$X_{t+s} = (\ldots, x^*_-, x^*_-, x_{t+s}(k), \ldots, x_{t+s}(k+l+s), x^*_+, x^*_+, \ldots)$$

for a one-way CML and to

$$X_{t+s} = (\ldots, x^*_-, x^*_-, x_{t+s}(k-s), \ldots, x_{t+s}(k+l+s), x^*_+, x^*_+, \ldots)$$

for a diffusive CML. Thus, a step state of the form (2.12) will remain of the same form, with generally more sites in the intermediate regime between x^*_- and x^*_+, if $x^*_\pm$ are fixed points of f. For the special case of $\varepsilon = 0$ the state (2.12) evolves like

$$X_{t+s} = (\ldots, x^*_-, x^*_-, f^s(x_t(k)), \ldots, f^s(x_t(k+l)), x^*_+, x^*_+, \ldots),$$

and will remain localized in the same region (between $i = k$ and $i = k+l$) at any time. Thus in the uncoupled case there is no propagation of any kind through the lattice.

It is important to notice that Lemma 2.1.2 and Corollary 2.1.3 do not prove the exponential localization when $t \to \infty$. In fact, there are cases where the state becomes infinitely spread along the lattice as $t \to \infty$ and so they loose localization.

2.2 Travelling velocity and basic properties

From the previous definitions and results it is clear that if the initial state X_0 is a step state, then $\mu(X_t)$ and $\sigma(X_t)$ are defined for all $t \geq 0$. Our main interest is to determine the average velocity v of the centre of mass, namely

$$v \;=\; v(\varepsilon, X_0) \;=\; \lim_{t\to\infty} \frac{1}{t}(\mu_t - \mu_0).$$

The velocity of the travelling front as a function of the coupling parameter ε obeys quite general properties, such as monotonicity (theorem 2.2.1), symmetry with respect to the point (1/2,1/2) (theorem 2.2.2) and continuation of the non-propagating case $v(\varepsilon = 0) = 0$ for small ε (theorem 2.2.3). The precise statements of these properties are given in the theorems. We consider the evolution of step states between x^*_- and x^*_+ ($x^*_- < x^*_+$ and $f(x^*_\pm) = x^*_\pm$) for non-decreasing local maps. The same results apply for a non-increasing f and $x^*_- > x^*_+$. For the following results we suppose that a travelling front with velocity $v(\varepsilon)$ exists.

Theorem 2.2.1 *The velocity $v(\varepsilon)$ of a step state with minimal mass is a non-decreasing function of ε in a one-way CML provided that the local map f is non-decreasing.*

Proof: We proceed by induction. We start with a minimal mass state $X_0 = (\ldots, x_0(-1), x_0(0), x_0(1), \ldots)$ with

$$\cdots \leq x_0(-1) \leq x_0(0) \leq x_0(1) \leq \cdots.$$

Let us consider two parameter values ε and ε' such that

$$\Delta\varepsilon = \varepsilon' - \varepsilon > 0. \tag{2.13}$$

We now follow the evolution of the configurations X_t and X'_t with corresponding coupling parameters ε and ε' and starting with the same initial condition $X_0 = X'_0$. We know that the minimal mass property of X_t and X'_t is preserved under iteration if f is non-decreasing (cf. proposition 2.1.1). Thus

$$x_t(i) \geq x_t(i-1) \tag{2.14}$$

and

$$x'_t(i) \geq x'_t(i-1). \tag{2.15}$$

The dynamics of two configurations is given respectively by

$$x_{t+1}(i) = (1-\varepsilon)f(x_t(i)) + \varepsilon f(x_t(i-1)) \tag{2.16}$$

and

$$x'_{t+1}(i) = (1-\varepsilon')f(x'_t(i)) + \varepsilon' f(x'_t(i-1)). \tag{2.17}$$

By subtracting eq. (2.17) from eq. (2.16) after one iteration we obtain

$$\begin{aligned} x_1(i) - x'_1(i) \;=\; & [(1-\varepsilon)f(x_0(i)) + \varepsilon f(x_0(i-1))] - [(1-\varepsilon)f(x'_0(i)) \\ & + \varepsilon f(x'_0(i-1))] + \Delta\varepsilon\left(f(x'_0(i)) - f(x'_0(i-1))\right). \end{aligned} \tag{2.18}$$

Because the initial condition is the same for both configurations the first two terms cancel each other, and eq. (2.18) reduces to

$$x_1(i) - x'_1(i) = \Delta\varepsilon\left(f(x'_0(i) - f(x'_0(i-1))\right).$$

Thus, if f is a non-decreasing function and recalling eq. (2.13) and (2.15) we have

$$x_1(i) \geq x'_1(i) \quad \forall i. \tag{2.19}$$

Equation (2.19) says that, after the first iteration, any i-th site of X'_1 is below, or equal to, the i-th site of X_1. This may be denoted as $X_1 \geq X'_1$ and may be referred by saying that the configuration X'_1 is below, or equal to, the one of X_1. Since we are dealing with step states

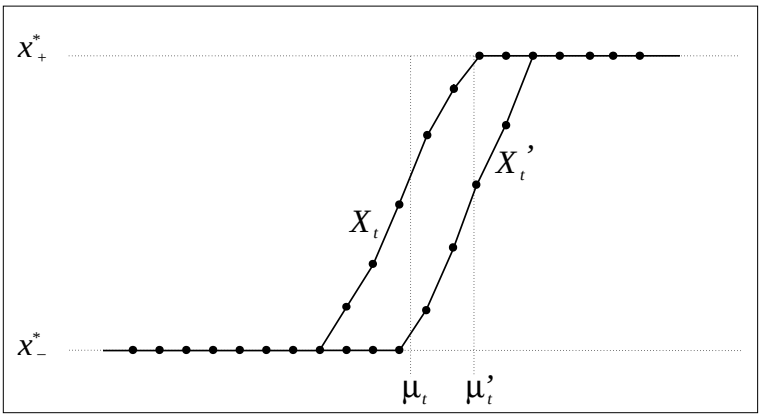

Figure 2.1: Configuration of two, initially identical, minimal mass step states with different coupling parameters. The step states X_t and X'_t correspond, respectively, to coupling parameters ε and ε' with $\varepsilon' > \varepsilon$. The centre of mass μ'_t of the state with largest ε advances further (the propagation is from left to right).

with minimal mass between x^*_- and x^*_+, saying that the configuration X'_1 is below or equal to the one of X_1 is the same that saying that the centre of mass μ_1 of X_1 is smaller or equal to the centre of mass μ'_1 of X'_1. Hence the configuration X'_1 has advanced more than the one of X_1 —with configurations not necessarily of the same shape— see figure 2.1. Therefore, for the first iteration, increasing ε results in a further advance (to the right) of the step state.

We now extend the above result for any successive iteration. Suppose that at time t

$$x_t(i) \geq x'_t(i). \tag{2.20}$$

Applying the corresponding dynamics (2.16) and (2.17) and subtracting the two resulting configurations gives

$$\begin{aligned} x_{t+1}(i) - x'_{t+1}(i) &= [(1-\varepsilon)f(x_t(i)) + \varepsilon f(x_t(i-1))] - [(1-\varepsilon)f(x'_t(i)) \\ &\quad + \varepsilon f(x'_t(i-1))] + \Delta\varepsilon\left(f(x'_t(i) - f(x'_t(i-1))\right). \end{aligned} \tag{2.21}$$

It is plain that the last term in eq. (2.21) is non-negative since f is non-decreasing and X'_t has always minimal mass. But this time, the first two terms does not cancel each other. Applying f to both sides of (2.20) for i and $i-1$, and multiplying by $1-\varepsilon$ and ε respectively, leads to

$$\begin{aligned} (1-\varepsilon)f(x_t(i)) &\geq (1-\varepsilon)f(x'_t(i)) \\ \varepsilon f(x_t(i-1)) &\geq \varepsilon f(x'_t(i-1)), \end{aligned}$$

whence to

$$(1-\varepsilon)f(x_t(i)) + \varepsilon f(x_t(i-1)) \geq (1-\varepsilon)f(x'_t(i)) + \varepsilon f(x'_t(i-1)).$$

Therefore, the first two terms of (2.21) combine to a positive quantity and hence

$$x_t(i) \geq x'_t(i) \quad \Rightarrow \quad x_{t+1}(i) \geq x'_{t+1}(i). \tag{2.22}$$

Because (2.22) is true for $t = 0$ (cf. (2.19)) then, by induction, (2.22) is true for any t. The two initially identical configurations X_0 and X'_0 evolve with a corresponding coupling

parameter $\varepsilon < \varepsilon'$. From the above result one has that $x_t(i) \geq x'_t(i)$ for all t, and because $X(t)$ and $X'(t)$ are minimal mass step states between x^*_- and x^*_+ we have

$$\mu_t \leq \mu'_t \quad \forall t.$$

Thus if the limits

$$v(\varepsilon) = \lim_{t\to\infty} \frac{\mu_t - \mu_0}{t} \quad \text{and} \quad v'(\varepsilon) = \lim_{t\to\infty} \frac{\mu'_t - \mu'_0}{t}$$

exist, we conclude that

$$\varepsilon' > \varepsilon \quad \Rightarrow \quad v(\varepsilon') \geq v(\varepsilon).$$

Therefore $v(\varepsilon)$ is non-decreasing provided that f is non-decreasing. □

It is worth to mention that the one-way CML model we are using (cf. (0.6)) is coupling a site to its left neighbour, and hence the propagation of any kind of information through the lattice ought to be from left to right. For a diffusive CML the sites are coupled both to the right and to the left neighbours and hence, in this case, a signal could propagate in any direction. As we will see later in section 3.3 the direction of propagation is determined by the local map.

Another general feature of the velocity of the travelling front in a one-way CML is its symmetry around its centre point:

Theorem 2.2.2 *The velocity of the travelling front in a one-way CML of the form* (0.6) *is symmetric with respect to the point* $(\varepsilon, v(\varepsilon)) = (1/2, 1/2)$*, that is* $v(\varepsilon) = 1 - v(1-\varepsilon)$*.*

Proof. Let $\delta = 1 - \varepsilon$ and consider a moving reference frame with a unit positive velocity:

$$\begin{cases} y_t(i) &= x_t(i) \\ y_{t+1}(i) &= x_{t+1}(i+1) \\ \vdots & \vdots \\ y_{t+k}(i) &= x_{t+k}(i+k). \end{cases}$$

The one-way CML in the moving frame now reads

$$\begin{aligned} y_{t+1}(i-1) &= \delta f(y_t(i)) + (1-\delta) f(y_t(i-1)) \\ \Longrightarrow \quad y_{t+1}(i) &= (1-\delta) f(y_t(i)) + \delta f(y_t(i+1)). \end{aligned} \tag{2.23}$$

Equation (2.23) represents a one-way CML of the type (0.6) but coupled in the opposite direction. Thus, taking into account the moving reference frame and the definition of δ we can conclude that

$$1 - v(\varepsilon) = v(1-\varepsilon). \tag{2.24}$$

This important symmetric property allows one to restrict the study of the velocity to the ε-interval $[0, 1/2]$ when dealing with a one-way CML. □

As we mentioned earlier, when $\varepsilon = 0$ there is no propagation through the lattice. We expect the step state to evolve as we increase the value of the coupling parameter and do so continuously from the uncoupled limit [36]. The limit when $\varepsilon \to \infty$ corresponds to the continuum limit so the $\varepsilon \to 0$ is called the *anti-continuum limit* —first introduced by Aubry as the anti-integrable limit [37]. A formal analysis on the stability of exponentially localized step states establishes the following quite general property of the velocity of a step state in one-way CML:

Theorem 2.2.3 *Let X_0 be an exponentially localized step state of a one-way CML. Let the local map f be bounded, and let f be a contraction mapping in a neighbourhood of the fixed points* (2.3)*. Then, for all sufficiently small ε, $v(\varepsilon) = 0$ and $v(1-\varepsilon) = 1$, independently of X_0.*

Proof. We deal with the case of small coupling first, and positive i. From Corollary 2.1.3 we know that X_t is an exponentially localized step state for all $t \geq 0$. By assumption f is a contraction mapping in some domain $|x - x_+^*| < r$. Let N' be such that for all $i \geq N'$ we have $|x_t(i) - x_+^*| < r/2$, so that $\Delta x_t(i) < r$. Then, for $i \geq N'$, the constant ρ appearing in (2.9) can be chosen to be smaller than 1.

Let N'' be such that $\Delta x_t(i) < 1$ for all $i \geq N''$, and let $N = \max(N', N'')$. Then since X_t is exponentially localized, we can choose κ so that the bound (2.10) holds for $i \geq N$ with $c = 1$. Letting $c = 1$ in (2.11) it follows that

$$\Delta x_{t+1}(i) \;<\; \kappa^i \qquad\qquad i > N \tag{2.25}$$

provided that

$$\varepsilon < \frac{\kappa}{\rho}\,\frac{1-\rho}{1-\kappa}$$

which is satisfied for sufficiently small ε, since the right hand side is positive.

It remains to consider the case $i = N$. Because f is bounded, the quantity

$$\Delta f = \sup_x f(x) - \inf_x f(x)$$

is finite. We have, in place of (2.9)

$$\Delta x_{t+1}(N) < \rho\,(1-\varepsilon)\,\Delta x_t(N) + \varepsilon\,\Delta f$$

giving, for all $t \geq 0$

$$\Delta x_{t+1}(N) < \alpha^{t+1}\kappa^N + \varepsilon\,\Delta f\,\frac{1-\alpha^{t+1}}{1-\alpha},$$

where $\alpha = \rho(1-\varepsilon) < 1$. The right-hand side of the above inequality can be made smaller than κ^N for all t, provided that ε is sufficiently small. Thus the inequality (2.25) holds also for $i = N$.

Let i be negative. Assuming that $\Delta x_t(i) < \kappa^{-i}$ for all sufficiently large (negative) i, and proceeding as above, we find that the bound $\Delta x_t(i) < \kappa^{-i}$ for $i \leq -N$ implies that

$$\Delta x_{t+1}(N) < \kappa^{-i}\rho\,(1-\varepsilon+\varepsilon\kappa) < \kappa^{-i}; \qquad\qquad i < -N$$

for all ε (all constants have been redefined). The case $i = -N$ gives the recursive inequality

$$\Delta x_{t+1}(-N) < (1-\varepsilon)\,\Delta f + \rho\varepsilon\kappa^{N+1}$$

which, as before, yields $\Delta x_{t+1}(-N) < \kappa^N$ for sufficiently small ε.

The above induction establishes the time-independent bound

$$\Delta x_t(i) < \kappa^{|i|}, \qquad\qquad |i| \geq N, \qquad t \geq 0,$$

for a suitable choice of κ and N, and for all sufficiently small ε. In this ε-range, from the boundedness of f we conclude that $|\mu_t|$ and σ_t are bounded from above for all times. Thus

$v(\varepsilon) = 0$, and X_t remains a step state also in the limit $t \to \infty$. Using the symmetric property (2.24), it follows that the same result holds for $v(1-\varepsilon)$. □

The above theorem is a general property of travelling front in a one-way CML. Using the same ideas as in [36, 38] for a network of units, one could find an estimate for the value of ε up to where the non-propagating case persists. The condition that f be a contraction mapping is a bit stronger than the condition that $x^*_\pm$ be attracting. We shall see (chapter 4) that for an initial localized pure step state of the type (2.5), the critical behaviour is much richer than a discontinuous transition from $v = 0$ to $v = 1$, at some intermediate value of ε. Rather, the dependence of v on ε is characterized by infinitely many critical values, in correspondence to the boundaries of intervals in ε, where the velocity is a given rational number.

Chapter 3

Travelling wave fronts

In this chapter we deal with the coherent propagation of a wave front, without damping or dispersion, along the lattice. We confine our attention to states with minimal mass. In order to ensure that this property is preserved under iteration, we shall require the local map f to be non-decreasing as stated before.

3.1 A bistable local map f

As it should be clear from the previous chapter, two fixed points of the local map f are necessary in order for the CML to support a step state (also called *kink* or *wave front*) for zero coupling. As mentioned before (cf. Theorem 2.2.3) the steady step state persists for small values of ε. We would like now to be able to increase further ε for the step state to travel along the lattice. We now describe a simple mechanism that allows step states to travel.

Consider a continuous non-decreasing local map f with two fixed attracting points x^*_- and x^*_+ (with $x^*_- < x^*_+$), *i.e.* $|f(x^*_\pm)| < 1$. The case of a non-increasing f and $x^*_- > x^*_+$ is equivalent. We focus our attention on the restricted map

$$f:\ [x^*_-, x^*_+] \to [x^*_-, x^*_+].$$

It is plain that if the initial state of the lattice verifies the condition $x^*_- \le x_0(i) \le x^*_+$, then for any $t > 0$ all the dynamics takes place in the interval $[x^*_-, x^*_+]$, *i.e.* $x^*_- \le x_t(i) \le x^*_+$, provided that $0 \le \varepsilon \le 1$. The fixed points $x^*_\pm$ are attractive but not necessarily superattractive (a note on this respect is given in the next section). A typical plot of such smooth local maps is shown in figure 3.1. By the continuity of f, there exists an unstable fixed point x^*_0 with $x^*_- < x^*_0 < x^*_+$. We denote the basins of attraction of x^*_- and x^*_+ to be $I_- = [x^*_-, x^*_0)$ and $I_+ = (x^*_0, x^*_+]$ respectively.

Let us consider the initial state X_0 to be a step state with minimal mass such that $\lim_{i\to\pm\infty} x_t(i) = x^*_\pm$. The dynamics at $\varepsilon = 0$ is trivial since any site in I_- (I_+) tends to x^*_- (x^*_+); thus after a transient —recall that X_0 has minimal mass so all the sites to the left (right) of x^*_0 tend to x^*_- (x^*_+)— the final state will be a pure step state (see figure 3.2.a). The marginal case when one or more sites have the initial position at the unstable point

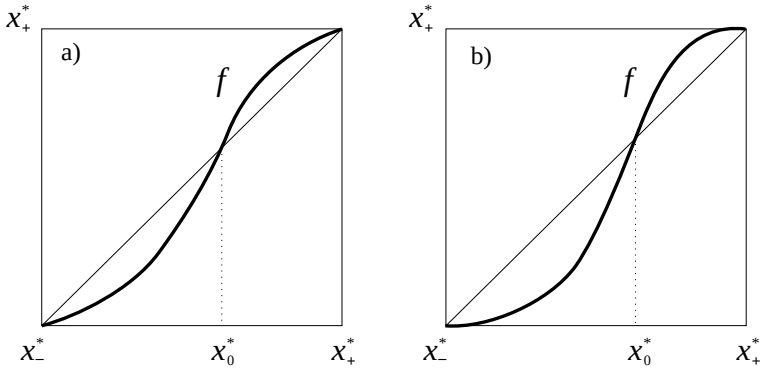

Figure 3.1: A bistable continuous map f. The local map f has two (a) stable ((b) superstable) fixed points $x^*_\pm$, because of continuity there exists an unstable fixed point x^*_0 between them.

x^*_0 is unstable. As we switch on the coupling parameter, these sites are pushed out of the unstable equilibrium to one of the basins of attraction $I_\pm$ (no matter how small ε is), so that the lattice tends to a pure step state as well (see figure 3.2.b). Therefore, from now on we will consider the initial configuration to be a pure step state.

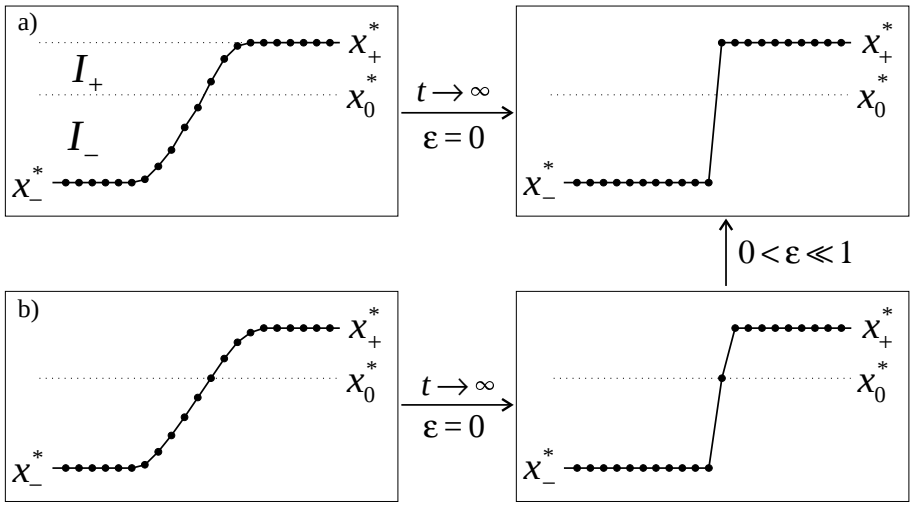

Figure 3.2: Evolution of an initial minimal mass step state for zero coupling. (a) All the sites that where initially in I_- (I_+) tend to x^*_- (x^*_+) and the final state is then a pure step state. (b) A site initially set at the unstable fixed point x^*_0 remains at its position at all times for zero coupling, but if the coupling is slightly increased ($0 < \varepsilon \ll 1$) the configuration tends to a pure step state.

As we increase the coupling parameter, the interaction between neighbours may 'pull out' some sites of their initial basin of attraction to the other basin of attraction, possibly causing the step state to evolve. We consider first the case of a one-way CML and then the diffusive one.

3.2 Travelling wave fronts in one-way CMLs

An initial pure step state is stable for $\varepsilon = 0$ since the individual sites are located at the stable fixed points of f. We know (Theorem 2.2.3) that if ε is small enough the resulting exponentially localized step state does not travel. What is happening internally in the lattice is that the coupling causes the first (left-most) sites of I_+ (grey site in figure 3.3.a) to be 'pulled down' towards I_- by the last (right-most) sites of the basin I_- (white site in figure 3.3.a) but at the same time the internal dynamics 'pulls up' the sites in I_+ towards the stable fixed point x_+^*. Overall, for ε small enough, the 'pulling down' by the coupling is balanced by the 'pulling up' of the stable internal dynamics, and then the step state cannot evolve (figure 3.3.a). This balance is broken when we increase further the coupling (figure 3.3.b).

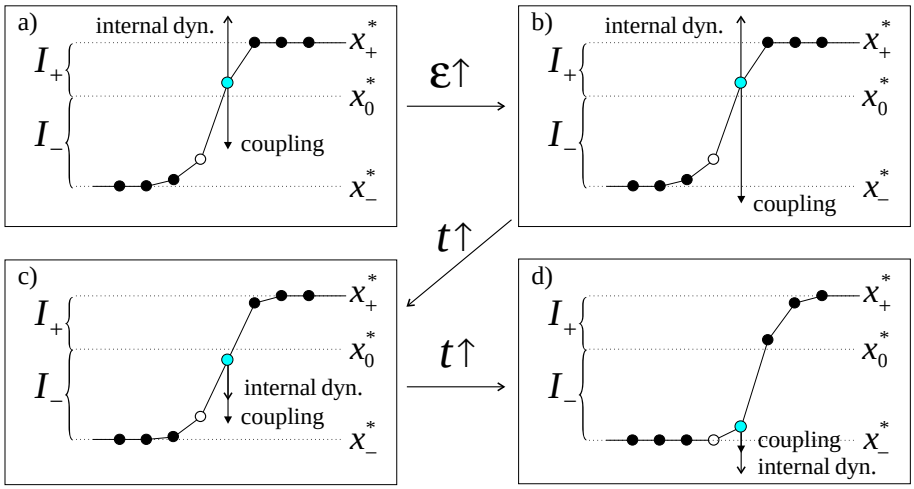

Figure 3.3: Competing dynamics in the interface of a step state in a one-way CML. (a) the coupling exerted by the white site pulls the grey site downwards but the attraction by the internal dynamics towards the stable point x_+^* pulls upwards with the same strength. (b) If we increase ε the coupling supersedes the upwards pulling and the grey site is pulled into I_- (c) where both, the coupling and the attraction towards x_-^*, pull in the same direction (d).

If the coupling is strong enough to break the balance, the first sites of I_+ are 'pulled down' sufficiently and fall into the basin of attraction I_- (figure 3.3.c). Once a site is in I_- it will, not only be 'pulled down' by the previous neighbours, but it will be attracted towards x_-^* as well, making the dynamics of those sites to converge rapidly to x_-^* (figure 3.3.d). Loosely speaking, every time a site is 'pulled down' from I_+ to I_- the step state moves to the right. Once the first site of I_+ has been pulled into I_-, its right neighbour will in turn follow the same destiny. This procedure may be pictorially portrayed as a battle between the I_- and the I_+ kingdoms where both armies are fighting for territory and once a prisoner is taken it switches party and then its new kingdom has one more head to help in the combat. This battle is very unfair since the overall capture of enemies is biased: the I_- army is the only one that can 'pull' enemies towards its territory and convert them into new recruits (the coupling is in one direction only). Maybe later, the army I_+ will have more chances in a diffusive CML case...

The result of the bias in the competing dynamics at the interface is to induce a gradual advance of the step state. An example of this phenomenon may be observed in figure 3.4.a where we plotted the evolution of a step state in a one-way CML with a cubic local map.

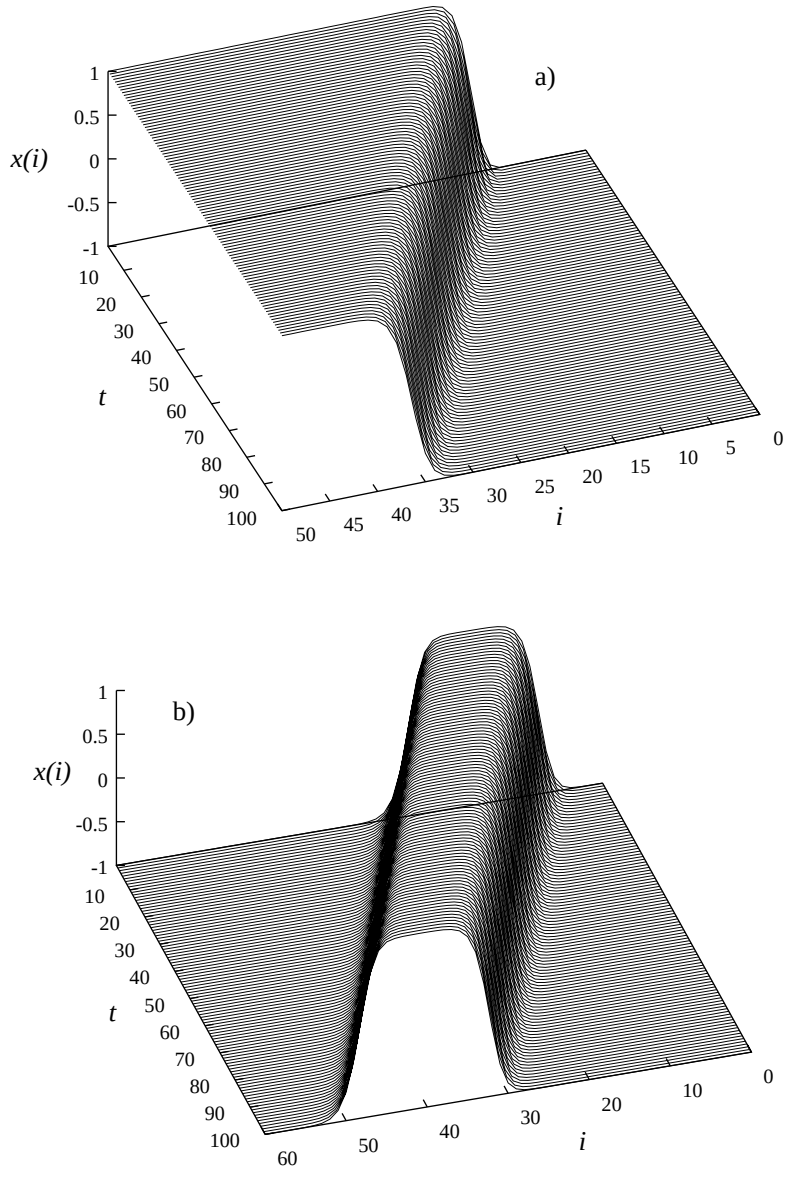

Figure 3.4: (a) Travelling step state in a one-way CML with the cubic local map defined in 3.6 for $\varepsilon = 0.25$ and $\alpha = 0.4$. The travelling velocity is $v(\varepsilon) = 1/4$. (b) For the same value of the parameters it is possible to send a whole kink in the same travelling direction.

The value of the coupling parameter, $\varepsilon = 0.25$, in figure 3.4 is large enough to break the balance between the competing dynamics and to create a bias for the sites to pass from I_+ to I_-. Since the local map is symmetric, whatever happens to a left step state will happen to a right step state, that is, we could send a whole kink (a combination of a left plus a right step state separated by an homogeneous region) through the lattice. Both ends of the kink travel with the same velocity and then its shape remains unchanged (see figure 3.4.b) thanks to the symmetry of the local map.

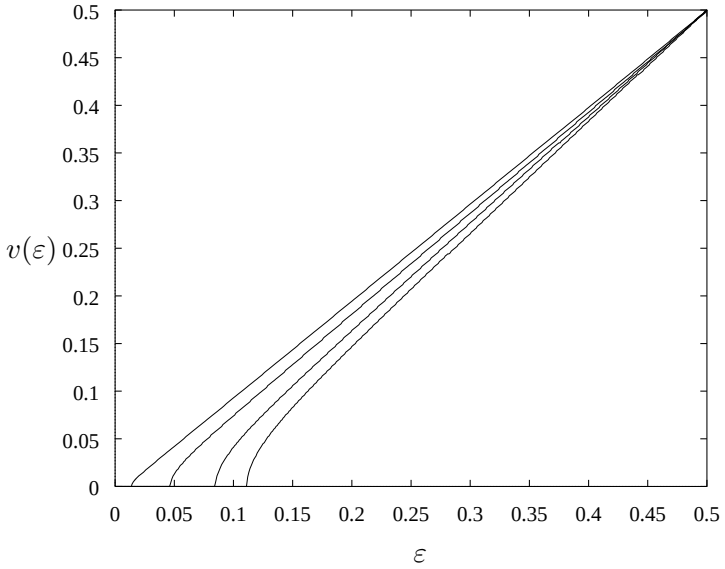

Figure 3.5: Velocity $v(\varepsilon)$ of the travelling step state as a function of the coupling parameter ε for the family of smooth local maps depicted in figure 3.6. Each curve, from left to right, corresponds to the local maps in figure 3.6 but from right to left. As the derivative at the unstable fixed point $x_0^* = 0$ increases in figure 3.6 the velocity decreases because the unstable point repels sites trying to switch from the basin of attraction I_+ to I_-.

The effect of the superattractiveness of the points $x_\pm^*$ is to enhance the overall attraction towards it and thus the travelling step state is more stable under perturbations. On the other hand, the unstable point x_0^*, at the boundary of the two basins of attraction, repels any site that gets closer to it making more difficult for any site to pass from one basin of attraction to the other. A measure of how repulsive is x_0^* is given by $f'(x_0^*)$. Consider two close maps f_1 and f_2 whose derivatives at the unstable point satisfy $1 < f_1'(x_0^*) < f_2'(x_0^*)$. The sites of the travelling step state will find more opposition to pass from I_+ to I_- with f_2 rather than with f_1 and thus one would expect that the velocity is smaller for f_2 than for f_1. In order to illustrate this phenomenon we plotted in figure 3.5 the velocity of the travelling step state as a function of ε for the family of local maps given in figure 3.6. As we may notice, the largest velocity curve corresponds to the map with smaller derivative at the unstable point $x_0^* = 0$. It is important to note that this is not always the case as it is possible to find maps with smaller derivative at x_0^* but whose velocity is smaller for certain values of ε. This is because the derivative at x_0^* is a local property of f, while the wave front velocity is also affected by other features of the map (derivatives at $x_\pm^*$, sizes of $I_\pm$, concavity, etc.).

Another feature that changes when we vary the derivative at the unstable point, is the critical parameter ε_c corresponding to the value of ε where there is a transition from a stationary front ($v(\varepsilon) = 0$) to a moving one ($v(\varepsilon) > 0$). As we mentioned above, the

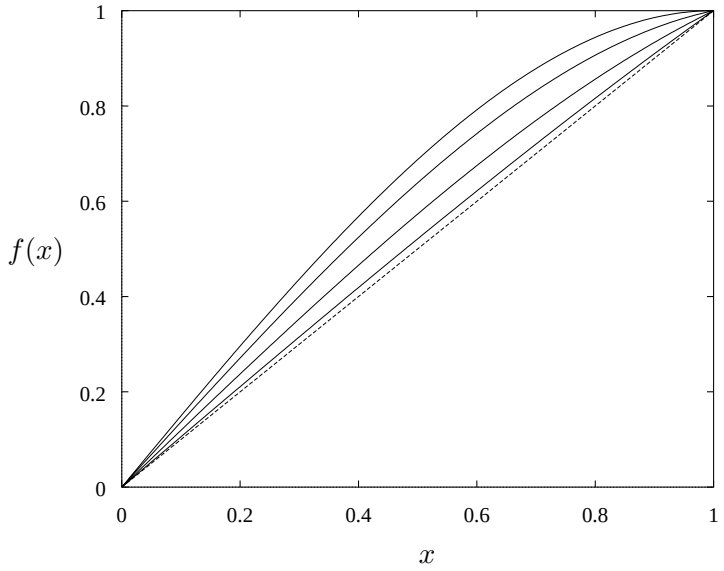

Figure 3.6: Family $f = (-\alpha^2\, x^3 + 3x)/(3 - \alpha^2)$ of bistable local maps used in figure 3.5. This cubic map has two stable fixed points $x^*_\pm = \pm 1$ and an unstable fixed point $x^*_0 = 0$ for $0 < \alpha < \sqrt{(3/2)} \simeq 1.22474$ and it is antisymmetric with respect to x^*_0. The curves, from left to right, correspond to $\alpha = 1,\ 0.9,\ 0.7,\ 0.4$ for which $f'(x^*_0) = 3/(3 - \alpha^2) = 1.5,\ 1.3698\ldots,\ 1.1952\ldots,\ 1.0563\ldots$.

transition from I_+ to I_- becomes more difficult as we increase $f'(x^*_0)$. This is reflected in figure 3.5 where the curves, from left to right, present values of ε_c that increase as $f'(x^*_0)$ increases. To have a clearer picture of this phenomenon we plotted in figure 3.7 the value of the critical point ε_c as a function of the derivative at the unstable point of the cubic map in figure 3.6. The plot clearly shows a strictly increasing function corroborating our intuition.

Finally, it is worth mentioning that the direction of propagation of the travelling wave front in a one-way CML is completely determined by the direction of the coupling itself. It is obviously impossible to send a right-to-left signal in the one-way CML defined before (eq. (0.6)); to do so we must invert the direction of the coupling by coupling the i-th site to its right neighbour $(i + 1)$, instead of the left one $(i - 1)$. To construct a CML that can support travelling fronts in both directions, by suitably changing the local map f, one must choose a coupling that involves left and right neighbours, in order to have the possibility of information travelling in both directions in the lattice. A possible candidate is the diffusive CML (0.5) as explained in the next section.

3.3 Travelling wave fronts in diffusive CMLs

The travelling wave front in one-way CMLs is the result of the bias between competing attractors created by the one-directional coupling. Let us consider now a diffusive CML of the type (0.5) with an antisymmetric local map f as the one used in the previous examples for the one-way CML case. In this diffusive CML the coupling itself is symmetric, *i.e.* there is a factor of $\varepsilon/2$ for both directions of coupling, and thus taking an antisymmetric f will result in an even contribution from both sides of the i-th site. The overall result is that the front stays in the same position, *i.e.* the centre of mass does not move, but this does not

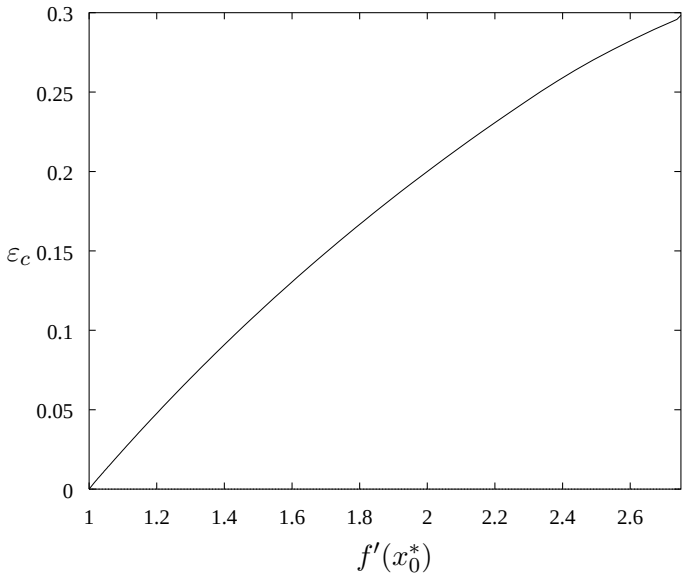

Figure 3.7: Dependence of the critical parameter value ε_c, at which the wave front begins to travel, upon the derivative at the unstable point $x_0^* = 0$, for the cubic map of figure 3.6.

mean that the front has the same shape at all times. In order to illustrate this phenomenon take the initial condition to be the pure step state $P(40)$ (cf. 2.5) and iterate the diffusive CML with the cubic local map defined in figure 3.6 for several values of α and ε. The result, after 10 000 transients, is plotted in figure 3.8.

We have then a non-propagating front. It is possible to show that there exists a stable configuration for the lattice [39, 7, 40], depending on the local map and the coupling parameter, to which any front tends. The shape of the front can be obtained by means of a continuum approximation [41, 42, 43]. For doing so one supposes that the wave front is widely spread in order to approximate the discrete space by a continuous one. The wave front in the CML is then approximated by a single ODE and it corresponds to an heteroclinic connection of two unstable points [44, 45]. This procedure is very similar to the one used in [46, 47] where the travelling fronts in LDEs (Lattice Dynamical Systems, that is a lattice of coupled ODEs) are described by a single ODE.

The fixed shape solution $h(i)$ is determined by the system of equations

$$h(i) = (1-\varepsilon) f(h(i)) + \frac{\varepsilon}{2} \left(f(h(i-1)) + f(h(i+1)) \right), \tag{3.1}$$

for i running from $-\infty$ to $+\infty$. If we assume that the space is continuous, *i.e.* $i \in \mathbb{R}$, equation 3.1 reduces to that for the motion of a particle of mass $m = \varepsilon/2$ in the potential

$$V(h) = \int \left(f(h) - h \right) dh.$$

For the cubic local map $f(x) = (-\alpha^2 x^3 + 3x)/(3-\alpha^2)$ the potential reduces to

$$\begin{aligned} V(h) &= \int \left(\frac{-\alpha^2 h^3 + 3h}{3-\alpha^2} - h \right) dh \\ &= \frac{\alpha^2 h^2}{4(3-\alpha^2)} \left(2 - h^2 \right). \end{aligned} \tag{3.2}$$

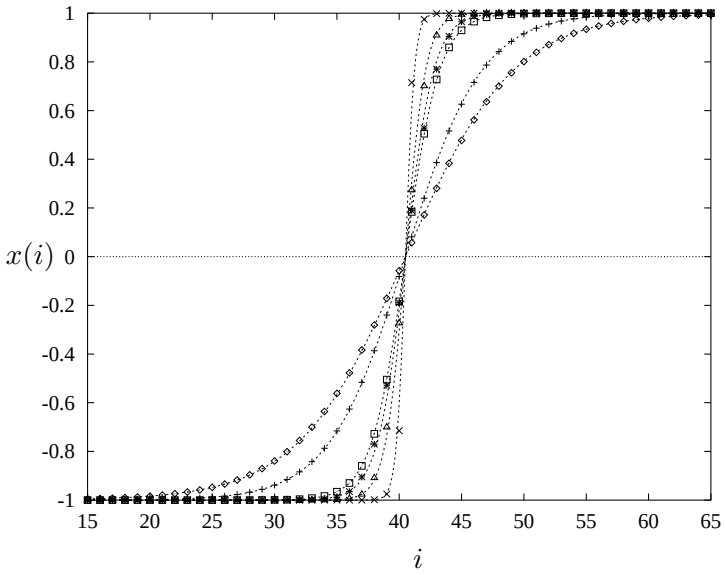

Figure 3.8: The stationary front shape, starting with a pure step state at $i = 40$, after 10 000 transients, in the diffusive CML with the cubic local map defined in figure 3.6 with the following parameter values: ($\diamond$) $\alpha = 0.2$, $\varepsilon = 0.995$; ($+$) $\alpha = 0.2$, $\varepsilon = 0.5$; ($\Box$) $\alpha = 0.2$, $\varepsilon = 0.1$; ($\times$) $\alpha = 0.7$, $\varepsilon = 0.1$; ($\triangle$) $\alpha = 0.7$, $\varepsilon = 0.5$ and ($*$) $\alpha = 0.7$, $\varepsilon = 0.995$. The dashed lines represent the continuum approximation (3.5).

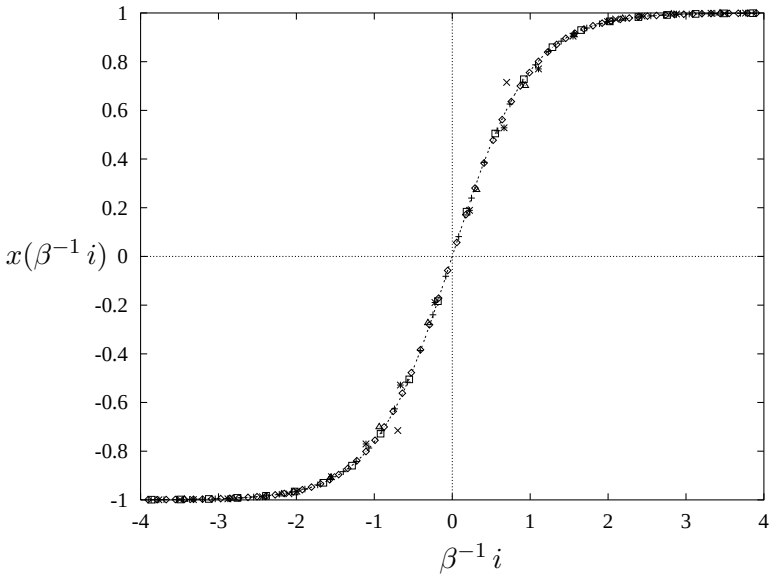

Figure 3.9: The rescaled profiles translated to the origin for the parameter values of figure 3.8. The dashed curve represents the hyperbolic tangent function.

The total energy E for this system is equal to the potential at the extremums

$$E = V(x_{\pm}^{*}) = \frac{\alpha^2}{4(3-\alpha^2)}, \tag{3.3}$$

whereas the first integral of motion, the energy, is the sum of the kinetic T and potential V energies

$$E = T + V = \frac{1}{2} m \dot{h}^2 + V(h). \tag{3.4}$$

Combining (3.2) and (3.3) in (3.4), and replacing $m = \varepsilon/2$, leads to the differential equation

$$\frac{3-\alpha^2}{\alpha^2} \varepsilon \, \dot{h}^2 - \Big(h^2 - 1\Big)^2 = 0.$$

whose solution is given by

$$h(y) = \tanh(\beta \, y) \tag{3.5}$$

where

$$\beta = \sqrt{\frac{\alpha^2}{\varepsilon(3-\alpha^2)}}.$$

A comparison between the shape of the stable stationary state and the continuum approximation is shown in figure 3.8 where the graph of (3.5) for the corresponding values of α and ε is plotted with dashed lines. The approximation is quite good. In order to have a better comparison notice that the continuum approximation only depends on the parameters α and ε, so one can rescale the front by a factor of β^{-1} on the X-axis so that the remaining profile no longer depends on α nor ε. In figure 3.9 we plotted such rescaled profile, translated to the origin, for the same curves that in figure 3.8 with the curve of the hyperbolic tangent tanh. One notices that all profiles follow the same shape. For fronts with few sites in the interface (case ($\times$) $\alpha = 0.7$, $\varepsilon = 0.1$ for example) the continuum approximation is not as good for fronts with many sites in the interface (case ($\diamond$) $\alpha = 0.2$, $\varepsilon = 0.995$ for example), this is because the approximation assumes a continuum space and thus the approximation will be better as there are more sites in the interface, *i.e.* a 'less' discrete space.

For the front to advance one needs asymmetry, either in the coupling or in the local map (with respect to the repeller point x_0^*) which generates a bias between competing attractors. This assertion can be formalized in the following sense [39]. Suppose we have a diffusive CML that has a propagating front $h(z)$ with $z = i - vt$, that is, a travelling interface with shape $h(i)$ and velocity v. Let us suppose that the front is moving with a small velocity $v \ll 1$ and assume, for the time being, that the variable i is continuous. The first order approximation of $h(z - v)$ is

$$h(z - v) = h(z) - v \left.\frac{dh}{dz}\right|_{z=i-vt},$$

which, using a continuum approximation of the diffusive CML (0.5) gives

$$h(z) - v h'(z) = f(h(z)) + \frac{\varepsilon}{2} \nabla f(h(z)). \tag{3.6}$$

Integrating eq. (3.6) over $\mathbb{R}$ and taking into account that

$$\int_{-\infty}^{+\infty} h'(z) \, dz = x_{+}^{*} - x_{-}^{*}$$

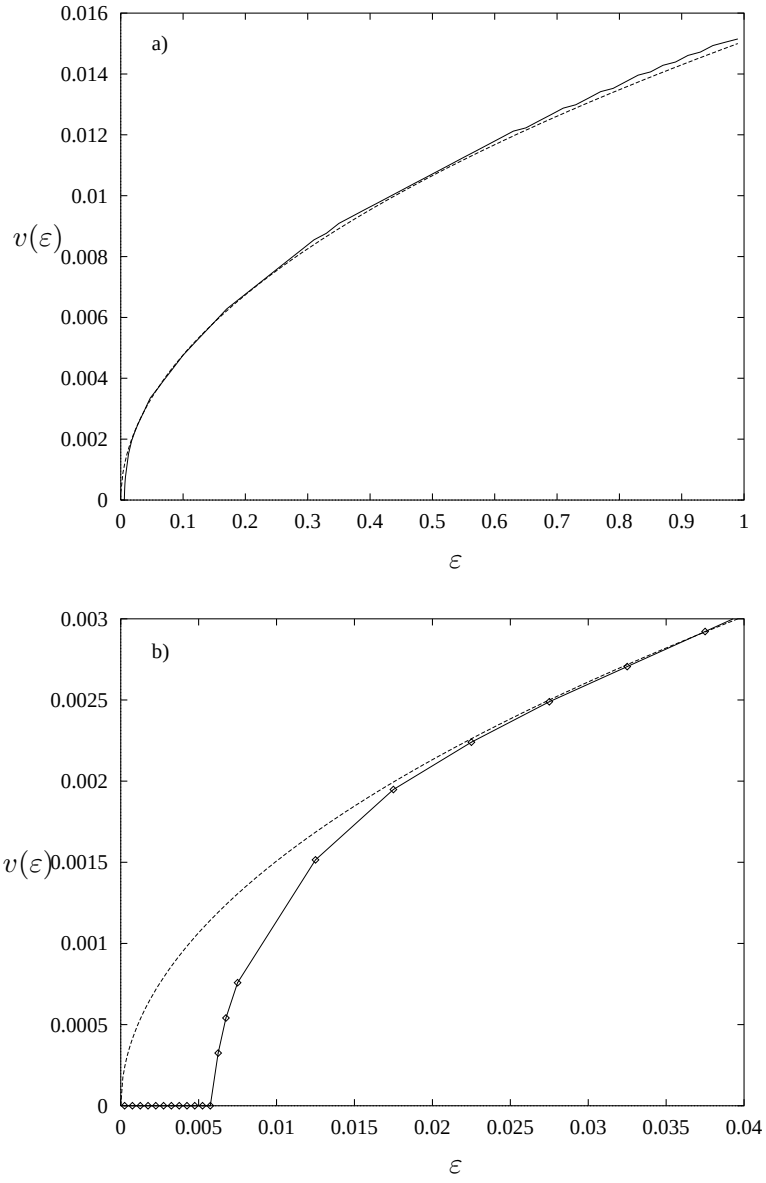

Figure 3.10: (a) Velocity of the travelling front in a diffusive CML with the non-symmetric map $f(x) = \nu\, x(1 - x^2) + p$ with $\nu = 1.01$ and $p = -0.0001$. The solid line represents the velocity computed numerically iterating 10 000 times a 200 sites lattices and the dashed line represents the continuum approximation (3.9). (b) Amplification of the lower-left corner of (a) showing the continuation of the non-propagating solution up to $\varepsilon_c \simeq 0.00575$ for the numerical computation.

and that

$$\int_{-\infty}^{+\infty} \nabla f(h(z))\, dz = 0$$

since we are dealing with step states, the velocity v is approximately given by

$$v = \frac{1}{x_+^* - x_-^*} \int_{-\infty}^{+\infty} (h(z) - f(h(z)))\, dz. \tag{3.7}$$

Thus, taking an antisymmetric local map f results in a symmetric profile h and the velocity computed with (3.7) vanishes. It is clear then that f has to be non-antisymmetric if we want the front to propagate in a diffusive CML. An analogous analysis in a continuous space-time model of chemical reactions had led to similar conclusions [48].

Let us consider then an non-symmetric map, the perturbed cubic map:

$$f(x) = \nu\, x(1 - x^2) + p, \tag{3.8}$$

where $1 < \nu < 2$, while $|p| \ll 1$ breaks the symmetry. For this map a similar analysis than the one for the symmetric cubic map may be performed and it is possible to find an approximation for the velocity of the corresponding travelling front given by [39, 49]:

$$v \simeq -\frac{3p}{2}\frac{\sqrt{\nu\varepsilon}}{\nu - 1}. \tag{3.9}$$

In figure 3.10 we plot the velocity of the travelling wave front for $\nu = 1.01$ and $p = -0.0001$ computed numerically (solid line) and using the continuum approach (3.9) (dashed line). The continuum approximation gives a good fit. However, it does not reproduce the lack of propagation for very small values of ε. Figure 3.10.b depicts a magnification of figure 3.10.a around $\varepsilon = 0$ showing the discrepancy between the numerical experiment where $v(\varepsilon) = 0$ for $\varepsilon \leq \varepsilon_c \simeq 0.00575$, and the approximation (3.9) where the transition occurs at $\varepsilon_c = 0$.

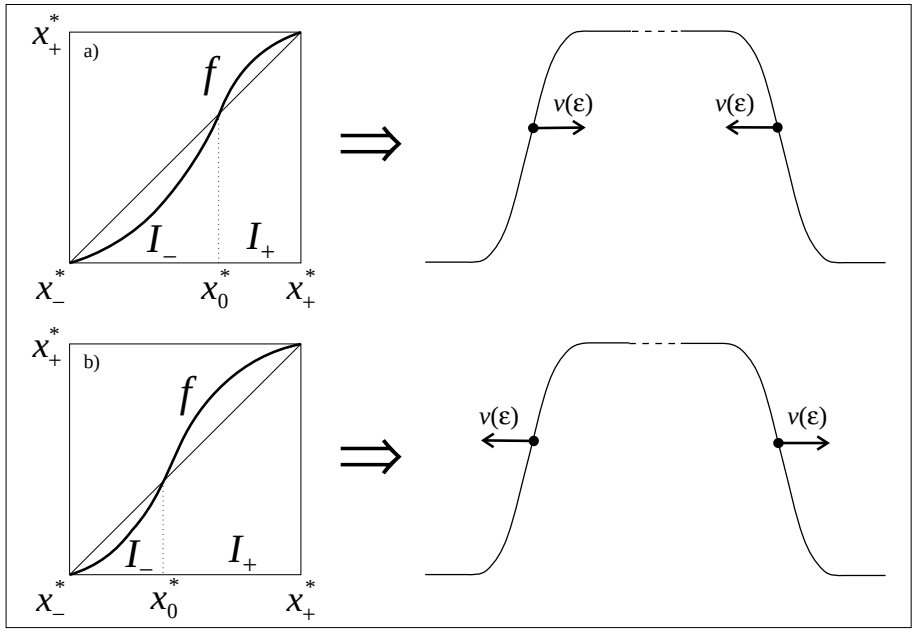

Figure 3.11: Travelling direction of an interface in a diffusive CML. (a) $|I_-| > |I_+|$: the kink shrinks and (b) $|I_-| < |I_+|$: the kink grows.

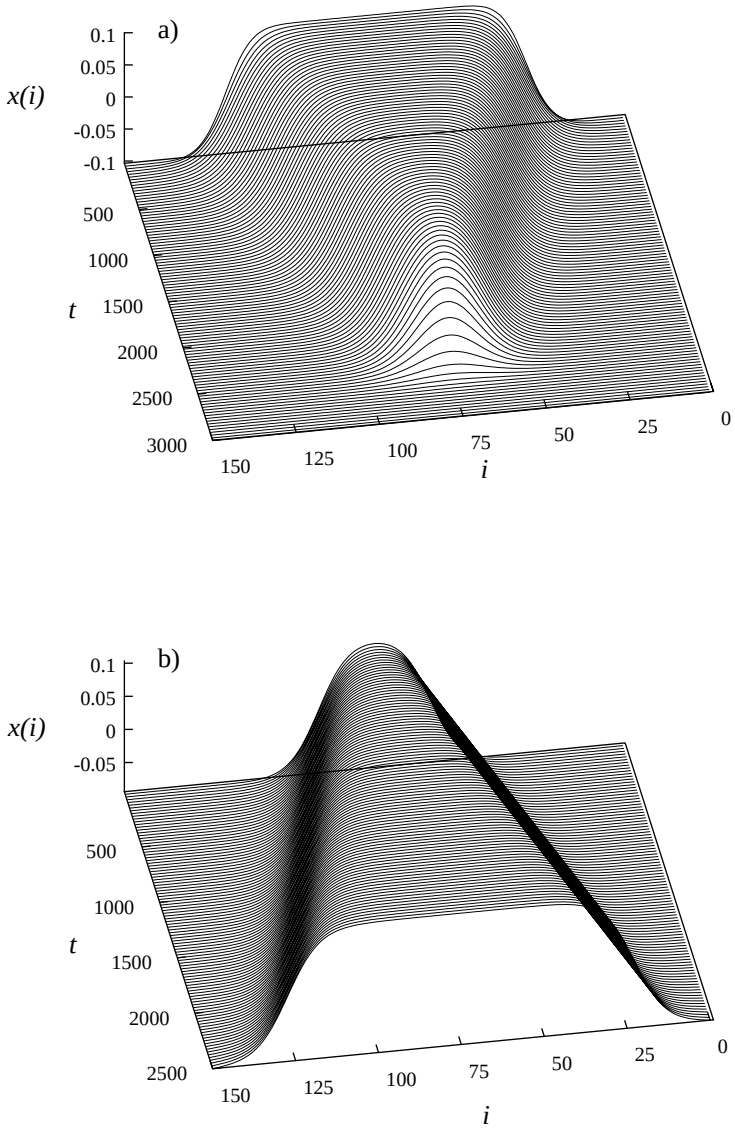

Figure 3.12: Propagating kink in a diffusive CML with the asymmetric local map (3.8) with $\nu = 1.01$ and $\varepsilon = 0.9$. (a) $p = -0.0001$: the kink solution shrinks (see figure 3.11.a) and (b) $p = +0.0001$: the kink solution grows (see figure 3.11.b).

In a diffusive CML the direction of travel of the interface is determined by the asymmetry. An important issue is the size of the basins of attraction $I_{\pm}$. If $|I_-| > |I_+|$ it is easier for a site to go from I_+ to I_- than the other way around, while if $|I_-| < |I_+|$ the opposite happens. The situation is depicted in figure 3.11, where the two cases are shown: (a) if $|I_-| > |I_+|$ the kink solution shrinks since the left (right) interface travels to the right (left) and (b) if $|I_-| < |I_+|$ the kink solution grows. In order to illustrate this phenomenon we plotted in figure 3.12 the evolution of the kink configuration with the asymmetric cubic map (3.8) for (a) $p = -0.0001$ and (b) $p = +0.0001$. Figure 3.12.a represents the case (a) in figure 3.11.a and figure 3.12.a the case (b). On the other hand, the coupling is symmetric, and thus the velocity of the left interface and the right one have the same magnitude but opposite directions, as it may be noticed in figure 3.12.

3.4 Mode-locking of the travelling velocity: first numerical evidence

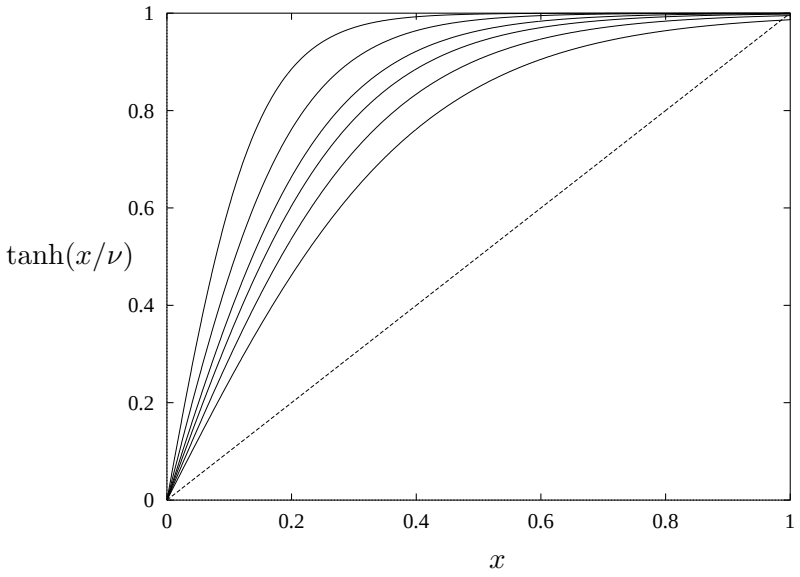

Figure 3.13: The hyperbolic tangent local map $f(x) = \tanh(x/\nu)$ ($\nu = 2/5, 1/3, 2/7, 1/4, 1/5, 1/7$ from right to left) used in figure 3.14.

In this chapter a simple mechanism for propagating interfaces in CMLs (one-way or diffusive) has been qualitatively described. The numerical experiments shown up to now (figures 3.10 and 3.5) seem to suggest smooth dependence of the velocity v as a function of ε with only one critical transition from the stationary state ($v(\varepsilon) = 0$) to the propagating solution at $\varepsilon_c > 0$ for the diffusive CML and two transitions (at $\varepsilon_c > 0$ and $1-\varepsilon_c$) for the one-way CML. In this section we give some numerical evidence of a quite striking phenomenon: *mode-locking* of the velocity of a travelling interface in CMLs. By mode-locking we understand that the velocity of the interface remains with the same value v_{lock} in the interval $[\varepsilon_1, \varepsilon_2]$ with $\varepsilon_1 < \varepsilon_2$.

As a first example, we used a one-way CML with the hyperbolic tangent $f(x) = \tanh(x/\nu)$ as local map (see figure 3.13); the results are shown in figure 3.14 for different values of the parameter ν. The velocity presents finite ε-regions where the velocity is locked to a

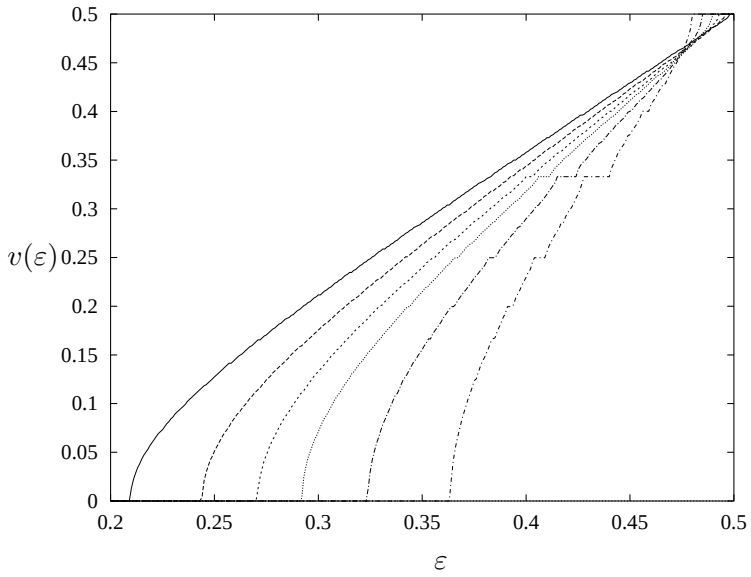

Figure 3.14: Velocity of the travelling interface for the hyperbolic tangent local map of figure 3.13 with $\nu = 2/5, 1/3, 2/7, 1/4, 1/5, 1/7$ from left to right. The velocity shows plateaus where the velocity is locked. The plateaus become larger as ν decreases.

particular value. The velocity curve corresponding to $\nu = 2/5$ (left-most one) does not apparently features any plateaus. However, as we decrease ν (curves going from left to right) the plateaus become more and more evident, and appear at the same heights for all the curves. A closer look reveals that they correspond to rational values of $v(\varepsilon)$.

Mode-locking implies the velocity to have a much more complex structure that the one previously described. It possesses several critical transitions as ε is varied. To understand this mode-locking phenomenon in detail we introduce, in the next chapter, the simplest local map that fulfills the basic conditions for supporting travelling wave fronts: a particular piece-wise linear local map for which the dynamics of the whole lattice is reduced to a one-dimensional map.

Chapter 4

A piece-wise linear local map: towards understanding the mode-locking phenomenon

In this chapter a piece-wise linear local map is introduced in order to analyze the mode-locking of the travelling velocity of interfaces in a one-way CML. We found the velocity to have an infinite number of critical transitions: it is indeed a Devil's staircase. The lattice dynamics is reduced to a one-dimensional circle map which is described using symbolic dynamics.

4.1 The piece-wise linear local map

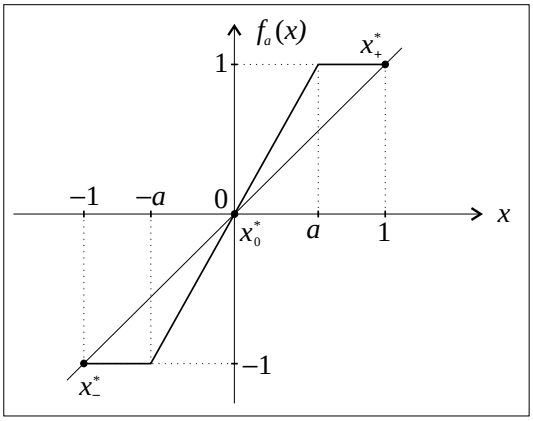

Figure 4.1: The simplest local map that allows travelling interfaces in one-way CML: the piece-wise linear local map f_a.

In the previous chapter we have described a very simple mechanism, allowing travelling interfaces in one-way CMLs consisting of a bistable local map. We now introduce a particularly simple example of a bistable local map that fulfills the following requirements: it is continuous, non-decreasing and has two superstable fixed points $x_\pm^*$, symmetric with respect to the unstable point x_0^*. We ask the fixed points $x_\pm^*$ to be superstable in order the travelling interface to be stable to perturbations and we require, without loss of generality, that

$x^*_- < x^*_+$. The simplest map of this kind is given by the 2-parameter family (see figure 4.1)

$$f_a(x) = \begin{cases} -1 & \text{if} \quad x \le -a \\ \frac{1}{a}\, x & \text{if} \quad -a < x < a \qquad 0 < a \le 1, \\ 1 & \text{if} \quad x \ge a \end{cases} \tag{4.1}$$

and by the step function between -1 and 1 centered at the origin with $f_a(0) = 0$ when $a = 0$. The fixed points $x^*_- = -1$ and $x^*_+ = 1$ are then superstable, with basins $I_- = [-1, 0)$ and $I_+ = (0, 1]$ respectively, and the repeller is the origin $x^*_0 = 0$. The coupled map lattice now depends on the two parameters ε and a, and the parameter space is the unit square. The one-way CML with local mapping f_a and coupling ε will be denoted by $F_{\varepsilon,a}$:

$$\begin{aligned} F_{\varepsilon,a}: \quad \mathbb{R}^{\infty} &\longrightarrow \mathbb{R}^{\infty} \\ X_{t+1} = \{x_{t+1}(i)\}_{i=-\infty}^{+\infty} &= F_{\varepsilon,a}\left(X_t = \{x_t(i)\}_{i=-\infty}^{+\infty}\right) \\ \text{s.t. } \forall\, i \in \mathbb{Z}, \quad x_{t+1}(i) &= (1-\varepsilon)\, f_a(x_t(i)) \,+\, \varepsilon f_a(x_t(i-1)). \end{aligned} \tag{4.2}$$

We partition the interval $I = [-1, 1]$ into the unstable domain $U = (-a, a)$ and the superstable domains $S_- = [-1, -a]$ and $S_+ = [a, 1]$. Any site falling within $S_\pm$ maps, under f_a, to $x^*_\pm$ at the next iteration. With this piece-wise linear local map the mode-locking is much more obvious as it may be observed in figure 4.2 where velocity curves as a function of ε are shown for several values of the local map parameter a.

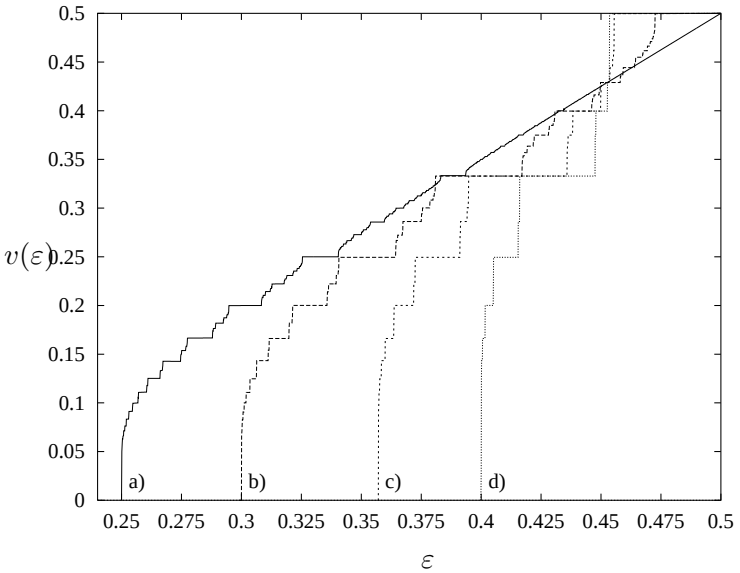

Figure 4.2: Velocity curves for the piece-wise linear local map as a function of ε for the following a values: a) $a = 1/2$, b) $a = 2/5$, c) $a = 2/7$ and d) $a = 1/5$.

We begin considering localized states of minimal mass X_t whose configurations $\{x_t(i)\}$ form a *non-decreasing* sequence. The case of a non-increasing configuration could be treated in the same way since the map f_a is antisymmetric w.r.t. x^*_0. Because X_t is a localized state, only a finite number n of local states belong to U (see figure 4.3.a), namely

$$i \in \{k+1, \ldots, k+n\} \quad \Longleftrightarrow \quad x_t(i) \in U. \tag{4.3}$$

For $i \leq k$ ($i > k+n$), the local states belong to the superstable domain S_- (S_+) and their image under f_a is -1 ($+1$). Consequently, if we let X'_t be the state obtained from X_t by replacing $x_t(i)$ with -1 for $i \leq k$ and with $+1$ for $i > k+n$, then $F_{\varepsilon,a}(X_t) = F_{\varepsilon,a}(X'_t)$. The state X'_t is said to be the *reduced state* associated with X_t, and we write $X_t \sim X'_t$ (see figure 4.3). We will reduce all states after each iteration of the mapping $F_{\varepsilon,a}$.

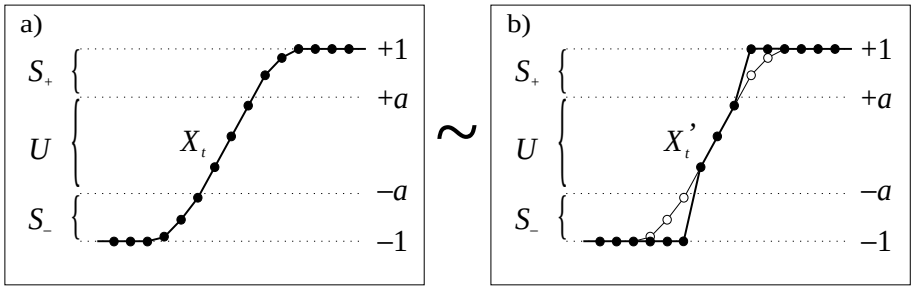

Figure 4.3: Reducing a minimal mass state. (a) A minimal mass state has a finite number of sites in U, (b) the remaining sites are reduced to -1 ($+1$) if they belong to S_- (S_+).

So, without loss of generality, we shall restrict our attention to states of the type

$$X_t = (\ldots, -1, -1, x_t(k+1), \ldots, x_t(k+n), 1, 1, \ldots) \tag{4.4}$$

where

$$x_t(i) \in U, \quad i = k+1, \ldots, k+n.$$

The number n of local states in U is called the *size* of X_t. Thus, the non-trivial part of X_t consists of the set of sites belonging to U giving the transition between the the stable local states x^*_- and x^*_+, this set is precisely defined as the *interface*. In more general terms, when the reduction of the states is not possible —that is the case when the local map does not have the superstable domains $S_\pm$— the interface is defined as the whole set of sites, belonging to the open interval (x^*_-, x^*_+), giving the transition between the stable local states x^*_- and x^*_+ (see figure 4.4).

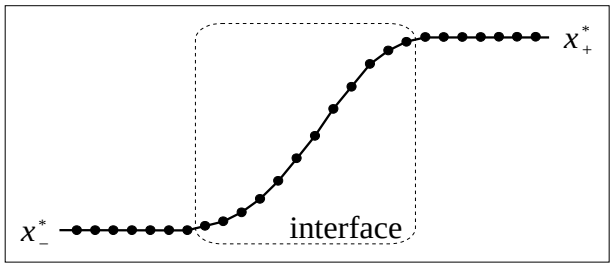

Figure 4.4: The interface of a minimal mass step state

The knowledge of the range (4.3) provides useful information about position and width of a step state. In fact, it is easy to show that the centre of mass of X_t satisfies the bounds

$$k + \frac{n(1-a)}{2} < \mu(X_t) < (k+n) - \frac{n(1-a)}{2}$$

and the width

$$\frac{n(1-a)}{2} < \sigma(X_t) < \frac{n}{2}.$$

Let us follow the dynamics of $F_{\varepsilon,a}$ by iterating the configuration (4.4). The image of X_t is

$$X_{t+1} = (\dots, -1, -1, x_{t+1}(k+1), \dots, x_{t+1}(k+n), x_{t+1}(k+n+1), 1, \dots), \qquad (4.5)$$

and its size is at most one bigger $(n+1)$ that the one for X_t. We say at most because X_{t+1} has not yet being reduced and therefore its size could have, after reduction, a smaller value. In order to compute X_{t+1} in (4.5) we have to apply the recipe $x_{t+1}(i) = (1-\varepsilon)f(x_t(i)) - \varepsilon f(x_t(i-1))$ to every site. Nevertheless, the first $(k+1)$ and the last $(k+n+1)$ non-trivial sites of X_{t+1} have a simpler form:

$$\begin{aligned} x_{t+1}(k+1) &= (1-\varepsilon)f(x_t(k+1)) - \varepsilon \\ x_{t+1}(k+n+1) &= (1-\varepsilon) - \varepsilon f(x_t(k+n)) \end{aligned}$$

since they are in the boundary of the interface where the neighbouring sites $x_t(k) = -1$ and $x_t(k+n+1) = 1$ simplify, respectively, to -1 and 1 under iteration of f_a. Thus, defining the linear maps

$$\begin{aligned} f_0(x) &\equiv \frac{1-\varepsilon}{a}\, x - \varepsilon \\ f_1(x) &\equiv \frac{\varepsilon}{a}\, x + (1-\varepsilon), \end{aligned} \qquad (4.6)$$

it is possible to rewrite (4.5) as

$$X_{t+1} = (\dots, -1, -1, f_0(x_t(k+1)), x_{t+1}(k+2), \dots, x_{t+1}(k+n), f_1(x_t(k+n)), 1, \dots).$$

As we said, X_{t+1} has at most $n+1$ sites in U. The reduced state X'_{t+1} is then one of the following (see figure 4.5):

$$\begin{aligned} &(a)\ (\dots, -1, -1, x_{t+1}(k+1), x_{t+1}(k+2), \dots, x_{t+1}(k+n), \quad 1, \quad 1, \dots) \\ &(b)\ (\dots, -1, -1, x_{t+1}(k+1), x_{t+1}(k+2), \dots, x_{t+1}(k+n), x_{t+1}(k+n+1), 1, \dots) \\ &(c)\ (\dots, -1, -1, \quad -1, \quad x_{t+1}(k+2), \dots, x_{t+1}(k+n), x_{t+1}(k+n+1), 1, \dots) \\ &(d)\ (\dots, -1, -1, \quad -1, \quad x_{t+1}(k+2), \dots, x_{t+1}(k+n), \quad 1, \quad 1, \dots) \end{aligned} \qquad (4.7)$$

In figure 4.5 we illustrate the simplest example, when only one site, at each boundary of the interface, is allowed to change from one basin of attraction to another. In general this picture is more complex since for one iteration there may be several sites interchanging basins at each end of the interface. However, the configuration remains a non-decreasing sequence (minimal mass state) since f_a is non-decreasing (proposition 2.1.1). The size of the interface is n in cases (a) and (c), $n+1$ in case (b) and $n-1$ in case (d). Loosely speaking, as the time increases from t to $t+1$, the state has not propagated in case (a), it has advanced to the right in case (c), it has propagated with dispersion in case (b) and it has shrunk without propagation in case (d).

To decide among these 4 possibilities, one needs to investigate the value of f_0 and f_1 at the boundary sites $i = k+1$ and $i = k+n$, respectively. Defining

$$\gamma_- \equiv \frac{a(\varepsilon - a)}{1-\varepsilon}, \qquad \gamma_+ \equiv \frac{a(a+\varepsilon-1)}{\varepsilon} \qquad (4.8)$$

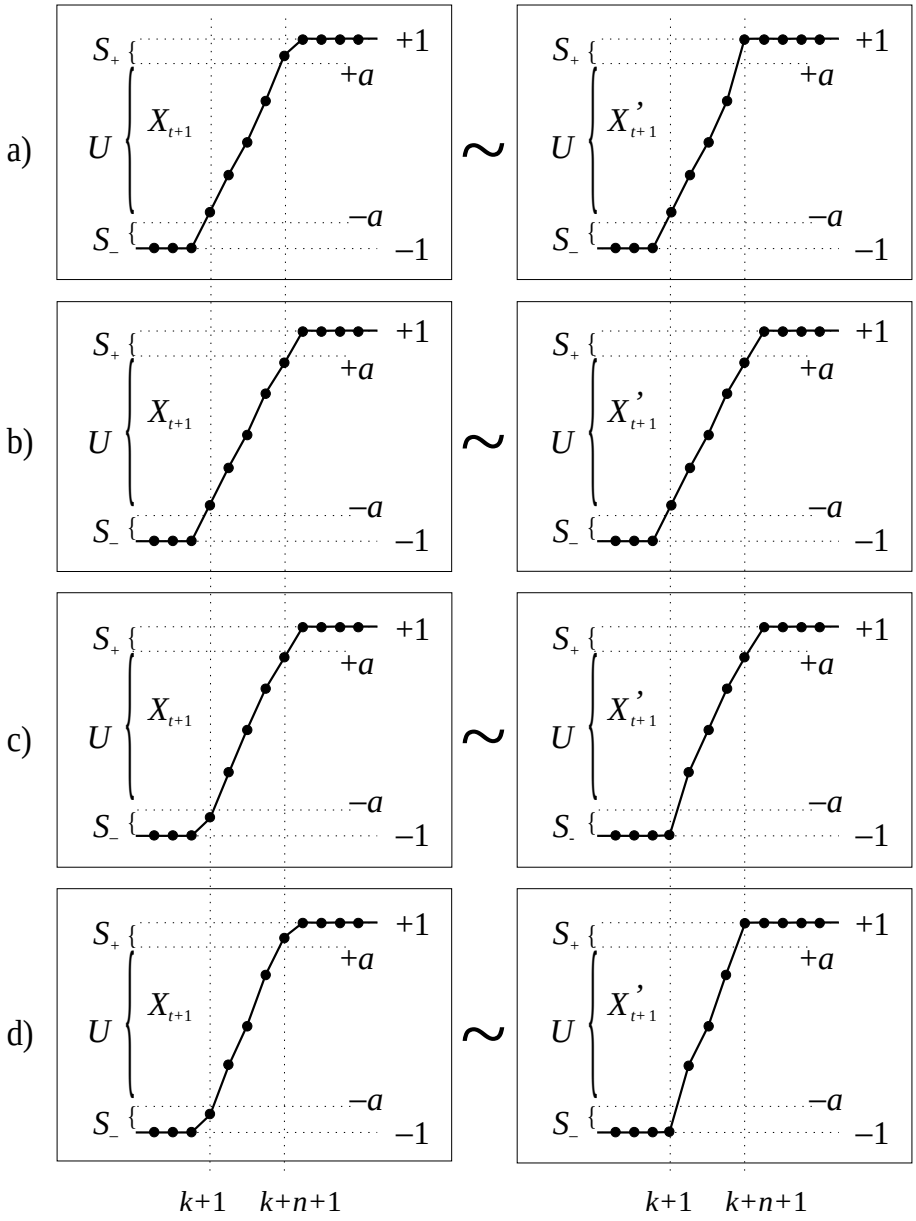

Figure 4.5: Reduction of the state X_{t+1} where 4 different cases are possible depending on the combination of the extremes sites of the interface.

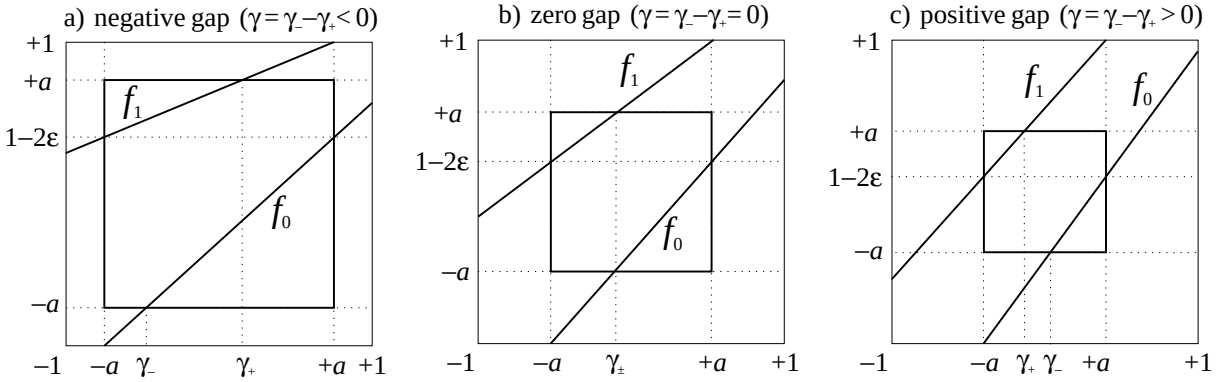

Figure 4.6: The maps f_0 and f_1 defining the dynamics at the ends of the interface.

one verifies that the functions f_0 and f_1 satisfy the following equations (see figure 4.6)

$$\begin{aligned} f_0(-a) &= -1 & f_1(-a) &= 1-2\varepsilon \\ f_0(a) &= 1-2\varepsilon & f_1(a) &= 1 \\ f_0(\gamma_-) &= -a & f_1(\gamma_+) &= a. \end{aligned} \tag{4.9}$$

We define the *gap* of $F_{\varepsilon,a}$ to be the closed interval $\Gamma = [\gamma_+, \gamma_-]$. Its length (with sign) is given by

$$\gamma(\varepsilon, a) \;=\; \gamma_- - \gamma_+ \;=\; \frac{a(1-a-2\varepsilon(1-\varepsilon))}{\varepsilon(1-\varepsilon)}. \tag{4.10}$$

We will often omit the arguments (ε, a) and refer to the gap as γ. Let us consider first states having only one site in the unstable regime U.

4.2 The auxiliary map and its symbolic dynamics

In this section we reduce the dynamics of the whole lattice to a one-dimensional circle map that describes the evolution of the only site contained in the interface.

4.2.1 The auxiliary map for an increasing step state

Let us first consider an increasing step state, *i.e.* a step state with minimal mass. The simplest of all the configurations (4.4) is a state with at most one site in U, *i.e.* at most one site in the interface. We call these states *minimal mass 1-states* or *minimal 1-states* and they have the form

$$X_t = (\ldots, -1, -1, x_t(i), 1, 1, \ldots), \tag{4.11}$$

where either $x_t(i) \in U$ or $x_t(i) = -1$, for which we introduce the shorthand notation

$$X_t = [x, i]_t,$$

(the subscript t will often be dropped). Thus a pure step state (cf. (2.5)) is a particular case of a minimal 1-state, *i.e.* $[-1, i] = P(i)$. We would like to deal with minimal 1-states, but in general the image of a minimal 1-states is not again a minimal 1-state. Nevertheless it is possible to establish a region of the parameter space were the minimal 1-states are preserved under iteration:

Theorem 4.2.1 *If X_t is a minimal 1-state then so is X_{t+1}, provided that the gap size is non-negative.*

Proof. Suppose that X_{t+1} has two sites in U ($x_{t+1}(k)$, $x_{t+1}(k+1) \in U$). Because the coupling is with one neighbour, the minimal 1-state X_t is of the form $X_t = [x, k]_t$ (see figure 4.7).

In order that $X_{t+1} = F_{\varepsilon,a}(X_t)$ the images of $x_t(k)$ have to verify $x_{t+1}(k) = f_0(x_t(k)) \in U$, $x_{t+1}(k+1) = f_1(x_t(k)) \in U$ and $x_{t+1}(k) \leq x_{t+1}(k+1)$, that is

$$\begin{cases} -a < \frac{1-\varepsilon}{a}\, x_t(k) - \varepsilon \\ a > \frac{\varepsilon}{a}\, x_t(k) + (1-\varepsilon) \end{cases}$$

$$\Rightarrow \quad \frac{a(\varepsilon - a)}{1-\varepsilon} < x_t(k) < \frac{a(a-(1-\varepsilon))}{\varepsilon}$$

$$\Rightarrow \quad \frac{\varepsilon - a}{1-\varepsilon} < \frac{a-(1-\varepsilon)}{\varepsilon}$$

$$\Rightarrow \quad 1 - a - 2\varepsilon(1-\varepsilon) < 0$$

$$\Rightarrow \quad \frac{a(1-a-2\varepsilon(1-\varepsilon))}{\varepsilon(1-\varepsilon)} < 0$$

$$\Rightarrow \quad \gamma(\varepsilon, a) < 0.$$

Thus two sites in U implies that $\gamma(\varepsilon, a) < 0$ and therefore it is not possible for X_{t+1} to have two sites in U when the gap size is non-negative. □

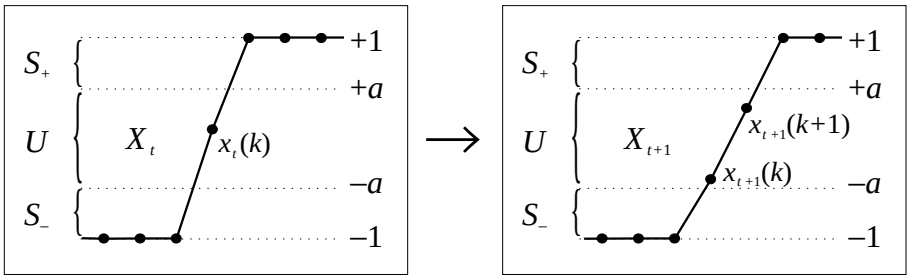

Figure 4.7: A minimal 1-state X_t going, after one iteration, to a state with two sites in the unstable regime U. (This does not happen when the gap size is positive ($\gamma(\varepsilon, a) \geq 0$).

Therefore if the gap size is non-negative the image of a minimal-1 state is a minimal 1-state. This fact will simplify enormously the global dynamics. On the other hand, when the gap size is negative it is possible for more than one site to be in U at the same iteration: nevertheless the interface dynamics can still be described in terms of one-dimensional maps via delay maps (see section 5.2).

We have characterized the (ε, a)-parameter region where the dynamics consists solely of minimal 1-states if starting with a minimal 1-state. A plot of this region is depicted in figure 4.8, lying below the zero-gap line, $\gamma(\varepsilon, a) = 0$. Let us now follow the evolution of a minimal 1-state in the positive-gap case. The image of X_t (cf. (4.11)) is given by

$$X_{t+1} = (\ldots, -1, -1, f_0(x_t(i)), f_1(x_t(i)), 1, \ldots). \tag{4.12}$$

Notice that X_{t+1} is given in terms of the new functions f_0 and f_1 (cf. (4.12)).

We define

$$\varepsilon_c = \frac{1-a}{2} \tag{4.13}$$

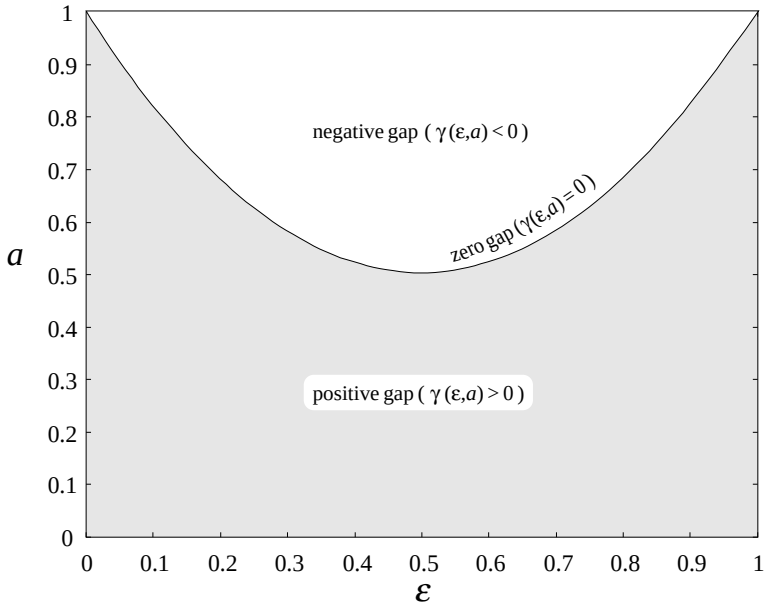

Figure 4.8: The parameter region where the minimal 1-states are preserved under iteration is the positive-gap region (shaded area). Above the zero-gap line ($\gamma(\varepsilon, a) = 0$) it is possible to have states with more than one site in U.

and note that ε_c is the area enclosed between the graph of f_a and the diagonal, for $x_0^* < x < x_+^*$. The following two results characterize completely the evolution of X_t in the parameter ranges $\varepsilon \leq \varepsilon_c$ and $\varepsilon \geq 1 - \varepsilon_c$.

Theorem 4.2.2 *Let X_t be a minimal 1-state of the form* (4.11)*, and consider the fixed points of f_0 and f_1 ($f_0(x_-) = x_-$ and $f_1(x_+) = x_+$)*

$$x_- = \frac{\varepsilon a}{1 - \varepsilon - a} \qquad x_+ = \frac{a(1-\varepsilon)}{a - \varepsilon}. \tag{4.14}$$

(i) If $\varepsilon \leq \varepsilon_c$, then for $x(i) < x_-$ ($x(i) > x_-$) the state $[x, i]$ reaches $P(i)$ ($P(i-1)$) in a finite time. The state $[x_-, i]$ is fixed and unstable.

(ii) If $\varepsilon \geq 1-\varepsilon_c$, then for $x(i) < x_+$ ($x(i) > x_+$) the state $[x, i]$ reaches $P(i+k)$ ($P(i+k-1)$) in a finite time. The state $[x_+, i]$ is fixed and unstable under $G \circ F$, where G is the shift mapping

$$G\left(\{x_t(i)\}\right) \,=\, \{x_t(i+1)\}.$$

Proof. (i) The image of the i-th site, if it remains in U, is given by $x_{t+k}(i) = f_0^k(x_t(i))$ since it is coupled to the $(i-1)$-th site whose value is -1. As to the $(i+1)$-th site, since $\varepsilon \leq \varepsilon_c$ and $a \leq f_1(x)$ for any $x \in U$, we have that $x_{t+k}(i+1) \in S_+$. Therefore at time $t+k$ the state of the lattice will be equivalent to $X_{t+k} = [f_0^k(x_t), i]$ which depends exclusively on the initial condition $x_t(i)$. If $\varepsilon \leq \varepsilon_c$ the derivative of the map $f_0'(x) = (1-\varepsilon)/a \geq 1$ and then f_0 has a repeller at x_-. Therefore $f_0^k(x_t(i))$ will decrease (increase), for $x_t(i) < x_-$ ($x_t(i) > x_-$) until it reaches S_- (S_+) when the state of the lattice is $P(i)$ ($P(i-1)$). For the marginal case $x_t(i) = x_-$ the state of the lattice $X_{t+k} = [f_0^k(x_-), i] = [f_0(x_-), i]$ is fixed and unstable since x_- is an unstable fixed point of f_0. A picture of these 3 situations is given in figure

4.9 where the cases $x(i) > x_-$, $x(i) = x_-$ and $x(i) < x_-$ correspond, respectively, to a black, grey and white site $x(i)$.

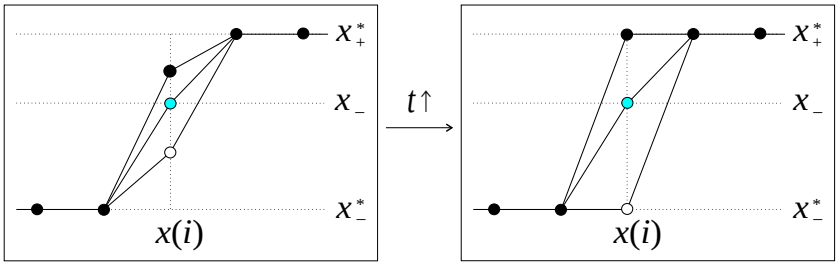

Figure 4.9: Dynamics of minimal 1-states for positive gap when $\varepsilon < \varepsilon_c$. The final state of the lattice is one of a pure step state $P(i-1)$ or $P(i)$ or it remains unchanged, but is unstable, when $x(i) = x_-$.

(ii) Using a similar reasoning, if $\varepsilon \geq 1 - \varepsilon_c$, x_+ is an unstable fixed point of f_1 and the state of the lattice at time $t+k$ is $X_{t+k} = [f_1^k(x_t), i+k]$. Therefore the lattice will reach the state $P(i+k)$ $(P(i+k-1))$ for $x_t(i) < x_+$ $(x_t(i) > x_+)$. In the marginal case $x_t(i) = x_+$, the state of the lattice is $X_{t+k} = G^k\left([f_1^k(x_+), i+k]\right) = G^k\left([f_1(x_+), i]\right)$, which is fixed and unstable under $G \circ F$. □

From Theorem 4.2.2 it follows that the velocity of the travelling interface satisfies

$$v(\varepsilon) = \begin{cases} 0 & \text{if} \quad 0 \leq \varepsilon \leq \varepsilon_c \\ 1 & \text{if} \quad 1 - \varepsilon_c \leq \varepsilon \leq 1 \end{cases} \tag{4.15}$$

where ε_c is the upper bound for the existence of the non-propagating wave front (see Theorem 2.2.3). At the other extreme, when ε is near 1, the interface propagates with a velocity equal to 1 and this case may be extended, from $\varepsilon = 1$ down to $\varepsilon \geq 1 - \varepsilon_c$. As a consequence, we have that if $\varepsilon \leq \varepsilon_c$ then $F_{\varepsilon,a}(P(i)) \sim P(i)$, and if $\varepsilon \geq 1 - \varepsilon_c$ then $F_{\varepsilon,a}(P(i)) \sim P(i+1)$. In the rest of this chapter we shall assume that $\varepsilon_c < \varepsilon < 1 - \varepsilon_c$.

We partition U into three intervals, namely

$$\begin{aligned} U_+ &= \{x : -a \leq x < \gamma_+\} \\ \Gamma \quad &= \{x : \gamma_+ \leq x \leq \gamma_-\} \\ U_- &= \{x : \gamma_- < x \leq a\}. \end{aligned}$$

Because we are assuming the gap length to be non-negative, we are dealing with a minimal 1-state and then the four possible configurations of the state (4.12) are reduced to three since the case of two coexisting sites in U is not attainable. Thus the three possibilities for the configuration (4.12) are

$$\begin{aligned} &(a) \;\; x_t \in U_- \quad \Rightarrow \quad f_0(x_t) \in U,\; f_1(x_t) \in S_+ \\ &(b') \;\; x_t \in \Gamma \quad \Rightarrow \quad f_0(x_t) \in S_-,\; f_1(x_t) \in S_+ \\ &(b) \;\; x_t \in U_+ \quad \Rightarrow \quad f_0(x_t) \in S_-,\; f_1(x_t) \in U. \end{aligned} \tag{4.16}$$

corresponding to the reduced states —see (4.7)

$$\begin{aligned}
(a) \quad & X_{t+1} = (\ldots, -1, -1, x_{t+1}, \ \ 1, \ \ 1, \ldots) \\
(b') \quad & X_{t+1} = (\ldots, -1, -1, \ -1, \ \ \ 1, \ \ 1, \ldots) \\
(b) \quad & X_{t+1} = (\ldots, -1, -1, \ -1, \ x_{t+1}, 1, \ldots)
\end{aligned}$$

depicted in figure 4.10.

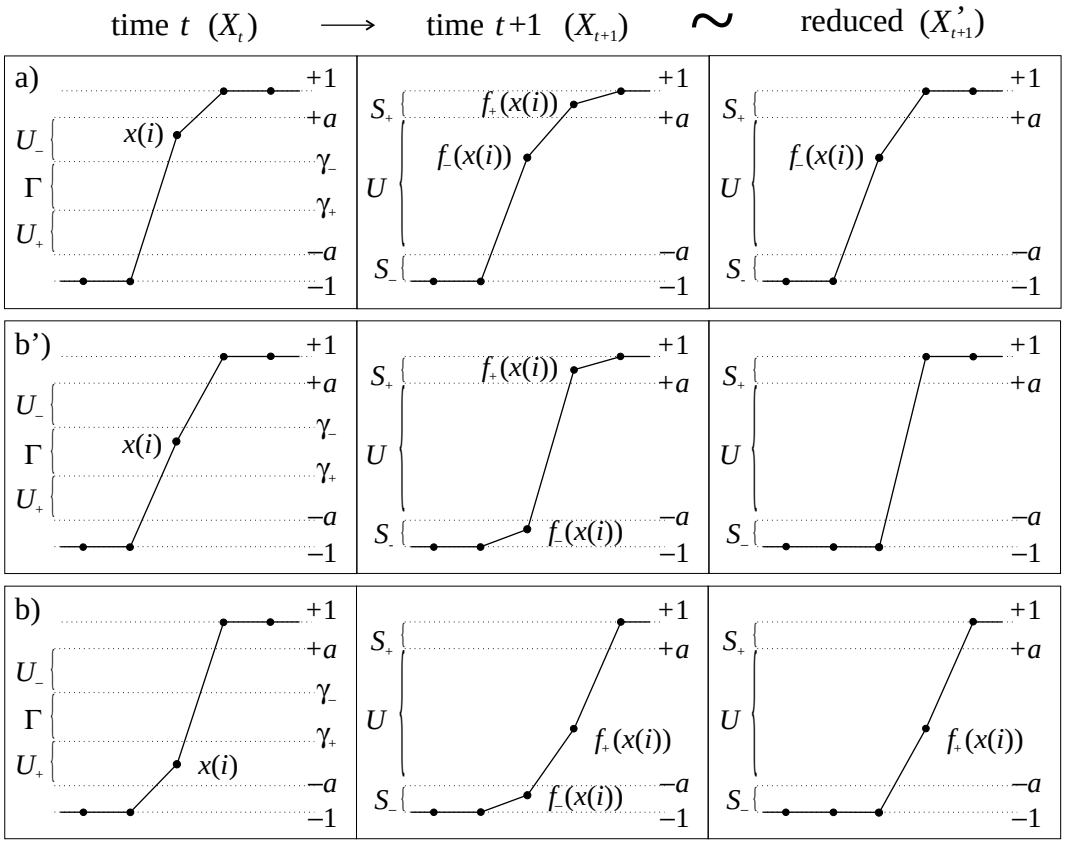

Figure 4.10: The 3 different possibilities of evolution for a minimal 1-state when the gap is non-negative and $\varepsilon_c < \varepsilon < 1 - \varepsilon_c$.

For the case (b') we have the evolution

$$[x, i]_t \longrightarrow [-1, i]_{t+1} \longrightarrow [1 - 2\varepsilon, i + 1]_{t+2}. \tag{4.17}$$

All possibilities are accounted for by defining the *auxiliary map* $\Phi_{\varepsilon,a}$ to be the 2-parameter map (see figure 4.11)

$$\Phi_{\varepsilon,a}(x) = \begin{cases} f_1(x) & \text{if } x \in U_+ \\ a & \text{if } x \in \Gamma \qquad \varepsilon_c < \varepsilon < 1 - \varepsilon_c. \\ f_0(x) & \text{if } x \in U_- \end{cases} \tag{4.18}$$

It is plain that $\Phi_{\varepsilon,a}$ maps U onto itself and if, in addition, γ is positive, then U_-, Γ and U_+ have positive measure. This characterizes the domain and range of $\Phi_{\varepsilon,a}$. The map $\Phi_{\varepsilon,a}$ is a

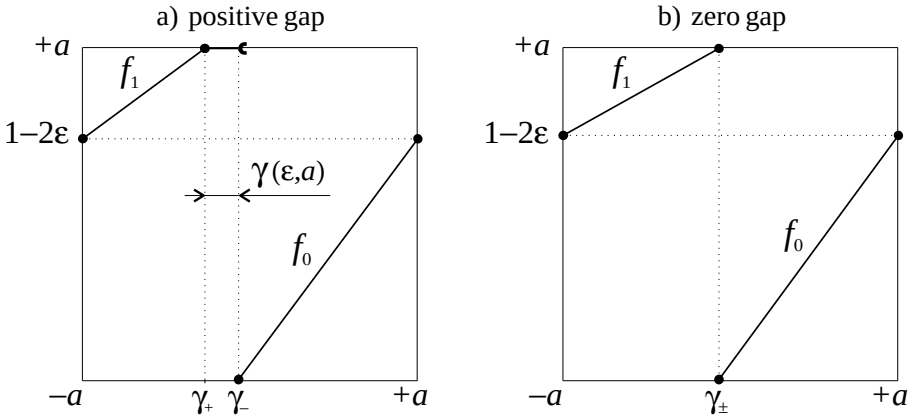

Figure 4.11: The auxiliary map $\Phi_{\varepsilon,a}$.

circle map because from the periodicity condition $\Phi(-a) = \Phi(a) = 1 - 2\varepsilon$ it can be made to map the circle of diameter $2a$ into itself. The evolution (4.17) is determined by the flat region $\Phi(\Gamma) = a$ since $\Phi(\Phi(\Gamma)) = \Phi(a) = 1 - 2\varepsilon$. It is worth mentioning that instead of choosing the value of $\Phi(\Gamma) = a$ we may have used $\Phi(\Gamma) = -a$ since after a further iteration both a and $-a$ are mapped to $1 - 2\varepsilon$ by Φ. The reason for this arbitrariness becomes clear in the next section.

The auxiliary map reduces the dimensionality of our system. The global map $F_{\varepsilon,a}$ is an infinite dimensional system since it has an infinite number of sites. But in the case of minimal 1-states for non-negative gap the dynamics of the whole lattice is reduced to that of the auxiliary map $\Phi_{\varepsilon,a}$, as illustrated schematically in figure 4.12. Iterating $F_{\varepsilon,a}$ q times amounts to applying the auxiliary map q times on the interface site. During these q iterations, whenever the branch f_0 is used the interface is not shifted; whenever f_1 is applied we shift the interface by one site to the right; and finally, when the interface site falls into the gap Γ it essentially undergoes two iterations —cf. (4.17)— to end up with the value $1 - 2\varepsilon$ as well as being shifted one site to the right.

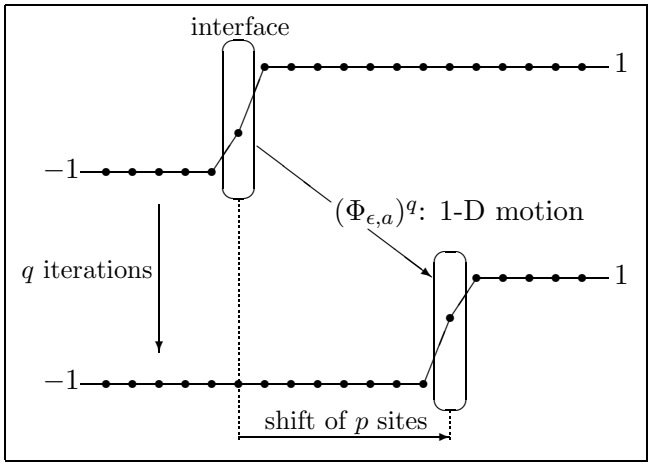

Figure 4.12: Reduction of the dynamics of the travelling front for minimal 1-states via the auxiliary map $\Phi_{\varepsilon,a}$.

Thus the dynamics of $F_{\varepsilon,a}$ for minimal 1-states, when the gap size is non-negative, is accounted for by the auxiliary map $\Phi_{\varepsilon,a}$. The nature of the auxiliary map (piece-wise linear) suggests a symbolic dynamics description.

4.2.2 The auxiliary map for a decreasing step state

Let us now consider a decreasing step state of the form

$$X_t = (\ldots, 1, 1, x_t(i), -1, -1, \ldots), \tag{4.19}$$

which is the simplest configuration for a decreasing step state. The state (4.19) is mapped to

$$X_{t+1} = (\ldots, 1, 1, g_0(x_t(i)), g_1(x_t(i)), -1, \ldots). \tag{4.20}$$

where

$$\begin{aligned} g_0(x) &\equiv \frac{1-\varepsilon}{a}\, x + \varepsilon \\ g_1(x) &\equiv \frac{\varepsilon}{a}\, x - (1-\varepsilon). \end{aligned} \tag{4.21}$$

The dynamics is then reduced to the auxiliary map (see figure 4.13)

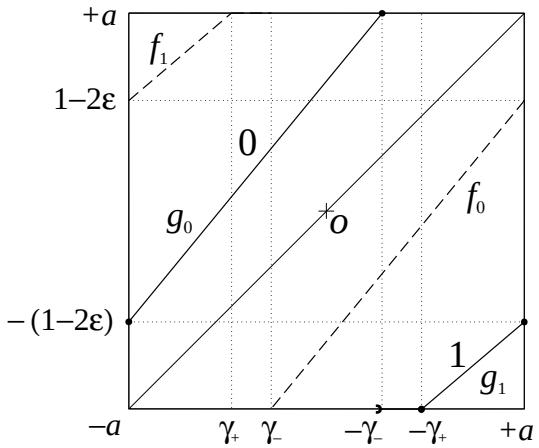

Figure 4.13: The auxiliary map $\Upsilon_{\varepsilon,a}$ accounting for the dynamics of the interfacial site for a decreasing step state.

$$\Upsilon_{\varepsilon,a}(x) = \begin{cases} g_0(x) & \text{if } -a \le x \le -\gamma_- \\ -a & \text{if } -\gamma_- < x < -\gamma_+ \\ g_1(x) & \text{if } -\gamma_+ < x \le a \end{cases} \qquad \varepsilon_c < \varepsilon < 1 - \varepsilon_c. \tag{4.22}$$

It is easy to show that g_0 is the symmetric version of f_0 (with respect to the origin $O = (0, 0)$) and similarly for g_1 and f_1. Thus the dynamics of a decreasing step state is the symmetric counterpart of that of an increasing step state. As a consequence, the velocity of propagation and shape (just symmetrized) of a decreasing and an increasing step state are equal.

4.2.3 Symbolic dynamics of minimal 1-states

We develop a symbolic description of the dynamics of minimal 1-states in the case of non-negative gap length. Their dynamics can be reduced to the iteration of a one-dimensional piece-wise linear circle map —the auxiliary map $\Phi_{\varepsilon,a}$. The following binary symbolic dynamics for the auxiliary map $\Phi_{\varepsilon,a}$ will play a decisive role in the rest of this chapter. This approach is quite standard when dealing with circle maps (cf. [50, 51]).

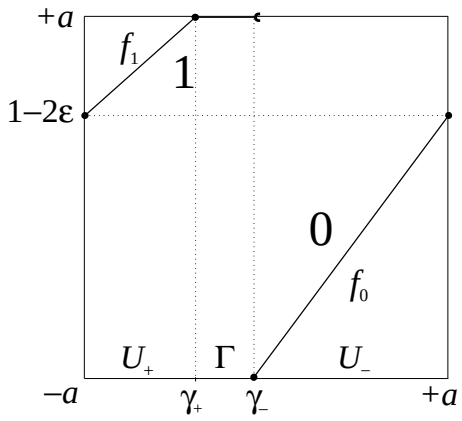

Figure 4.14: Symbolic dynamics of the auxiliary map. An iteration falling in the upper (lower) branch of Φ is given the symbol '1' ('0').

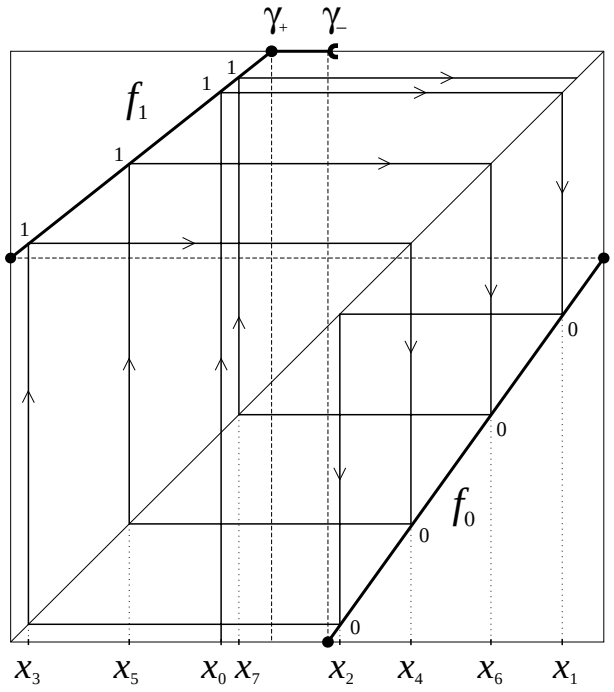

Figure 4.15: Symbolic dynamics for an orbit of the auxiliary map. The initial point x_0 is iterated under Φ and we obtain the semi-infinite sequence of symbols $S(x_0) = (1, 0, 0, 1, 0, 1, 0, 1, \ldots)$.

We assign the symbols '0' to U_-, the symbol '1' to U_+, and again the symbol '1' to Γ, see figure 4.14, thus the upper branch of Φ (f_1 and gap) is coded with '1' and the lower branch (f_0) with '0'. This choice originates from the prescriptions (4.16), according to which the location of a minimal 1-state remains unchanged for $x \in U_-$, increases by one for $x \in (U_+ \cup \Gamma)$. To the orbit of the auxiliary map with initial condition x we associate the semi-infinite sequence of symbols (see figure 4.15 for an example)

$$S = S(x) = (s_1, s_2, s_3, \dots)$$

where

$$s_i = \begin{cases} 1 & \text{if} \quad \Phi^i(x) \in (U_+ \cup \Gamma) \\ 0 & \text{if} \quad \Phi^i(x) \in U_- \end{cases} .$$

The space of binary sequences is denoted by Σ_2, and is equipped with the usual topology.

Any orbit with an element in Γ will be called a *gap orbit*. If this orbit is periodic, then the period of its symbolic representation is that of the orbit. Because every '1' in S accounts for a global displacement of the front by one site it is possible to compute the velocity of the travelling front by counting the fraction of '1"s in the binary sequence, namely

$$v(\varepsilon, a) = \lim_{T\to\infty} \frac{1}{T} \sum_{t=0}^{T} s_t \tag{4.23}$$

provided that the limit exists. If this is the case, it is plain that $0 \leq v(\varepsilon, a) \leq 1$. The right hand side of equation (4.23) is equivalent to the rotation number of the auxiliary map (see next section).

We will show that the symbol sequence $S(x)$ can be characterized in terms of the *spectrum* of $v(\varepsilon, a)$, which is defined as the following sequence of integers

$$Spec(v) \;=\; \lfloor 0 \times v \rfloor, \lfloor 1 \times v \rfloor, \lfloor 2 \times v \rfloor, \;\dots\; = \; (a_0, a_1, a_2, \;\dots) \tag{4.24}$$

where $\lfloor \cdot \rfloor$ is the floor function. The elements of $Spec(v(\varepsilon, a))$ are arranged in increasing order and they differ by zero or one since $0 \leq v(\varepsilon, a) \leq 1$. Thus defining

$$\tau(a_1, a_2, \dots) = (a_1 - a_0, a_2 - a_1, a_3 - a_2, \dots),$$

we find that $\tau(Spec(v(\varepsilon, a)))$ is a binary sequence.

Using symbolic dynamics it is easy to follow the evolution of the minimal 1-state: every iteration corresponds to a new symbol in the sequence. If the symbol is '0' then the minimal 1-state remains in the same site and if the symbol is '1' the minimal 1-state is shifted one site to the right. If we assume the velocity of the travelling front to be constant, so that the spectrum of the velocity gives the integer position of the minimal 1-state at every iteration —the location of the minimal 1-state can only take integer values. Thus τ applied on $Spec(v(\varepsilon, a))$ gives a '0' when the position of the minimal 1-state remains unchanged and a '1' when it jumps one site to its right neighbour. This is exactly what the symbolic sequence S gives, therefore the symbolic binary sequence associated to a given velocity $v(\varepsilon, a)$ can be computed as

$$S = \tau \left(Spec(v(\varepsilon, a)) \right). \tag{4.25}$$

If $v(\varepsilon, a)$ is rational, then $\tau(Spec(v(\varepsilon, a)))$ is periodic, as is easily verified. For example, the sequence $S(3/7)$ is given by, see figure 4.16,

$$\begin{aligned} S(3/7) &= \tau\left(Spec(3/7)\right) \\ &= \tau(0,0,0,1,1,2,2,3,\ldots) \\ &= (\overline{0,0,1,0,1,0,1}), \end{aligned}$$

where the bar denotes periodicity. From now on we will drop the bar, representing the symbolic sequence for a rational velocity by just one period.

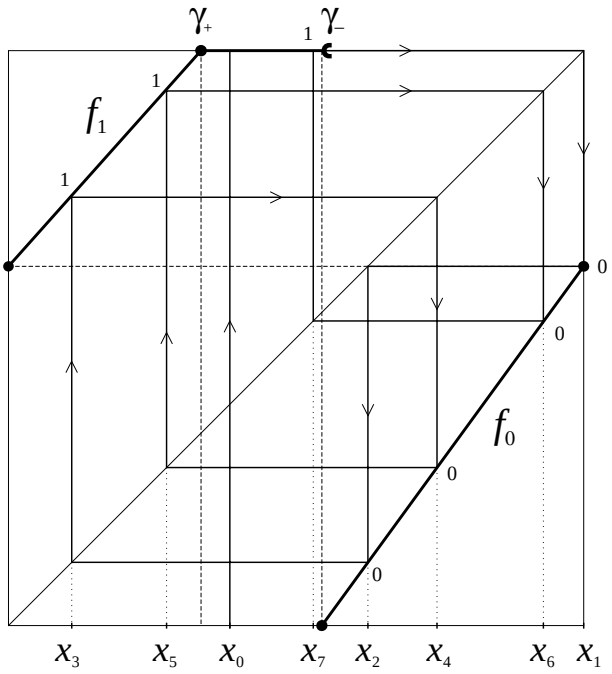

Figure 4.16: Symbolic dynamics for a periodic orbit of the auxiliary map. The periodic sequence of symbols is $S(x_0) = (\overline{0,0,1,0,1,0,1})$.

The symbolic dynamics of $\Phi_{\varepsilon,a}$ is then that of a uniform rotation with rotation number $v(\varepsilon, a)$ analogous to that of a homeomorphism of a circle map, as we shall see in section 4.4. We will denote the iterations of the auxiliary map as follows. Every time the upper branch is used we denote the applied function by f_1, and f_0 when the lower branch is used. An orbit through Φ is then a multiple composition of f_0's and f_1's depending on its symbolic coding. We simplify further the notation by defining

$$f_{S(x)}(x) = f_{s_1,s_2,\ldots,s_p} \equiv f_{s_p}\left(f_{s_{p-1}}\left(\ldots f_{s_2}(f_{s_1}(x))\ldots\right)\right). \tag{4.26}$$

As an example let us write the iteration of an initial point x_0 through the periodic symbolic sequence obtained from $v = 3/7$:

$$\begin{aligned} f_{S(v=3/7)}(x_0) &= f_{0010101}(x_0) \\ &= f_1\left(f_0\left(f_1\left(f_0\left(f_1\left(f_0\left(f_0(x_0)\right)\right)\right)\right)\right)\right). \end{aligned}$$

Thanks to equation (4.26) it is possible to represent explicitly the dynamics of an orbit starting at x_0 in a compact way.

4.3 The travelling velocity

Using the equivalence between the rotation number of Φ and the velocity $v(\varepsilon, a)$ we show that the latter exists, independently from the initial state, is continuous with respect to the parameters (ε, a) and, is a non-decreasing function of ε.

4.3.1 Existence of the travelling velocity

The auxiliary map Φ maps the interval $[-a, a]$ onto itself. Let us define a *lift* [52, 53] of Φ as $\Psi : \mathbb{R} \to \mathbb{R}$ such that $\pi\Psi(x) = \Phi\pi(x)$, where $\pi(x) = x \,(\mathrm{mod}\, 2a)$ is the standard projection from the real line to the circle of circumference $2a$. The lift Ψ is not unique, we chose then the following form

$$\begin{aligned} &\Psi : \mathbb{R} \to \mathbb{R} \\ &\Psi(x) = \Phi(x - 2a\, k_1(x)) + 2a\, k_2(x) \end{aligned} \tag{4.27}$$

where $k_1(x)$ is the integer such that $-a \le x - 2a\, k_1(x) < a$ and $k_2(x)$ is the smallest integer

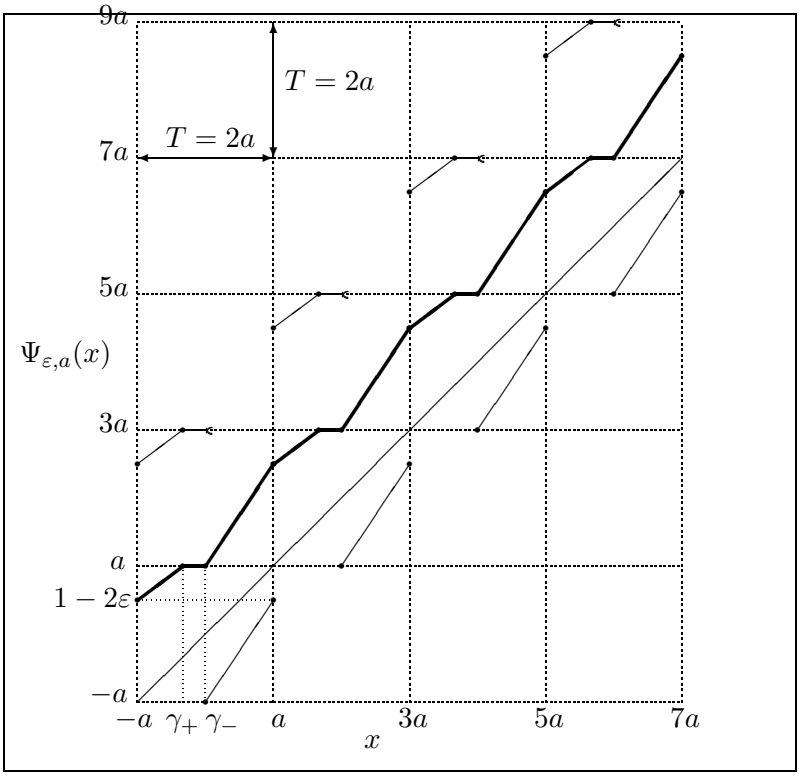

Figure 4.17: Lift of the auxiliary map.

such that $\Psi(x) \ge x$. Since Φ is non-decreasing and continuous in $(-a, \gamma_-)$ and in (γ_-, a), and because $\Phi(-a) = \Phi(a)$ and $\lim_{x\uparrow\gamma_-} \Phi(x) = 2a + \Phi(\gamma_-) = 2a + \lim_{x\downarrow\gamma_-} \Phi(x)$ (see figure 4.11), the function Ψ is continuous, non-decreasing and has the following periodic property (see figure 4.17):

$$\Psi(x + T) = \Psi(x) + T, \tag{4.28}$$

where we defined $T \equiv 2a$ to be the spatial period of the lift Ψ. Any iterate Ψ^n of the auxiliary map will be of the same type as Ψ, that is, continuous, non-decreasing and with the same periodic property (4.28). For simplicity, in this section, we will let $x_n = \Psi^n(x)$.

In order to define the rotation number, we first consider the following limit

$$\rho_0(\varepsilon, a) = \lim_{n\to\infty} \frac{x_n}{n\,T}. \tag{4.29}$$

Then the *rotation number* of the auxiliary map is defined as

$$\rho(\varepsilon, a) = \rho_0(\varepsilon, a) - \lfloor \rho_0(\varepsilon, a) \rfloor, \tag{4.30}$$

that is, the integer part of ρ_0. Consequently, ρ and ρ_0 differ by an integer. The rotation number gives the average rotation of an orbit through Φ. This is equivalent to the relative number of times that the orbit touches the upper branch of Φ. Therefore, from (4.23), $v(\varepsilon, a) = \rho(\varepsilon, a)$. From now on we will use interchangeably $v(\varepsilon, a)$ and $\rho(\varepsilon, a)$.

First of all let us prove that $v(\varepsilon, a)$ is a function, in other words, that for any $0 \leq \varepsilon \leq 1$ and a such that $\gamma(\varepsilon, a) > 0$ the velocity of the travelling wave front is well-defined. This problem is the same that the existence of the rotation number for a circle map and it has already been proved [52, 54] for a monotone increasing map. In our case the auxiliary map is non-decreasing —it has intervals where it is constant— but the same line of proof may be followed:

Theorem 4.3.1 *The limit* (4.29) *exists and is independent of* $x = x_0$. *Consequently the rotation number* $\rho(\varepsilon, a)$ *also exists and is independent of* $x = x_0$.

Proof. First suppose that ρ_0 exists for some x^*. Then there exists an integer m such that

$$\begin{aligned} & m\,T \leq x - x^* < (m+1)\,T \\ \Rightarrow\ & x^* + m\,T \leq x < x^* + (m+1)\,T, \end{aligned}$$

and because Ψ^n is non-decreasing

$$\begin{aligned} & \Psi^n(x^* + m\,T) \leq \Psi^n(x) \leq \Psi^n(x^* + (m+1)\,T) \\ \Rightarrow\ & x_n^* + m\,T \leq x_n \leq x_n^* + (m+1)\,T \\ \Rightarrow\ & \frac{m}{n} \leq \frac{x_n - x_n^*}{n\,T} \leq \frac{(m+1)}{n}. \end{aligned}$$

Taking the limit $n \to \infty$ and recalling that m and T are fixed, we have that

$$\lim_{n\to\infty} \frac{x_n - x_n^*}{n\,T} = 0$$

and therefore if ρ_0 exists for x^*, it exists for any x and it is the same number.

Finally, we prove that ρ_0 exists for at least one point x^*. We consider two cases: (a) when a power of Φ has a fixed point and (b) when it does not.

(a) Suppose that x^* is a fixed point of Φ^m, *i.e.* we have for the lift,

$$x_m^* = x + r\,T,$$

for some integer r. By induction, any multiple iteration of $\Psi^m(x)$, $(\Psi^m)^n(x)$, has the property

$$x_{nm}^* = x + nr\,T.$$

Every integer k can be written as $k = nm + s$, where n, s are integers and $0 \leq s < m$. Thus

$$x_k^* = x_{nm+s}^* = \Psi^s(x_{nm}^*) = \Psi^s(x^* + nr\,T) = \Psi^s(x^*) + nr\,T = x_s^* + nr\,T,$$

and then

$$\frac{x_k^*}{k\,T} = \frac{x_s^*}{k\,T} + \frac{nr}{k}.$$

Since m is fixed and $s < m$, $x_s^*/k\,T \to 0$ as $k \to \infty$, and

$$\lim_{k\to\infty} \frac{x_k^*}{k\,T} = \lim_{n\to\infty} \frac{nr}{nm+s} = \frac{r}{m}.$$

Hence ρ_0 exists for $x^* = \Phi^m(x^*)$, and is the rational number r/m.

(b) We show that if no power of Φ has a fixed point, then ρ_0 still exists. Saying that no power of Φ has a fixed point means that no integers m and r exist such that

$$x_m = x + r\,T.$$

Thus for any m there exists an integer r such that

$$x + r\,T < x_m < x + (r+1)\,T \tag{4.31}$$

independently from the choice of x. If we apply repetitively Ψ^m to (4.31) we obtain the sequence of inequalities

$$\begin{aligned}
x + r\,T &< x_m < x + (r+1)\,T \\
x_m + r\,T &\leq x_{2m} \leq x_m + (r+1)\,T \\
x_{2m} + r\,T &\leq x_{3m} \leq x_{2m} + (r+1)\,T \\
&\vdots \qquad\qquad \vdots \\
x_{(n-1)m} + r\,T &\leq x_{nm} \leq x_{(n-1)m} + (r+1)\,T,
\end{aligned} \tag{4.32}$$

which added up together lead to

$$x + nr\,T < x_{nm} < x + n(r+1)\,T. \tag{4.33}$$

If we combine the first inequality of (4.32) with (4.33), with $x = x^* = 0$ we obtain

$$\left| \frac{x_{nm}^*}{nm\,T} - \frac{x_m^*}{m\,T} \right| < \frac{1}{m}. \tag{4.34}$$

Interchanging m and n in (4.34) and adding in to (4.34) again, we obtain

$$\left| \frac{x_n^*}{n\,T} - \frac{x_m^*}{m\,T} \right| < \frac{1}{n} + \frac{1}{m},$$

showing that the sequence $\{x_n^*/n\,T\}$ is a Cauchy sequence, which converges in $\mathbb{R}$. Therefore, when no power of Φ has a fixed point, the rotation number still exists for $x^* = 0$ and then it exists and is the same for all x. □

Moreover, following the same proofs than in [52, 54] but taking into account that Ψ is not strictly increasing, it is possible to show that

Theorem 4.3.2 *The rotation number $\rho(\varepsilon, a)$ is irrational if and only if Φ has no periodic points.*

Now that the existence of the rotation number —the velocity of the travelling interface— has been established, we can proceed to prove its continuity.

4.3.2 Continuity of the travelling velocity

We show that the velocity $v(\varepsilon, a)$ of a minimal 1-state of $F_{\varepsilon,a}$ depends continuously on the parameters ε and a.

Theorem 4.3.3 *The limit* (4.29) *depends continuously on the parameters a and ε and so does the rotation number $\rho(\varepsilon, a)$.*

Proof. Let us consider two pairs of parameter values (ε, a) and (ε', a') of the auxiliary map Φ such that $\max(|\varepsilon' - \varepsilon|, |a' - a|) < \delta$, and choose m sufficiently large such that $2/m < \epsilon_0$ for any $\epsilon_0 > 0$. It is important to notice that the dummy variable ϵ_0 used in this proof is not related to the coupling parameter ε ($\epsilon_0 \neq \varepsilon$). We define $\Psi_{\varepsilon,a}$ and $\Psi_{\varepsilon',a'}$ the corresponding lifts of $\Phi_{\varepsilon,a}$ and $\Phi_{\varepsilon',a'}$. It is possible to find an integer r such that

$$x^* + (r-1)\,T < \Psi^m_{\varepsilon,a}(x^*) < x^* + (r+1)\,T, \tag{4.35}$$

and choosing δ small enough we can make $\Psi_{\varepsilon',a'}$ to satisfy the same inequality, since Ψ depends continuously on the parameters a and ε:

$$x^* + (r-1)\,T < \Psi^m_{\varepsilon',a'}(x^*) < x^* + (r+1)\,T. \tag{4.36}$$

Applying repetitively $\Psi^m_{\varepsilon,a}$ and $\Psi^m_{\varepsilon',a'}$ to (4.35) and (4.36) respectively and adding the resulting series of inequalities as in the previous proof leads to

$$\begin{aligned} x^* + n(r-1)\,T < \Psi^{nm}_{\varepsilon,a}(x^*) < x^* + n(r+1)\,T \\ x^* + n(r-1)\,T < \Psi^{nm}_{\varepsilon',a'}(x^*) < x^* + n(r+1)\,T, \end{aligned}$$

which implies that

$$\left| \frac{\Psi^{nm}_{\varepsilon,a}(x^*)}{nm\,T} - \frac{\Psi^{nm}_{\varepsilon',a'}(x^*)}{nm\,T} \right| < \frac{2}{m} < \epsilon_0$$

for any n. By taking m large enough it is possible to find that for any ϵ_1, $\epsilon_2 > 0$, one could approximate the rotation numbers by:

$$\begin{aligned} \left| \frac{\Psi^{nm}_{\varepsilon,a}(x^*)}{nm\,T} - \rho_0(\varepsilon, a) \right| &< \epsilon_1, \\ \left| \frac{\Psi^{nm}_{\varepsilon',a'}(x^*)}{nm\,T} - \rho_0(\varepsilon', a') \right| &< \epsilon_2. \end{aligned}$$

Therefore, by adding the last three inequalities together, one arrives to the following bound for the difference of the rotation numbers

$$|\rho_0(\varepsilon, a) - \rho_0(\varepsilon', a')| < \epsilon, \tag{4.37}$$

where we defined $\epsilon = \epsilon_0 + \epsilon_1 + \epsilon_2$, whose value could be made as small as required by choosing m large enough. Hence, for any $\epsilon > 0$, there exists $\delta > 0$ such that (4.37) is satisfied, and the continuity of $\rho_0(\varepsilon, a)$ w.r.t. the parameters ε and a follows. □

In summary, the velocity $v(\varepsilon, a)$ of the travelling front exists, is continuous with respect to the parameters ε and a and it is independent from the choice of the initial minimal 1-state, *i.e.* $v(\varepsilon, a)$ is independent from the choice of $-1 \leq x_0 \leq 1$ of $[x_0, i]$ as initial configuration for $F_{\varepsilon,a}$.

4.3.3 The travelling velocity is non-decreasing

We have proved in Theorem 2.2.1 that the velocity of the travelling interface is a non-decreasing function of the coupling parameter. We give here another proof for a decreasing step state.

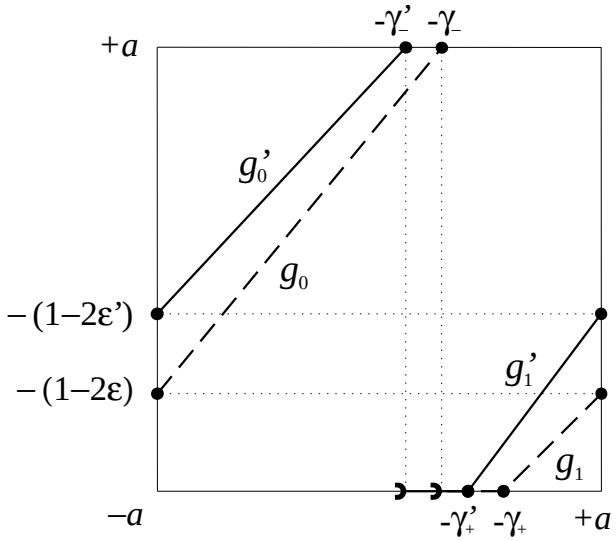

Figure 4.18: If $\varepsilon' > \varepsilon$ then $-\gamma'_+ < -\gamma_+$, $-\gamma'_- < -\gamma_-$, $g'_0 \geq g_0$ and $g'_1 \geq g_1$, thus, the auxiliary maps corresponding to ε' ($\Upsilon_{\varepsilon',a}(x)$, solid lines) and to ε ($\Upsilon_{\varepsilon,a}(x)$, dashed lines) satisfy $\Upsilon_{\varepsilon',a}(x) \geq \Upsilon_{\varepsilon,a}(x)$.

Theorem 4.3.4 *The rotation number $\rho(\varepsilon, a)$ is a non-decreasing function of ε.*

Proof. Let us consider two coupling parameter values, ε and ε', such that $\varepsilon' > \varepsilon$ and consider their respective auxiliary maps, $\Upsilon_{\varepsilon,a}$ and $\Upsilon_{\varepsilon',a}$. It is easy to verify that

$$\varepsilon < \varepsilon' \quad \Rightarrow \quad \begin{cases} -\gamma'_+ < -\gamma_+ \quad \text{and} \quad -\gamma'_- < -\gamma_- \\ g'_0(x) \geq g_0(x) \quad \text{and} \quad g'_1(x) \geq g_1(x) \quad \text{in} \quad U \times U, \end{cases}$$

and thus $\Upsilon_{\varepsilon',a}(x) \geq \Upsilon_{\varepsilon,a}(x)$, see figure 4.18. The same inequality then holds for the corresponding lifts and therefore, from the definition of rotation number, it is straightforward to show that $\rho(\varepsilon', a) \geq \rho(\varepsilon, a)$. □

4.3.4 The velocity tree

Here we address the problem of finding an algorithm providing the velocity for a given value of the parameters (ε, a). This algorithm is characterized in terms of a velocity tree where, depending on the values of ε and a, we follow a determined path. We begin with a pure step state of the form $X_0 = (\ldots, -1, -1, 1, 1, \ldots)$. In order to simplify the notation we recall that this step state may only evolve to the right with the one-way CML (0.6), so we may rewrite $X_0 = (-1, 1, \ldots)$, since the homogeneous part to the left of the interface remains unchanged. After one iteration we have $X_1 = (-1, 1 - 2\varepsilon, 1, \ldots)$, which for the symbolic dynamics representation reads $X_1 = (-1, f_0(a), 1, \ldots)$. In the following we will drop the

argument of $f_{S(x_0)}(x_0)$ and write only $f_{S(x_0)}$ when there is no ambiguity. Thus X_1 is written as $X_1 = (-1, f_0, 1, \ldots)$, the following iterations may be chosen from (4.7). There are in total 4 different choices (cf. (4.7)), but one of them is impossible when the gap size is positive.

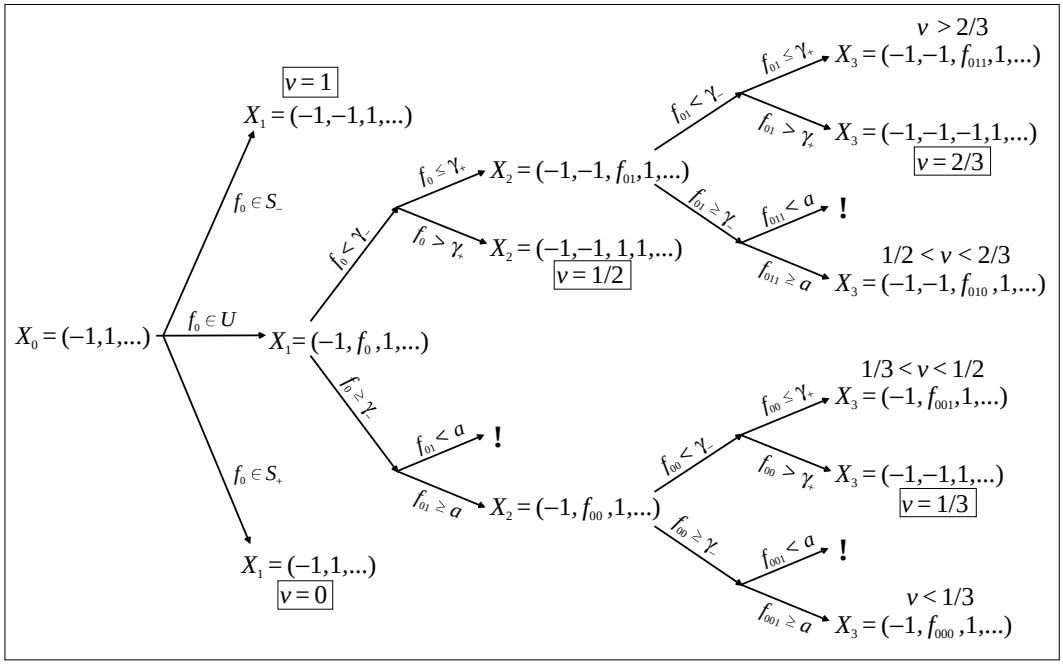

Figure 4.19: Velocity tree

The choices may be represented in a velocity tree, (figure 4.19), where each branch correspond to a different choice. Every branch has a condition to be satisfied for the initial state X_0 to evolve there. A branch terminating with an exclamation mark denotes an inadmissible choice since the gap size is positive and thus two sites are not simultaneously allowed in the interface. It is important to mention that, in order to arrive to a particular branch, we have to pass through a path of branches dictated by the symbolic sequence of the particular chosen orbit. Taking an upper (lower) branch in the tree corresponds to a '1' ('0') in the sequence; thus large velocities correspond to upper paths in the tree and vice-versa.

The overall parametric condition to be satisfied for a given velocity, is obtained by all the individual conditions of the corresponding path. We work out such conditions in some simple cases. For $v = 1$ the only condition to be satisfied is $f_0 \in S_-$, that is $-1 \leq f_0(a) \leq -a \quad \Rightarrow \quad -1 \leq 1 - 2\varepsilon \leq -a$, thus $\varepsilon \leq 1$ and $\varepsilon \geq \frac{1+a}{2} = 1 - \varepsilon_c$. The area corresponding to $v = 1$ is plotted in figure 4.20 (left shaded area). For $v = 0$ the condition is $f_0 \in S_+$ that amounts to $\varepsilon \geq 0$ and $\varepsilon \leq \frac{1-a}{2} = \varepsilon_c$ and it is also plotted in figure 4.20 (right shaded area). The zone where $v = 0$ corresponds to the solution of (4.15) giving the bounds on the extent of the non-propagating case (Theorem 2.2.3). Finally, for $v = 1/2$ the conditions are $f_0 \in U$, $f_0 < \gamma_-$ and $f_0 > \gamma_+$ whose solution is shown in figure 4.20 as the central shaded area.

Using this procedure it is possible to determine the regions where a given rational velocity $v = p/q$ is present. Nevertheless, the tree representation does not tell if such regions are non-empty. In the next section we show that such regions, for the positive gap, are non-empty and we give a simpler way of computing them.

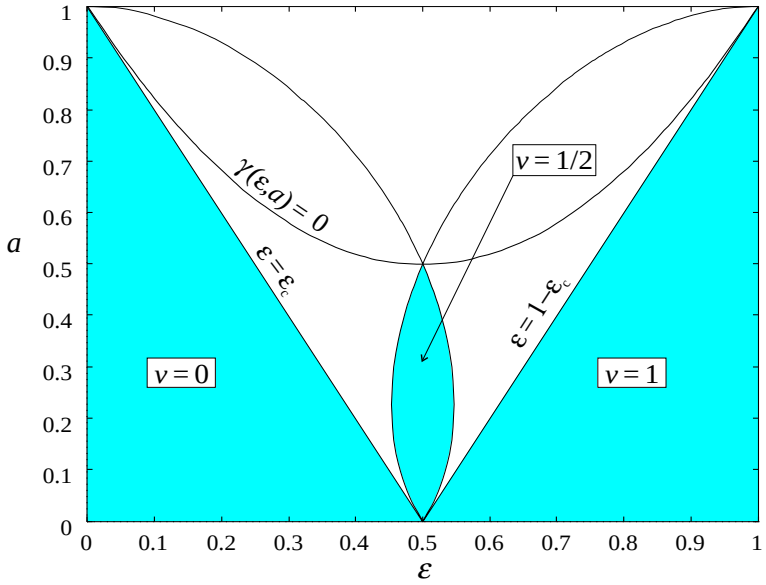

Figure 4.20: Parameter space regions where $v = 0, 1, 1/2$. The left (right) shaded area correspond to the (ε, a)-values where $v = 0$ ($v = 1$) and the central shaded area corresponds to $v = 1/2$.

4.4 Mode-locking of the auxiliary map

In this section we focus our attention on the dynamics of the auxiliary map $\Phi_{\varepsilon,a}$ and we show that there exists a mode-locking (ε, a)-region for every rational rotation number. It is important to say that the results of the following section rely on the parametric stability of periodic gap orbits (orbits that fall in the gap Γ). The study of non gap orbits will be dealt in section 4.4.2 and we show how they do not contribute towards the mode-locking since they all are unstable. Therefore we are firstly interested in the mode-locking of periodic gap orbits.

4.4.1 Mode-locking

Using the auxiliary map as a representation of the interface of the travelling front, we now prove that the gap Γ forces the velocity to be locked to rational values if $\Phi_{\varepsilon,a}$ has a periodic orbit containing a point of Γ. This gives an easier way, when compared with the one provided by the velocity tree, for computing the mode-locking regions in the (ε, a) plane.

The symbolic coding of the orbit of the auxiliary map $\Phi_{\varepsilon,a}$ gives the velocity of the travelling interface via equation (4.23). The presence of a non-negative gap Γ induces a mode-locking of the rotation number in the following way. Since the rotation number, *i.e.* the velocity of the travelling interface, does not depend on the choice of the initial interfacial site (Theorem 4.3.1), let us take as initial condition the step state $X_0 = [x_0, i]_0$ with x_0 in Γ. The dynamics on the auxiliary map gives then the orbit generated from an arbitrary point x_0 in Γ. Suppose that for the parameter values (ε, a) we have that after q iterations the orbit falls into Γ. The orbit is then periodic of period q with rotation number p/q, p being the number of times the orbit visits the upper branch of Φ. In figure 4.21 we show an example of a periodic orbit of period 5, starting with an x_0 in Γ, corresponding to a rotation number

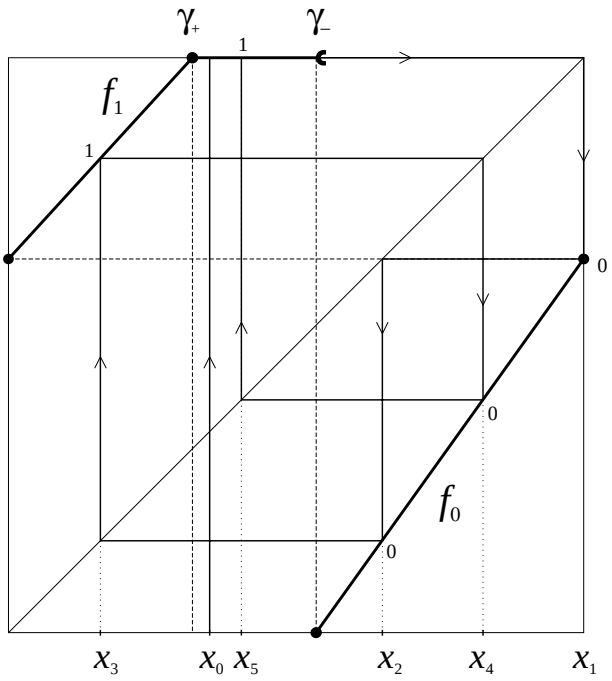

Figure 4.21: Period 5 orbit of the auxiliary map for $(\varepsilon, a) = (0.44, 0.4)$, the coding sequence for this orbit is $S(x_0) = \overline{(0,0,1,0,1)}$ and corresponds to a rotation number $v = 2/5$.

$v = 2/5$.

Suppose now that we introduce a small perturbation of the parameters and the initial condition: $(x_0, \varepsilon, a) \longrightarrow (x_0', \varepsilon', a')$. The perturbed orbit $x_t' = \Phi^t_{\varepsilon', a'}(x_0')$ is initially at a distance $\Delta x_0 = x_0' - x_0$ from the unperturbed one. The continuity of the lift of Φ (Theorem 4.3.3) ensures that x_t' depends continuously on the parameters ε, a and the initial condition. The distance Δx_t between the two orbits at time t can be made as small as we want by making (x_0, ε, a) sufficiently close to (x_0', ε', a'). Because Γ is an open interval, if x_q belongs to Γ, then so does x_q' for a sufficiently small perturbation (figure 4.22). Therefore we have established the crucial result:

Theorem 4.4.1 *If the gap orbit of $\Phi_{\varepsilon,a}$ is finite (periodic), then it is stable under a sufficiently small perturbation of parameters and initial condition.*

Thus there is a region in the parameter space (ε, a), where the given rotation number is constant or *mode-locked*. An example of mode-locking ε-regions for a fixed value of a is given in figure 4.23. The mode-locked region, corresponding to a given rotation number $\rho = p/q$, can be computed by noting that in order that an orbit, starting at any x_0 in Γ, falls, after q iterations, in Γ we must have that $\Phi^q_{\varepsilon,a}(\Gamma) \subseteq \Gamma$. This condition may be rewritten as $\Phi^{q-1}_{\varepsilon,a}(a) \in \Gamma$ giving the inequalities

$$\gamma_+ \quad \leq \quad \Phi^{q-1}_{\varepsilon,a}(a) \quad \leq \quad \gamma_-, \tag{4.38}$$

since

$$\forall\, x_0 \in \Gamma \quad \Longrightarrow \quad x_1 = \Phi_{\varepsilon,a}(x_0) = a.$$

We shall mention that the end points of (4.38) are included because an orbit arriving at $\gamma_\pm$ after $q-1$ iterations will also reach $1-2\varepsilon$ in two more iterations: $\Phi^2_{\varepsilon,a}(\gamma_-) = \Phi_{\varepsilon,a}(-a) = 1-2\varepsilon$

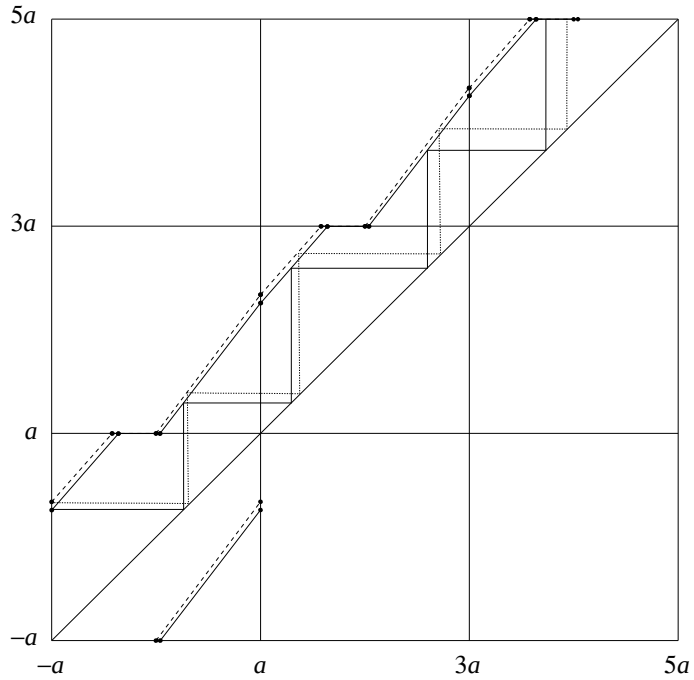

Figure 4.22: Parametric stability of a gap orbit. The solid and the dashed lines correspond to two nearby values of ε. The corresponding gap orbits have the same symbolic sequence and fall into the gap in the same number of iterations.

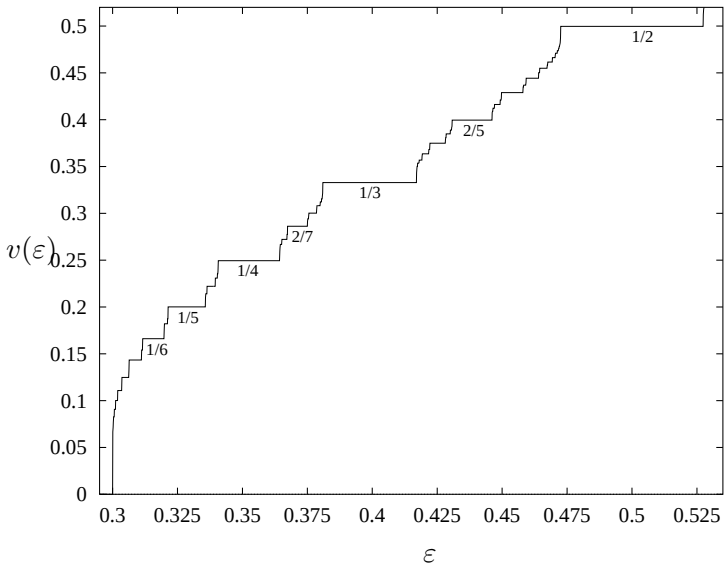

Figure 4.23: Velocity of the travelling interface for $a = 2/5$. The mode-locked regions correspond to gap orbits that are stable to parametric perturbations. The period of the gap orbit is given the denominator of the rational velocity $v = p/q$, some of the velocity plateaus are indicated.

and $\Phi^2_{\varepsilon,a}(\gamma_+) = \Phi_{\varepsilon,a}(+a) = 1 - 2\varepsilon$ (cf. (4.9)) —these two orbits correspond to the kneading sequences of the local map [55, 56]. The closed ε-interval, for a constant value of a, given by the inequality (4.38), for which the velocity is mode-locked to a given rational, is called a *plateau*.

Equation (4.38) ensures that the orbit starting at $x_0 \in \Gamma$ falls again into the gap after q iterations and therefore repeats itself every q iterations. The value of $\Phi^q_{\varepsilon,a}(x_0)$ is determined by the coding sequence of the associated rotation number. So if we want to compute the mode-locked region for a given velocity $v = p/q$ we have to determine the (ε, a) region where (4.38) is satisfied in correspondence to the code $S(p/q)$ given by (4.25). For example, to compute the mode-locked region for the velocity $v = 2/5$ we first compute $S(2/5) = (\overline{0,0,1,0,1})$, and so we know that the orbit visits the regions U_-, U_-, U_+, U_- and Γ (see figure 4.21). If fact, all the gap orbits starting at $x_0 \in \Gamma$ finish in the gap after q iterations and therefore the last digit of $S(v = p/q)$ is a '1'. This detail is very important: the last digit of any sequence $S(v = p/q)$ does not represent an iteration of f_1 in the auxiliary map, but it indicates that the orbit has fallen into the gap. Applying the last digit '1' (f_1), to both sides of (4.38) we replace the latter with

$$f_1(\gamma_+) \quad \leq \quad \Phi^q_{\varepsilon,a}(a) \quad \leq \quad f_1(\gamma_-), \tag{4.39}$$

The advantage of the inequality (4.39) is that we can now use directly the coding sequence by applying f_0 (f_1) every time a '0' ('1') is encountered in $S(v = p/q)$ without having to pay attention if the last digit comes from the gap and not from f_1.

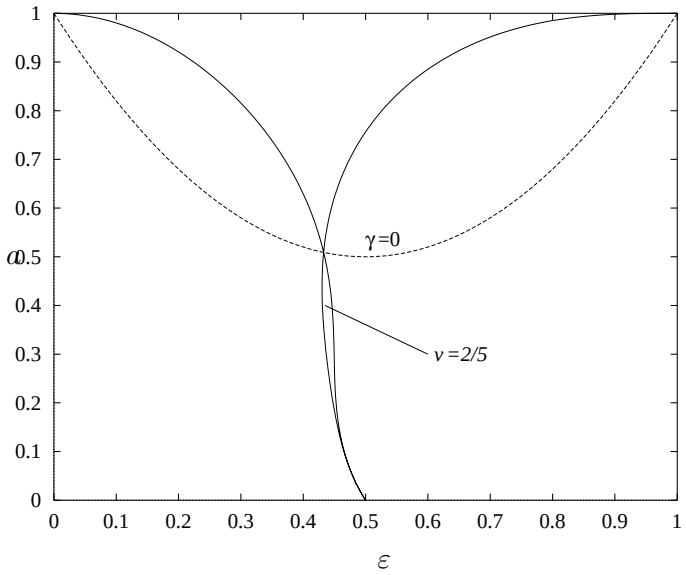

Figure 4.24: Mode-locking region for $v = 2/5$ obtained by solving the inequalities 4.39.

We illustrate this method to compute the mode-locking region for $v = 2/5$. The coding sequence for $v = 2/5$ is $S(2/5) = (\overline{0,0,1,0,1})$ (see figure 4.21) and thus we have to compute $\Phi^5_{\varepsilon,a}(a)$ with $f_1\left(f_0\left(f_1\left(f_0\left(f_0(a)\right)\right)\right)\right)$. The mode-locking region for $v = 2/5$ is then given by

$$f_1(\gamma_+) \quad \leq \quad f_1\left(f_0\left(f_1\left(f_0\left(f_0(a)\right)\right)\right)\right) \quad \leq \quad f_1(\gamma_-),$$

and is plotted in the (ε, a)-plane in figure 4.24.

The same procedure may be followed to obtain the zones where a given $v = p/q$ is present. In figure 4.25 we depict some of this zones corresponding to the principal mode-locking ratios.

These regions, represented as shaded areas, are the so-called *Arnold's tongues* [57, 58]. It can be observed that as we approach the zero-gap line (dashed line) —given by $\gamma = 0$ in (4.10)— the tongue size decreases, as the latter is related to the gap size.

We have shown several examples and given the general formula for finding the mode-locking regions (inequality (4.39)). The next result show that these regions have positive measure.

Theorem 4.4.2 *The (ε, a) region where any given rational velocity $0 < v = p/q < 1$ has positive measure.*

Proof. Since $v(\varepsilon = 0) = 0$ and $v(\varepsilon = 1) = 1$, using the continuity of $v(\varepsilon)$ (cf. Theorem 4.3.3), it is possible to find at least one point ε^* such that for any given rational velocity p/q we have that $v(\varepsilon^*) = p/q$. Thus there exist a periodic orbit of Φ with the periodic symbolic sequence $S(p/q)$. On the other hand, Theorem 4.3.1 also tells us that the rotation number does not depend on the initial condition, thus we could take as the initial condition a point in the gap Γ giving us a periodic gap orbit. From Theorem 4.4.1, such periodic gap orbits are stable to sufficiently small parametric perturbations if the gap size is positive and therefore the set of (ε, a)-values where this is true has positive measure. □

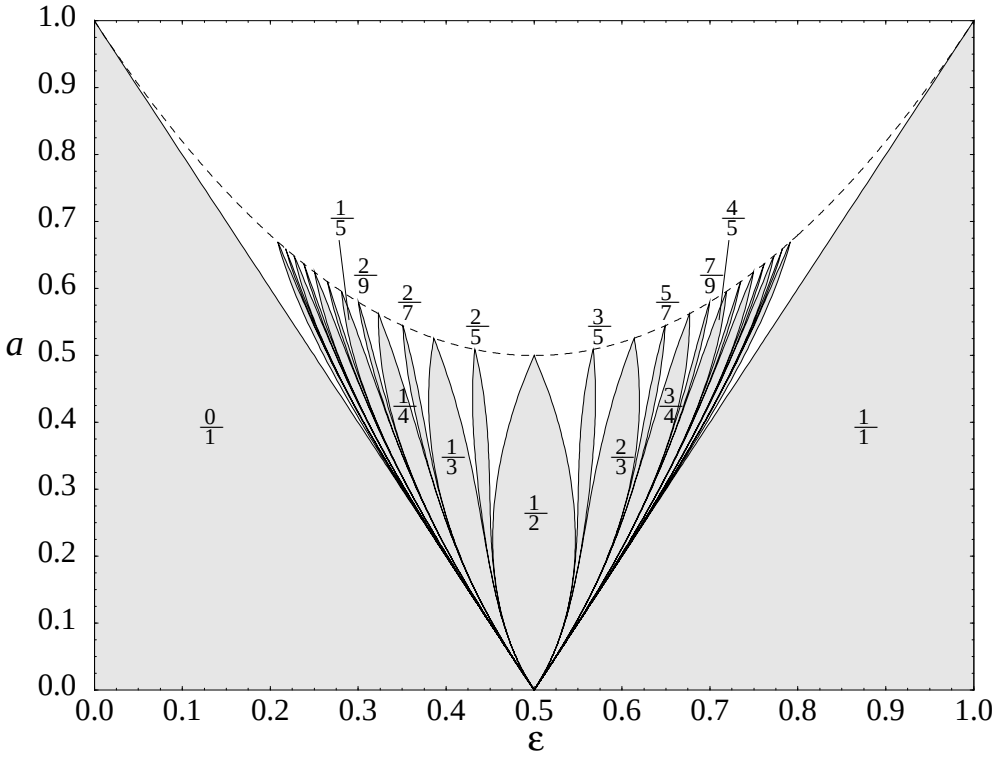

Figure 4.25: Arnold's tongues in the (ε, a)-plane corresponding to the zones where rational velocities of the travelling interface of $F_{\varepsilon,a}$ are present.

The above theorem tells that there always exists a non-empty ε-interval, for a fixed a, where the velocity is mode-locked to any given rational velocity. Such a function is called a *Devil's staircase* [58, 59]. This mode-locking phenomenon is very similar to the one observed for a uniform rotation in a perturbed circle map [57]. The fractal nature of $v(\varepsilon)$ will be revealed in more detail in section 4.5.4.

4.4.2 Linear stability of periodic non gap orbits

In the previous section we dealt with the parametric stability of periodic gap orbits which is responsible for the mode-locking phenomenon. In this section we study the linear stability of periodic non gap orbits —orbits that never touch the gap Γ— and we prove that they do not contribute towards the mode-locking tongues because they are all contained in a unstable zone.

Let us construct periodic non gap orbits first. A periodic orbit $x(t)$, with velocity $v = p/q$, that never touches the gap has p 1's and $(q-p)$ 0's in its symbolic sequence. None of its symbols comes from the gap and therefore every 1 (0) corresponds to a f_1 (f_0). Thus, the multiplier $\lambda(p,q)$ giving the linear stability of a periodic non gap orbit with velocity $v = p/q$ is given by

$$\lambda(p,q) = \prod_{i=1}^{q} \Phi(x(i)) = (f_1')^p \, (f_0')^{q-p} = \left(\frac{\varepsilon}{a}\right)^p \left(\frac{1-\varepsilon}{a}\right)^{q-p}.$$

For the periodic orbit $x(t)$ to be unstable we need its multiplier to be larger than 1, that is

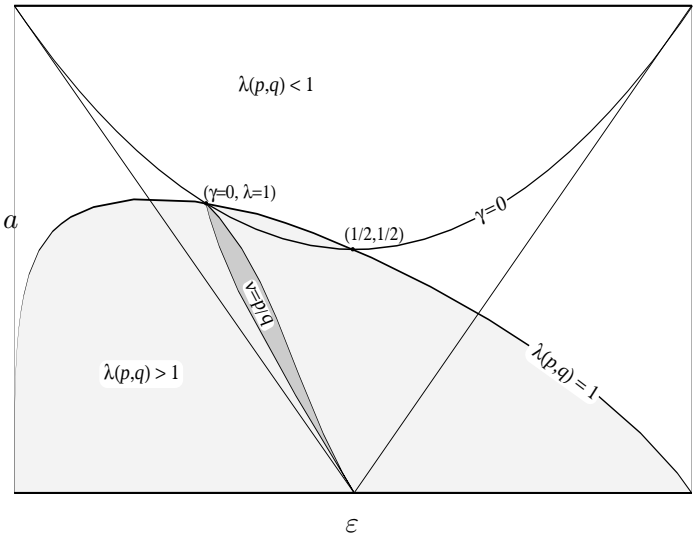

Figure 4.26: Schematic representation of the unstable region (light shaded area) for a periodic non gap orbit with velocity $v = p/q$. The whole p/q-mode-locking tongue corresponding to a periodic gap orbit is inside the unstable region.

$$\begin{aligned} \lambda(p,q) > 1 \quad &\Rightarrow \quad \left(\frac{\varepsilon}{a}\right)^p \left(\frac{1-\varepsilon}{a}\right)^{q-p} < 1 \\ &\Rightarrow \quad a < \varepsilon^{\frac{p}{q}} (1-\varepsilon)^{\frac{q-p}{q}} \\ &\Rightarrow \quad a < \varepsilon^v (1-\varepsilon)^{1-v}. \end{aligned} \tag{4.40}$$

For a given velocity $v = p/q$ the inequality (4.40) gives the (ε, a) region where a particular periodic non gap orbit is unstable. Such regions seem to contain the whole p/q-tongue obtained in the previous section for the gap orbits (see figure 4.26 and figure 4.27). On the other hand, the monotonicity of $v(\varepsilon, a)$ w.r.t ε (cf. section 4.3.3) ensures that the mode-locking tongues cannot possess two disjoint regions. Thus there is strong numerical evidence showing that no stable periodic non gap orbit exists and therefore the analysis of the previous

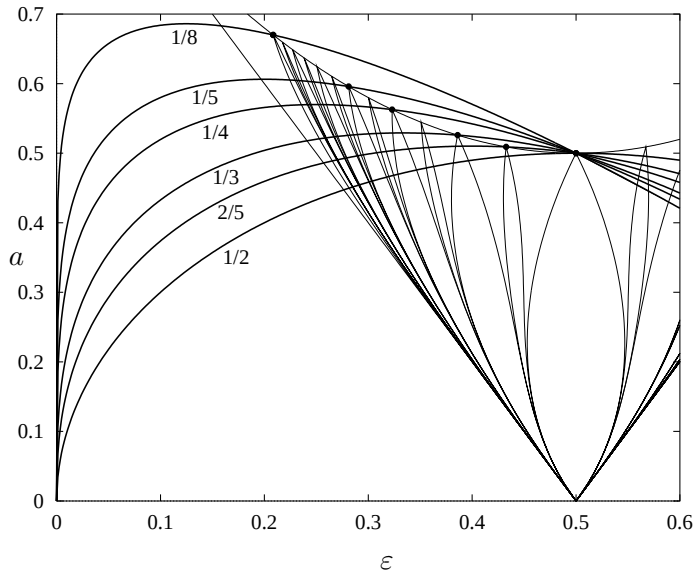

Figure 4.27: Several examples of the unstable regions for periodic non gap orbits. The tongues always fall inside the corresponding unstable region.

section, using gap orbits, is sufficient for describing the mode-locking in the non-negative gap region.

4.4.3 Stability diagram of the auxiliary map

An interesting feature of the auxiliary map is its stability diagram. Theorem 4.4.2 states that for a fixed value of a there is a non-empty ε-interval where any given rational rotation number $v(\varepsilon, a) = p/q$ is present. Thus, varying continuously ε for a given value of a gives a Devil's staircase featuring ε-mode-locked intervals. The dynamics of the auxiliary map at each mode-locked interval is that of a periodic orbit. For the mode-locking ε-interval corresponding to the rational rotation number $v(\varepsilon, a) = p/q$ the period of the orbit through Φ is exactly q. As we vary ε we browse through all the possible periods for the orbit. Therefore bifurcations should occur changing the stability of the periodic points of Φ as well as introducing (or removing) other periodic points.

Let us first recall the value of the fixed point of the interface for the extreme cases $v(\varepsilon, a) = 0$ ($\varepsilon \leq \varepsilon_c$) and $v(\varepsilon, a) = 1$ ($\varepsilon \geq 1 - \varepsilon_c$). It is important to recall that these cases are not accounted for by the auxiliary map, since the latter is only defined when $\varepsilon_c < \varepsilon < 1 - \varepsilon_c$. In the proof of Theorem 4.2.2 we showed how the dynamics of the interface site tends to x_- (x_+) when $\varepsilon \leq \varepsilon_c$ ($\varepsilon \geq 1 - \varepsilon_c$) where x_- (x_+) is the fixed point of f_0 (f_1). Therefore the value of the interface site x_t is

$$x_t = \begin{cases} x_- = \dfrac{a\varepsilon}{1 - \varepsilon - a} & \text{if} \quad \varepsilon \leq \varepsilon_c \\ \\ x_+ = \dfrac{a(1-\varepsilon)}{a - \varepsilon} & \text{if} \quad \varepsilon \geq 1 - \varepsilon_c, \end{cases}$$

whose period is one —corresponding to the denominator of the velocity $v = 0/1$ and $v = 1/1$.

Let us now concentrate our attention on to the non-trivial region $\varepsilon_c < \varepsilon < 1 - \varepsilon_c$. It is possible to find analytically the periodic orbits of Φ via standard methods, but we present here only the numerical results. It is worth mentioning that the periodic gap orbits of Φ are superstable, because the map in the gap has zero derivative. In figure 4.28 we depict the stable points of Φ for $a = 0.25$ and $a = 0.5$. Figure 4.28.a presents several bifurcation points. The principal mode-locking ratios ($v = 1/q$ and $v = 2/q$, some of them are indicated in the figure) embrace almost all the ε interval making this bifurcation diagram look quite simple. However, we have to keep in mind that when all periods are accounted for, this diagram is really a fractal one. This feature may be better observed in figure 4.28.b where we show a similar bifurcation diagram but now with $a = 0.5$. In figure 4.28.b the multiple bifurcations near $\varepsilon = 0.5$ are more visible since we are taking a path in the (ε, a)-parameter space where the tongues are much narrower than in the path used in figure 4.28.a, see figure 4.29.

In order to have a clearer picture of the bifurcation diagram, we recall that the size of the mode-locked regions is directly related to the size of the gap. Thus, avoiding a path that cuts some tongues in narrow regions and some others in thick regions, and taking a path with constant gap leads to a better comparative size between plateaus. Figure 4.30 depicts the bifurcation diagram for a gap size of 0.1 (see figure 4.29 for a picture of this path). The bifurcations are now more evident, since the gap size is quite small ($\gamma = 0.1$), and the self-similar structure is quite striking, as we may observe a blow-up of figure 4.30.a in 4.30.b. This fractal structure will be revealed in more detail by means of envelopes using Farey series and unimodular transformations in section 4.5.4.

Because of symmetry we only plotted half ($\varepsilon \leq 1/2$) of the bifurcation diagrams in figures 4.28 and 4.30. Replacing ε by $1 - \varepsilon$ and vice-versa in the definition of the auxiliary map,

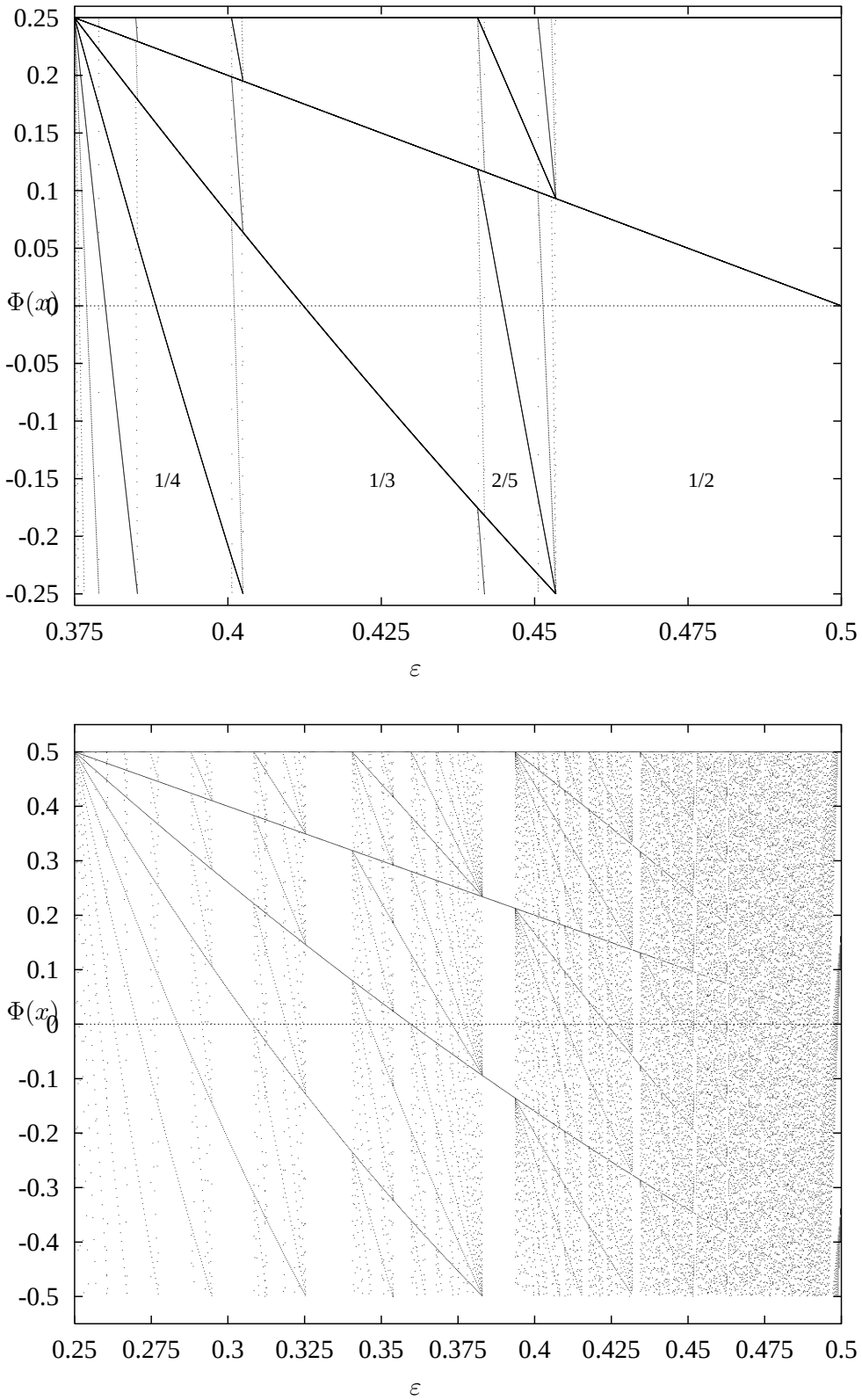

Figure 4.28: Bifurcation diagram of the stable points of the auxiliary map. (a) $a = 0.25$ and (b) $a = 0.5$ plotting 100 points after 10 000 transitory iterations.

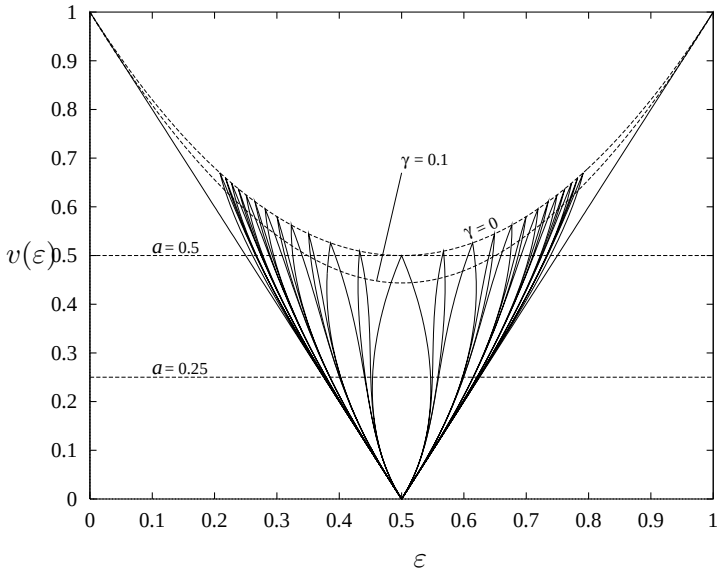

Figure 4.29: Paths in the (ε, a)-parameter space used for the bifurcation diagrams in figures 4.28 and 4.30.

equation (4.18), leads to

$$\Phi'_{\varepsilon,a}(x) = \begin{cases} f'_1(x) & \text{if } -a \le x \le -\gamma_- \\ a & \text{if } -\gamma_- < x < -\gamma_+ \\ f'_0(x) & \text{if } -\gamma_+ \le x \le a \end{cases}$$

with

$$f'_0(x) \equiv \frac{\varepsilon}{a}\, x - (1-\varepsilon)$$

$$f'_1(x) \equiv \frac{1-\varepsilon}{a}\, x + \varepsilon.$$

With the exception of the gap, Φ' and Φ are symmetric w.r.t. the origin O (figure 4.31). For Φ' and Φ to be completely symmetric, the gap of Φ' should be placed at $-a$ and not at a. However, the iterates of $-a$ and a, by any of the auxiliary maps, give the same result: $\Phi(\pm a) = 1 - 2\varepsilon$ and $\Phi'(\pm a) = -(1-2\varepsilon)$. So, for the purpose of the bifurcation diagram, it does not really matter if the gap is at a or $-a$. Thus, we could use the symmetric w.r.t. O of Φ instead of Φ'. Therefore the bifurcation diagram inherit a symmetry w.r.t the point $(\varepsilon, v(\varepsilon)) = (1/2, 1/2)$ allowing us to restrict the study to ε-values smaller than $1/2$.

4.4.4 Velocity in the zero-gap case

In this section we give an analytical expression for the velocity $v(\varepsilon, a)$ for the zero-gap case. As it may be noticed from figure 4.25 the thickness of the tongues seems to tend to zero as we approach the zero-gap curve ($\gamma = 0$). In fact, we shall demonstrate that the width of the tongues in the zero-gap case is zero. The reason is that the auxiliary map, for the zero-gap case, only consists of the two linear parts f_1 and f_0, with no gap Γ, see figure 4.11.b, and therefore the lack of mode-locking.

The orbit of the auxiliary map is $f_{S_0}(x_0)$, where the sequence $S_0 = S(x_0)$ gives the order in which the maps f_0 and f_1 have to be applied. However, in the zero gap case, this order

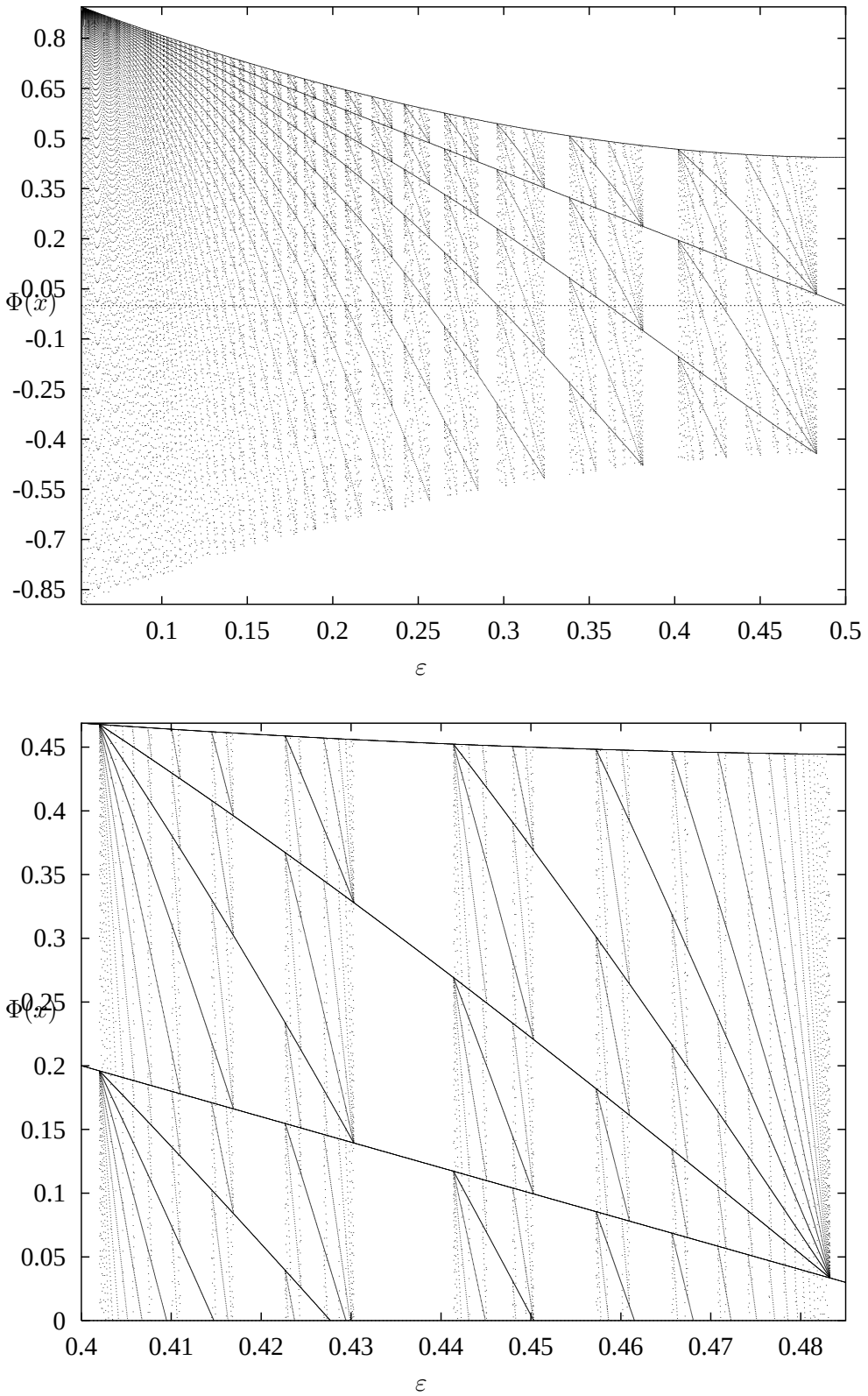

Figure 4.30: Bifurcation diagram of the stable points of the auxiliary map with $\gamma = 0.1$ plotting 100 points after 10 000 transitory iterations. Figure (b) is a blow-up of a figure (a) showing the self-similarity structure.

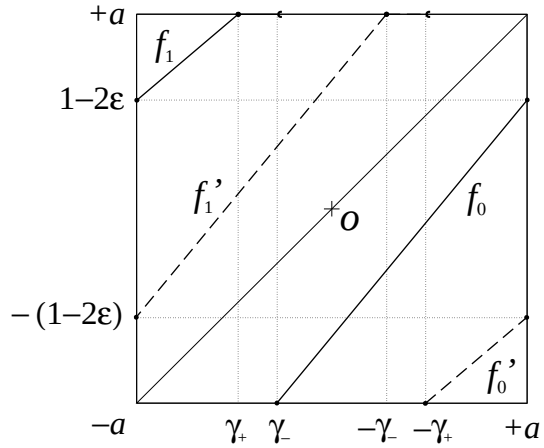

Figure 4.31: The auxiliary map $\Phi'_{\varepsilon,a}$ is obtained by replacing ε by $1-\varepsilon$ and vice-versa in the original auxiliary map Φ. With the exception of the gap, Φ' and Φ are symmetric w.r.t. the origin O.

is not important since $f_0(f_1(x)) = f_1(f_0(x)) \Leftrightarrow \gamma = 0$ as easily verified (see Lemma 4.5.5). Let us suppose that the (ε, a)-parameter values are such that $\gamma = 0$ and that $v(\varepsilon, a) = m/n$. Thus f_1 is applied m times in f_{S_0} and f_0 is applied $n-m$ times. The n-th iterate is then

$$\begin{aligned} f_{S_0}(x_0) &= f_1^m \left(f_0^{n-m}(x_0) \right) \\ &= f_1^m \left(\left(\frac{1-\varepsilon}{a} \right)^{n-m} (x_0 - x_-) + x_- \right) \\ &= \left(\frac{\varepsilon}{a}\right)^m \left[\left(\left(\frac{1-\varepsilon}{a} \right)^{n-m} (x_0 - x_-) + x_- \right) - x_+ \right] + x_+ \\ &= \left(\frac{\varepsilon}{a}\right)^m \left(\frac{1-\varepsilon}{a} \right)^{n-m} (x_0 - x_\pm) + x_\pm, \end{aligned}$$

where x_- and x_+ are, respectively, the fixed points of f_0 and f_1 (cf. (4.14)) which coincide ($x_\pm = x_- = x_+$) when $\gamma = 0$. Since we are dealing with the rational velocity m/n, the orbit $\Phi^n(x_0)$ must return to its initial value, *i.e.*

$$\left(\frac{\varepsilon}{a}\right)^m \left(\frac{1-\varepsilon}{a} \right)^{n-m} (x_0 - x_\pm) + x_\pm = x_0$$

therefore

$$\left(\frac{\varepsilon}{a}\right)^m \left(\frac{1-\varepsilon}{a} \right)^{n-m} = 1. \tag{4.41}$$

Equation (4.41) has been obtained for a rational velocity m/n. To find the analytical form of $v(\varepsilon, a)$ one has to extend, by continuity, to irrational values of the velocity. Let us then assume that the velocity $v(\varepsilon, a) = r$ is an arbitrary real number in the interval $[0, 1]$. Since any irrational $v(\varepsilon, a) = r$ may be approximated, as close as desired, by a rational m/n, it is possible to write $m \simeq rn$ and thus, in the limit equation (4.41) reads

$$\begin{aligned} \left(\frac{\varepsilon}{a}\right)^{rn} \left(\frac{1-\varepsilon}{a} \right)^{n(1-r)} = 1 \quad &\Rightarrow \quad \left(\frac{\varepsilon}{1-\varepsilon} \right)^r = \frac{a}{1-\varepsilon} \\ &\Rightarrow \quad v(\varepsilon) = r = \frac{\ln\left(\dfrac{1-2\varepsilon(1-\varepsilon)}{1-\varepsilon} \right)}{\ln\left(\dfrac{\varepsilon}{1-\varepsilon} \right)}, \end{aligned} \tag{4.42}$$

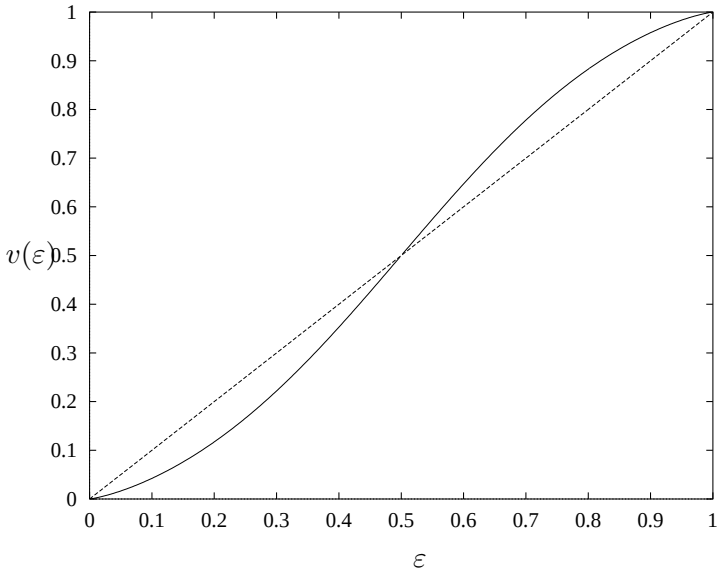

Figure 4.32: Velocity curve for the zero-gap case. Here the velocity is an analytical function and does not present mode-locking.

where we replaced a by $1-2\varepsilon(1-\varepsilon)$ (zero-gap condition) obtaining a function of ε. The plot of $v(\varepsilon)$ for the zero gap is presented in figure 4.32 and it completes the study of the dynamics for the zero-gap case.

4.5 Representing the velocity tree with an integral lattice

In this section we give a useful geometric representation of the velocity tree using an integral lattice. This new representation allows us to calculate in a straightforward manner the sequence associated with the Farey sum of two given velocities with known associated sequences. This lattice representation for rational numbers has been known for centuries and it has been used before in the context of rotation numbers (cf. [51, 60]).

4.5.1 The integral lattice

We are going to identify the rational velocities with points in the integral lattice $\mathbb{Z}^2$. We first introduce the Farey numbers. The Farey series [61, 62] of order r, $\mathcal{F}_r$, is defined to be the set of irreducible fractions, in ascending order, belonging to $[0,1]$ whose denominators are smaller than or equal to r (figure 4.33). If m/n and m'/n' are two consecutive rationals of the Farey series $\mathcal{F}_{\max(n,n')}$ then $|m'n - n'm| = 1$. This unimodular property is very important and will be used later (section 4.5.4). With it is possible to represent the Farey series as a tree: first take the rationals $0/1$ and $1/1$ —they satisfy the unimodular property, $|1\times 1 - 1\times 0| = 1$— and add to the tree their mediant. The mediant of two rationals p/q and p'/q', denoted by $\frac{p}{q}\oplus\frac{p'}{q'}$ is obtain by adding their respective numerators and denominators, *i.e.* $\frac{p}{q}\oplus\frac{p'}{q'} = \frac{p+p'}{q+q'}$. Thus the mediant of $0/1$ and $1/1$ is $\frac{0}{1}\oplus\frac{1}{1} = 1/2$. The whole Farey tree is then constructed by repeatedly inserting the mediants of every two consecutive Farey numbers, see figure 4.33. It

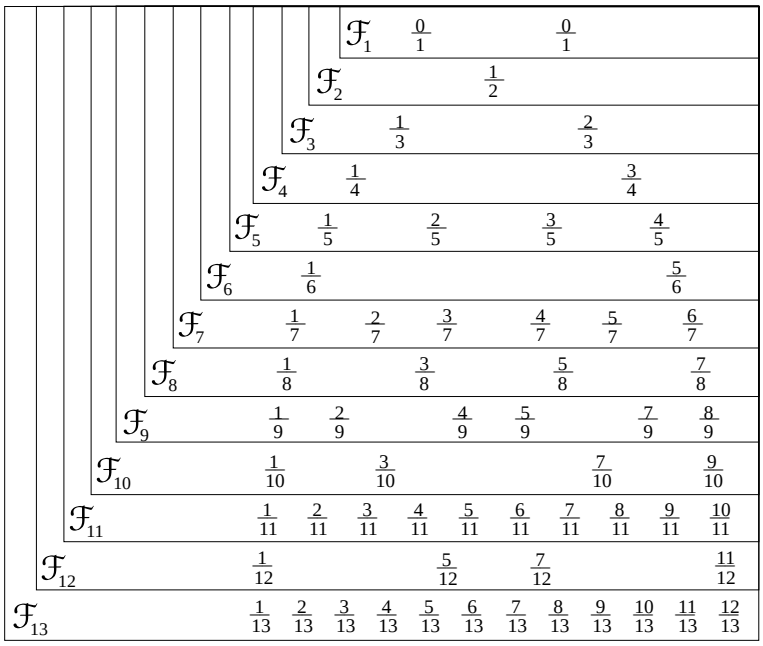

Figure 4.33: Construction of the Farey numbers using the Farey tree. In between any two consecutive Farey numbers of the same order we include their mediant. Note that $\mathcal{F}_r \subset \mathcal{F}_{r+1}$.

is possible to show that any two consecutive Farey numbers satisfy the unimodular property [61].

We want to identify the elements of the Farey series with points on the integral lattice $\mathbb{Z}^2$. To do so we associate to every Farey number m/n the point $P(m/n) = (n-m, m)$. It is obvious that distinct Farey numbers correspond to distinct points in $\mathbb{Z}^2$. Let us take O as the origin of the lattice, and consider the ray $OP(m/n)$ emanating from the origin and passing through $P(m/n)$. Defining $\theta(m/n)$ to be the angle between $OP(m/n)$ and the X-axis, *i.e.* $\theta(m/n) = \tan^{-1}(m/(n-m))$, it can be shown that distinct Farey numbers correspond to distinct angles θ.

Lemma 4.5.1 $m/n < m'/n' \Leftrightarrow \theta(m/n) < \theta(m'/n')$.

Proof. $m/n < m'/n' \Leftrightarrow n/m > n'/m' \Leftrightarrow n/m-1 > n'/m'-1 \Leftrightarrow (n-m)/m > (n'-m')/m' \Leftrightarrow m/(n-m) < m'/(n'-m') \Leftrightarrow \tan(\theta(m/n)) < \tan(\theta(m'/n')) \Leftrightarrow \theta(m/n) < \theta(m'/n')$. □

In section 4.2.3 we showed that $S(m/n) = \tau(Spec(m/n))$. Consider now the spectrum of m/n, $Spec(m/n) = s_1 s_2 \ldots s_m$ with $s_i \equiv \lfloor im/n \rfloor$. We have

Lemma 4.5.2 *The sequences* $\{s_i/i\}_{i=1,2,\ldots,n}$ *and* $\{(s_i+1)/i\}_{i=1,2,\ldots,n}$ *give, respectively, the series of lower and upper approximants of order* i *to* $v = m/n$.

Proof. $s_i = \lfloor im/n \rfloor \Rightarrow s_i \leq im/n < s_{i+1} \Rightarrow s_i/i \leq m/n < (s_i+1)/i$. Therefore s_i/i and $(s_i+1)/i$ give, respectively, the lower and upper approximants of order i of m/n. □

We know (section 4.2.3) that a '0' in $S(m/n)$ means one iteration of the CML without advance of the interface, and a '1' in $S(m/n)$ means that the interface has advanced one

site after one iteration of the CML. Let us now illustrate the effect of moving vertically and horizontally from adjacent points on the lattice $\mathbb{Z}^2$. Moving horizontally to the right on $\mathbb{Z}^2$ has the effect $(n-m,m) \longmapsto (n+1-m,m)$, *i.e.* from $P(m/n)$ to $P(m/(n+1))$. This corresponds to a single iterate of the lattice without any advance of the interface. Moving vertically upwards has the effect $(n-m,m) \longmapsto (n-m,(m+1)) = ((n+1)-(m+1),m+1)$, *i.e.* from $P(m/n)$ to $P((m+1)/(n+1))$ which corresponds to a shift of one site of the interface after one iteration. Therefore we may identify a '0' with an horizontal vertex joining two adjacent points and a '1' with a vertical vertex joining adjacent points. Hence taking a path of right-horizontal and upward-vertical vertices in $\mathbb{Z}^2$ from the origin to the point $P(m/n)$ will give us a possible coding sequence for the velocity $v = m/n$, since we have to take m upward-vertical vertices (m '1"s) and $n-m$ right-horizontal vertices ($n-m$ '0"s) in order to arrive to $P(m/n) = (n-m,m)$.

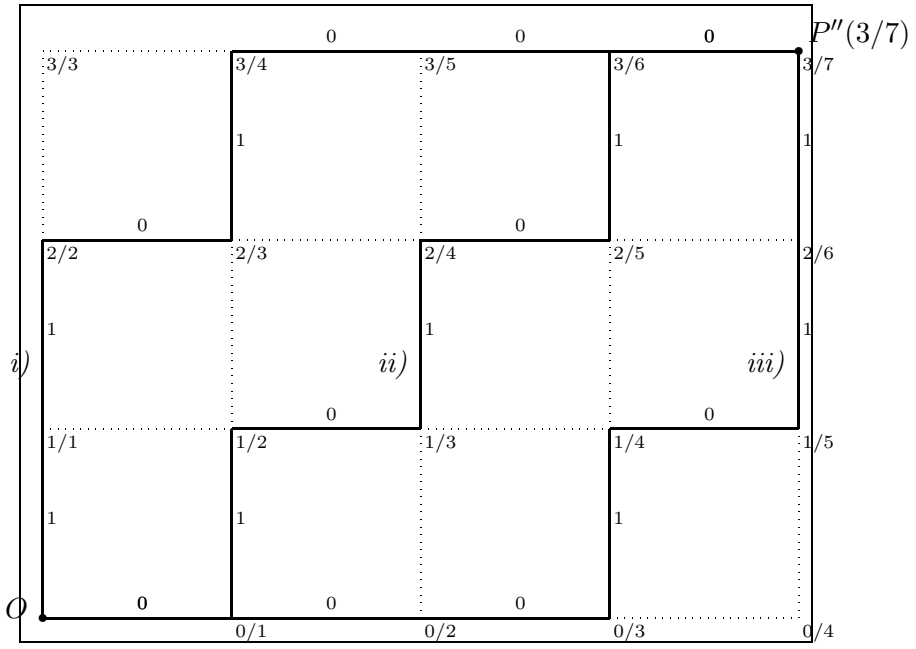

Figure 4.34: There exists many different possible paths in the integral lattice joining the origin and a given point $P(m/n)$ corresponding to different symbolic sequences. In this example between the possible symbolic sequences for $P(3/7)$ are: *i)* $P(3/7) = (1,1,0,1,0,0,0)$, *ii)* $P(3/7) = (0,1,0,1,0,1,0)$ and *iii)* $P(3/7) = (0,0,0,1,0,1,1)$.

But the problem of selecting the right path on the lattice arises: there are several paths that can be taken in $\mathbb{Z}^2$ in order to arrive to a desired velocity $v = m/n$ (see figure 4.34) corresponding to all the possible permutations of $n-m$ '0"s and m '1"s.

Lemma 4.5.3 *The path in $\mathbb{Z}^2$ giving the coding sequence of $v = m/n$ is obtained by taking the nearest vertices to $OP(m/n)$ contained in the lower semi-plane defined by it.*

Proof. The lower approximants of order i to $v = m/n$ are given by s_i/i (Lemma 4.5.2): they are contained in the lower semi-plane defined by the line $OP(m/n)$ since they are smaller than $v = m/n$ (Lemma 4.5.1), and they are to be as close as possible to the line $OP(m/n)$ because they give the closest rational to $v = m/n$ with denominator equal to i. □

In figure 4.35 the correct path of the velocity $v = 3/7$ is depicted using the above tech-

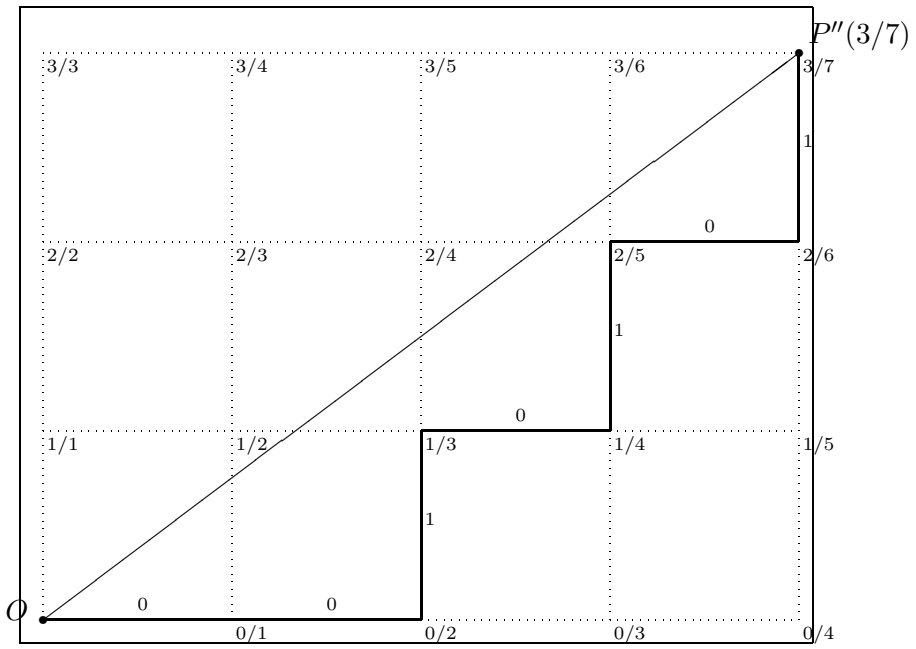

Figure 4.35: The correct path in the integral lattice giving the coding sequence for $v = m/n$ may be found by choosing the closest path in $\mathbb{Z}^2$ that is under the line $OP(m/n)$. In this example the method gives us $P(3/7) = (0, 0, 1, 0, 1, 0, 1)$.

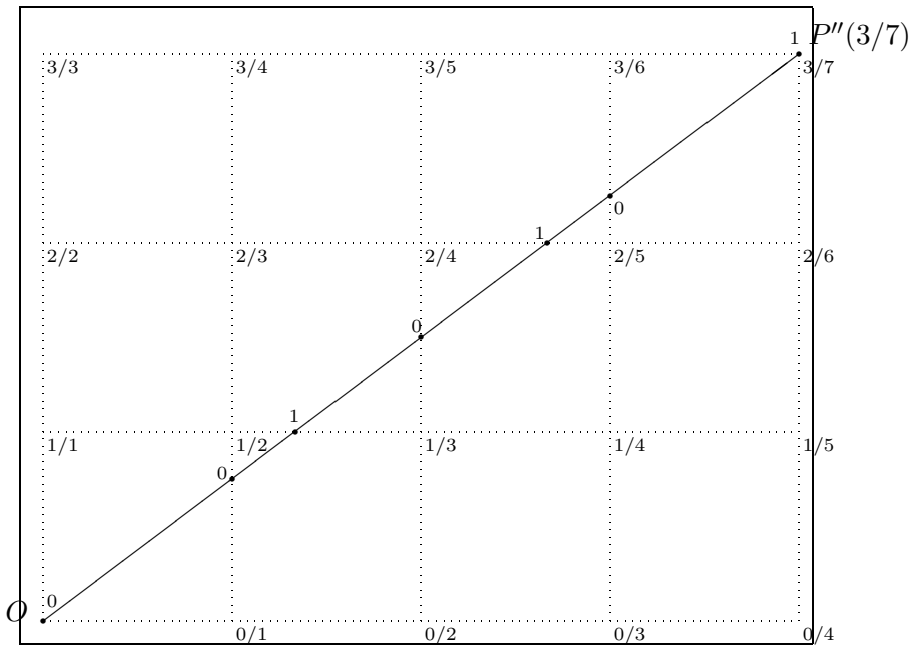

Figure 4.36: Another method giving the correct path in the integral lattice of the coding sequence $P(3/7) = (0, 0, 1, 0, 1, 0, 1)$, this time we use the intersections with the lattice.

nique. Another simple geometrical construction is to associate a symbol to every cross between the segment $[OP(m/n)]$: beginning with a symbol '0' from the origin, associate a '1' every time $[OP(m/n)]$ crosses an horizontal vertex of the lattice and associate a '0' when it crosses a vertical one. The resulting sequence, taking first the '0' of the origin and ordering the crosses by taking first the ones closer to the origin, is equivalent to the coding sequence of $v = m/n$. This follows from an argument similar to that used in Lemma 4.5.3. This construction is illustrated in figure 4.36 for the same velocity $v = 3/7$.

4.5.2 Concatenating sequences using the lattice representation

We wish to relate the sequences of $S(m/n)$ and $S(m'/n')$ with the sequence $S((m+m')/(n+n'))$ of the mediant. We first define the concatenation of two sequences $S(m/n) = (\overline{s_1, \ldots, s_p})$ and $S(m'/n') = (\overline{s'_1, \ldots, s'_q})$, denoted by $S(m/n)S(m'/n')$, as the concatenation of their respective periods:

$$S\left(\frac{m}{n}\right) S\left(\frac{m'}{n'}\right) = (\overline{s_1, \ldots, s_p, s'_1, \ldots, s'_q}).$$

The following result then follows.

Lemma 4.5.4 *If $m/n < m'/n'$ are two consecutive Farey numbers, then the sequence $S((m+m')/(n+n'))$ associated to their mediant is the concatenation of $S(m/n)$ and $S(m'/n')$. That is*

$$S\left(\frac{m+m'}{n+n'}\right) = S\left(\frac{m}{n}\right) S\left(\frac{m'}{n'}\right) = (\overline{s_1, \ldots, s_p, s'_1, \ldots, s'_q}). \tag{4.43}$$

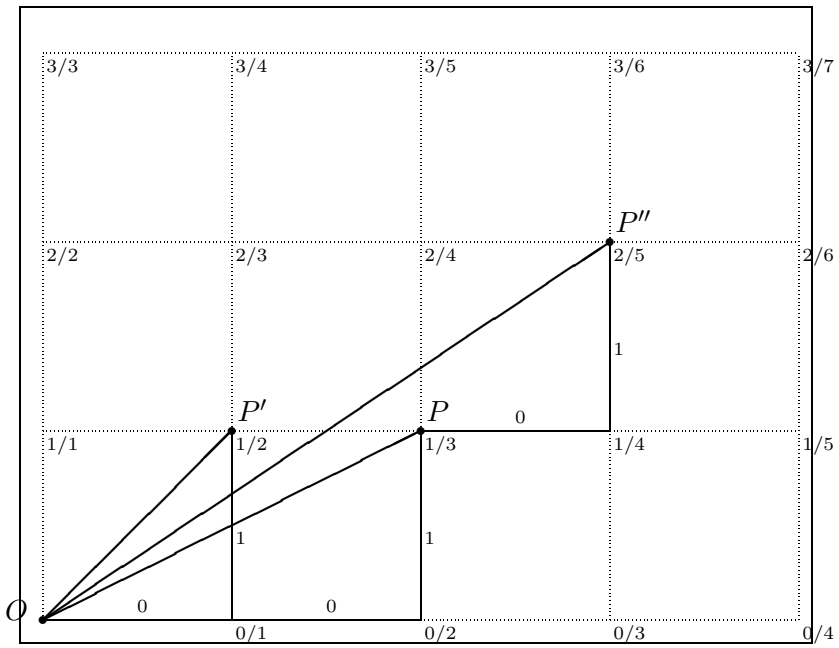

Figure 4.37: The symbolic sequence for the mediant, $v'' = 2/5$, of the two velocities $v = 1/3$ and $v' = 1/2$ is obtained by vector-like adding their path of their symbolic sequences.

Proof. Let us define $P'' \equiv P((m+m')/(n+n'))$, $P' \equiv P(m'/n')$ and $P \equiv P(m/n)$. The coordinates of these points are $P'' = (n+n'-(m+m'), m+m')$, $P' = (n'-m', m')$ and

$P' = (n-m, m)$, and therefore $\overrightarrow{OP'} = \overrightarrow{PP''}$ (figure 4.37). Let T be the triangle $T = OPP'$. Because m/n and m'/n' are consecutive Farey numbers of $\mathfrak{F}_{\max(n,n')}$ there is no fraction p/q such that $m/n < p/q < m'/n'$ with $q \leq \max(n, n')$. Therefore there are no points of $\mathbb{Z}^2$ contained in the triangle T. Analogously the same happens on the triangle $T' = OPP''$ where there are no points of $\mathbb{Z}^2$ inside it. Because there are no lattice points inside T, the closest path to the line OP'' from O to P'' is the same as the path taken from O to P, hence the first part of the sequence $S((m+m')/(n+n'))$ is the sequence $S(m/n)$. On the other hand, since $\overrightarrow{OP'} = \overrightarrow{PP''}$, a possible path for arriving from P to P'' is the path from O to P', *i.e.* the path associated with the sequence $S(m'/n')$, but translated by $\overrightarrow{OP}$ and since there are no points in T' this path is the closest to the line OP''. Therefore the last part of the sequence $S((m+m')/(n+n'))$ is given by the sequence $S(m'/n')$. □

An example of this construction is shown in figure 4.37 where the velocities $v = 1/3$ and $v' = 1/2$ give the mediant $v'' = 2/5$. The associated sequence of $v = 1/3$ is $S(1/3) = (0, 0, 1)$ (horizontal+horizontal+vertical), the one for $v' = 1/2$ is $S(1/2) = (0, 1)$ (horizontal+vertical) and the one for the mediant $v'' = 2/5$ is $S(2/5) = (0, 0, 1, 0, 1)$ which corresponds to the concatenation of $S(1/3)$ and $S(1/2)$.

Two questions arise from the above method: (a) is the concatenated sequence periodic? If yes, what is the period. And (b) is the order of concatenation important? The following result answers both questions.

Lemma 4.5.5

(a) The concatenation of two periodic sequences gives again a periodic sequence whose period is the sum of their periods.

(b) The maps f_0 and f_1 commute if and only if the gap size is zero.

Proof (a). The concatenation of the sequences $S = (\overline{s_1, \ldots, s_p})$ and $S' = (\overline{s'_1, \ldots, s'_q})$ of respective periods p and q gives, by definition, the periodic sequence $SS' = (\overline{s_1, \ldots, s_p, s'_1, \ldots, s'_q})$ whose period is clearly $p + q$.

Proof (b). Recall that the semi-infinite symbolic sequence gives the order in which we have to apply f_0 and f_1. The functions f_0 and f_1 does not commute in general. Requiring $f_0(f_1(x)) = f_1(f_0(x))$ for any x is equivalent to

$$\begin{aligned}
& \tfrac{1-\varepsilon}{a}\left(\tfrac{\varepsilon}{a}\,x + (1-\varepsilon)\right) - \varepsilon = \tfrac{\varepsilon}{a}\left(\tfrac{1-\varepsilon}{a}\,x - \varepsilon\right) + (1-\varepsilon) \\
\Leftrightarrow \quad & \tfrac{1-\varepsilon}{a}(1-\varepsilon) - \varepsilon = -\tfrac{\varepsilon}{a}\varepsilon + (1-\varepsilon) \\
\Leftrightarrow \quad & a = \varepsilon^2 + (1-\varepsilon)^2 = 1 - 2\varepsilon(1-\varepsilon) \\
\Leftrightarrow \quad & \gamma = 0,
\end{aligned}$$

where we imposed $a \neq 0$. The case $a = 0$ is trivial since the $\varepsilon = \varepsilon_c = 1/2$ and the velocity curve is a step function centered at $\varepsilon = 1/2$. Therefore, the functions f_0 and f_1 commute if and only if the gap size is zero. □

The second part of this lemma shows that periodic orbits for zero gap size could be found without taking into account the order in which the maps f_0 and f_1 are applied —this fact

was already used in section 4.4.4 in order to find an explicit expression for the travelling front velocity, as a function of the parameters ε and a, in the zero gap case.

On the other hand, the symmetry of $v(\varepsilon)$ w.r.t. the point (1/2,1/2) has already been established in (2.24). Now let us see how this property reflects itself into the symbolic sequence representation. The general formula for the i-th symbolic symbol for a velocity $v = p/q$ may be written as (cf. (4.25))

$$S(p/q)_i = \lfloor ip/q \rfloor - \lfloor (i-1)p/q \rfloor,$$

where $i = 1, \ldots, q$ and $S(p/q)_i$ stands for the i-th symbol of $S(p/q)$. First notice that $S(p/q)_1 = 0$ and $S(p/q)_q = 1$ for any irreducible fraction $0 < p/q < 1$. The following two results are directly related with the symmetric property (2.24).

Property 4.5.6 *Consider* $0 < v = p/q < 1$, *then*

(a) $S(1-p/q)_{q-j+1} = 1 - S(p/q)_j \quad \forall\, j = 1, \ldots, q$

(b) $S(1-p/q)_j = 1 - S(p/q)_j \quad \forall\, j = 2, \ldots, q-1.$

Proof (a).

$$\begin{aligned} S(1-p/q)_{q-j+1} &= \lfloor (q-j+1)(1-p/q) \rfloor - \lfloor (q-j+1-1)(1-p/q) \rfloor \\ &= q - j + 1 + \lfloor (-q+j-1)p/q \rfloor - (q-j) - \lfloor (j-q)p/q \rfloor \\ &= 1 + (-1 + \lfloor (j-1)p/q \rfloor) - (-1 + \lfloor jp/q \rfloor) \\ &= 1 - (\lfloor jp/q \rfloor - \lfloor (j-1)p/q \rfloor) \\ &= 1 - S(p/q)_j. \end{aligned}$$

Proof (b).

$$\begin{aligned} S(1-p/q)_j &= \lfloor j(1-p/q) \rfloor - \lfloor (j-1)(1-p/q) \rfloor \\ &= j + \lfloor -jp/q \rfloor - (j-1) - \lfloor -(j-1)p/q \rfloor, \end{aligned}$$

but if $j \neq 0, 1, q, q+1$ (always true since property 4.5.6.b only requires $j = 2, \ldots, q-1$) then

$$S(1-p/q)_j = 1 - \lfloor jp/q \rfloor - 1 + \lfloor (j-1)p/q + 1 \rfloor$$

since $\lfloor -x \rfloor = -x - 1$ when $x \notin \mathbb{Z}$. Thus

$$\begin{aligned} S(1-p/q)_j &= 1 - (\lfloor jp/q \rfloor - \lfloor (j-1)p/q \rfloor) \\ &= 1 - S(p/q)_j \qquad \forall\, j = 2, \ldots, q. \end{aligned}$$

□

The property 4.5.6.a means that if we have already the coding sequence for $v = p/q$ to be $S(p/q) = (s_1, s_2, \ldots, s_{q-1}, s_q)$ then the coding sequence for its symmetric velocity $1 - p/q$ is $S(1-p/q) = (1-s_q, 1-s_{q-1}, \ldots, 1-s_2, 1-s_1)$, *i.e.* invert the sequence and take its conjugate (replacing 0 by 1 and vice-versa). The property 4.5.6.b says that $S(1-p/q) = (0, 1-s_2, 1-s_3, \ldots, 1-s_{q-2}, 1-s_{q-1}, 1)$, *i.e.* conjugate all the symbols but leave unchanged the first and the last symbols that ought to be '0' and '1' respectively.

As an example of properties 4.5.6.a and 4.5.6.b let us derive the coding sequence of $v = 4/7 = 1 - 3/7$ from the one of $v = 3/7$. In order to apply property 4.5.6.a to the coding

sequence for $v = 3/7$, $S(3/7) = (0010101)$, we have to invert it, *i.e.* (1010100), and then take its conjugate, *i.e.* (0101011). Thus, the first method tells us that $S(1 - 3/7) = S(4/7) = (0101011)$. For property 4.5.6.b we take the conjugate of $S(3/7)$, *i.e.* (1101010), and change the first and last symbols to 0 and 1 respectively, which gives $S(4/7) = (0101011)$. In fact the correct sequence for $v = 4/7$ is $S(4/7) = (0101011)$, the same we obtained via the two methods.

4.5.3 Concatenating a family of sequences

In section 4.5.2 we gave a straightforward algorithm for finding the sequence corresponding to the mediant of two given sequences. By applying this result repeatedly it is possible to compute directly the sequences associated to a given family of mediants. Let us consider the two distinct rational velocities $v_a = m_a/n_a$ and $v_b = m_b/n_b$, with corresponding coding sequences $S_a \equiv S(v_a)$ and $S_b \equiv S(v_b)$, and the family of mediants:

$$S(v_a \to v_b)_n = S\left(\frac{m_a + n\, m_b}{n_a + n\, n_b}\right),$$

where $n = 1, 2, \ldots$. The series $S(v_a \to v_b)_n$ consists of a branch of mediants between v_a and v_b, starting at $v_a = S(v_a \to v_b)_1$ and tending to $v_b = S(v_a \to v_b)_\infty$. Two cases may be considered, $v_a < v_b$ and $v_a > v_b$, since the concatenation of two sequences is not commutative (Lemma 4.5.5, the sequence associated with the smallest velocity goes first in the concatenation). Applying repeatedly the concatenation of Lemma 4.5.4 we obtain for the former case

$$S\left(\frac{m_a + n\, m_b}{n_a + n\, n_b}\right) = S_a \overbrace{S_b \ldots S_b}^{n}$$

and for the latter case

$$S\left(\frac{m_a + n\, m_b}{n_a + n\, n_b}\right) = \overbrace{S_b \ldots S_b}^{n} S_a.$$

We will now use the notation S^n for n concatenations of S and recall that $S_1 S_2$ means the concatenation of the sequences S_1 and S_2, in that order. The two cases may be written as

$$S\left(\frac{m_a + n\, m_b}{n_a + n\, n_b}\right) = \begin{cases} S_a S_b^n & \text{if} \quad v_a < v_b \\ S_b^n S_a & \text{if} \quad v_a > v_b. \end{cases} \tag{4.44}$$

4.5.4 Unimodular transformations and envelopes

The structure of the parameter space of the mapping $F_{\varepsilon,a}$ at the boundary of a tongue can be described analytically by means of *envelopes*. These are functions characterizing the structure of sequences of adjacent tongues. The study of envelopes proceeds in two stages. Firstly we derive upper and lower envelopes for the so-called first order plateaus (*i.e.* $v = 1/n$ and $v = (n-1)/n,\ n = 1, 2, \ldots$). Then with the use of unimodular transformations we find envelopes for any order plateaus.

The *zeroth order plateaus* are defined as the two plateaus given by (4.15) with velocities $\{0/1, 1/1\}$. In order to construct any order of plateaus, the *k-th order plateaus*, we take any

two consecutive elements of the previous order $k-1$ denoted by $v_a = m_a/n_a$ and $v_b = m_b/n_b$ ($v_a < v_b$). Then the next order of plateaus is defined as the following infinite increasing sequence of mediants

$$\left\{\dots, \frac{3m_a+m_b}{3n_a+n_b}, \frac{2m_a+m_b}{2n_a+n_b}, \frac{m_a+m_b}{n_a+n_b}, \frac{m_a+2m_b}{n_a+2n_b}, \frac{m_a+3m_b}{n_a+3n_b}, \dots\right\} \tag{4.45}$$

The first order plateaus are thus given by

$$\left\{\dots, \frac{1}{4}, \frac{1}{3}, \frac{1}{2}, \frac{2}{3}, \frac{3}{4}, \dots\right\}.$$

They form a unique family. On the other hand, between any two consecutive plateaus of a given order there is a new family of plateaus of the next order and so on. This construction is similar to that of the Farey series [61]. In particular, any two consecutive plateaus p/q and p'/q' ($p/q < p'/q'$) of the same order and family are consecutive fractions of a Farey series (*i.e.* $qp' - pq' = 1$).

From the definition of the sequence of plateaus (4.45) and by applying the sequence concatenation for a series of mediants (4.44) it is possible to find the sequences associated to a given family of plateaus

$$\left\{\dots,\, S_a^3 S_b,\, S_a^2 S_b,\, S_a S_b,\, S_a S_b^2,\, S_a S_b^3, \dots\right\},$$

where we used the shorthand notation $S_a = S(m_a/n_a)$ and $S_b = S(m_b/n_b)$. It will be useful to distinguish the left Σ_a and right Σ_b subfamilies of sequences defined by

$$\begin{aligned} \Sigma_a &= \left\{\dots,\, S_a^3 S_b,\, S_a^2 S_b,\, S_a S_b\right\} \\ \Sigma_b &= \left\{S_a S_b,\, S_a S_b^2,\, S_a S_b^3, \dots\right\}. \end{aligned} \tag{4.46}$$

Note that the sequence $S_a S_b$, corresponding to the mediant of v_a and v_b, appears in both families. The elements of the subfamilies Σ_a (Σ_b) tend, to the left (right), to S_a (S_b). Thus the subfamilies Σ_a (Σ_b) correspond to velocities going from the mediant of v_a and v_b to the plateau v_a (v_b).

First we derive the envelopes for Σ_a. The elements of Σ_a are of the form

$$S \in \Sigma_a \quad \Longrightarrow \quad S = S_a^n S_b \qquad n = 1, 2, \dots \tag{4.47}$$

which correspond to the velocities

$$v(S_a^n S_b) = \frac{n\, m_a + m_b}{n\, n_a + n_b} \qquad n = 1, 2, \dots \tag{4.48}$$

We recall that the transformations (4.48) are unimodular since we always deal with consecutive fractions of Farey series.

The sequences S_a and S_b correspond to a particular combination of f_0 and f_1. Since f_0 and f_1 are linear, any such combination will again give a linear function. We denote by f_{S_a} (f_{S_b}), as prescribed by (4.26), the linear function resulting from the combination of f_0 and f_1 specified by the sequence S_a (S_b):

$$\begin{aligned} f_{S_a}(x) &= \alpha_a x + \beta_a \\ f_{S_b}(x) &= \alpha_b x + \beta_b. \end{aligned} \tag{4.49}$$

Composing f_{S_a} and f_{S_a} with itself n times gives

$$\begin{aligned} f^n_{S_a}(x) &= f_{S^n_a}(x) = \alpha^n_a(x-\xi^*_a)+\xi^*_a \\ f^n_{S_b}(x) &= f_{S^n_b}(x) = \alpha^n_b(x-\xi^*_b)+\xi^*_b \end{aligned} \tag{4.50}$$

where $\xi^*_a \equiv \beta_a/(1-\alpha_a)$ and $\xi^*_b \equiv \beta_b/(1-\alpha_b)$ are the fixed points of f_{S_a} and f_{S_b} respectively. Combining (4.49) and (4.50) in (4.47) we obtain the iterates of $x_0 = a$ under $\Phi_{\varepsilon,a}$ for the coding sequences $S^n_a S_b$

$$f_{S^n_a S_b}(x_0) = f_{S_b}\left(f^n_{S_a}(x_0)\right). \tag{4.51}$$

Replacing (4.51) in (4.39) we obtain the mode-locking region for a given series of plateaus

$$f_1(\gamma_+) \quad \leq \quad \alpha_b(\alpha^n_a(x_0-\xi^*_a)+\xi^*_a)+\beta_b \quad \leq \quad f_1(\gamma_-). \tag{4.52}$$

As we mentioned earlier, the plateaus include their endpoints. These are obtained from solving the inequalities (4.52) for the extremes $f_1(\gamma_\pm)$. Therefore, all the end points of a given family of plateaus are given by

$$\alpha_b(\alpha^n_a(x_0-\xi^*_a)+\xi^*_a)+\beta_b = f_1(\gamma_\pm), \tag{4.53}$$

where the positive (negative) sign gives the left (right) endpoints of the plateaus. As we vary $n = 0, 1, \ldots$ in (4.53) we browse all the boundaries of the series of plateaus going from the mediant of v_a and v_b to v_a.

Solving (4.53) for n yields

$$n_\pm(\varepsilon, a) = \frac{1}{\ln \alpha_a}\, \ln \frac{f_1(\gamma_\pm) - \beta_b - \alpha_b \xi^*_a}{\alpha_b(x_0 - \xi^*_a)}.$$

Finally, replacing the value of n in (4.48) by $n_\pm(\varepsilon, a)$ gives the continuous functions

$$v_\pm(\varepsilon, a) = \frac{n_\pm(\varepsilon, a)\, m_a + m_b}{n_\pm(\varepsilon, a)\, n_a + n_b}, \tag{4.54}$$

that passes through all the left (v_+) and right (v_-) boundaries of the plateaus. Therefore, $v_\pm$ gives the upper ($+$) and lower ($-$) envelopes of the series of plateaus (4.48).

Now let us derive the envelopes for Σ_b. Using exactly the same definitions as before we obtain the iterates of x_0 under $\Phi_{\varepsilon,a}$ for the sequences $S = S_a S^n_b$:

$$f_{S_a S^n_b}(x_0) = f_{S^n_b}\left(f_{S_a}(x_0)\right). \tag{4.55}$$

The end points of the plateaus are, in this case,

$$\alpha^n_b(\alpha_a x_0 + \beta_a - \xi^*_b) + \xi^*_b = f_1(\gamma_\pm), \tag{4.56}$$

which gives for the envelopes

$$n_\pm(\varepsilon, a) = \frac{1}{\ln \alpha_b}\, \ln \frac{f_1(\gamma_\pm) - \xi^*_b}{\alpha_a x_0 + \beta_a - \xi^*_b}.$$

with

$$v_\pm(\varepsilon, a) = \frac{m_a + n_\pm(\varepsilon, a)\, m_b}{n_a + n_\pm(\varepsilon, a)\, n_b}, \tag{4.57}$$

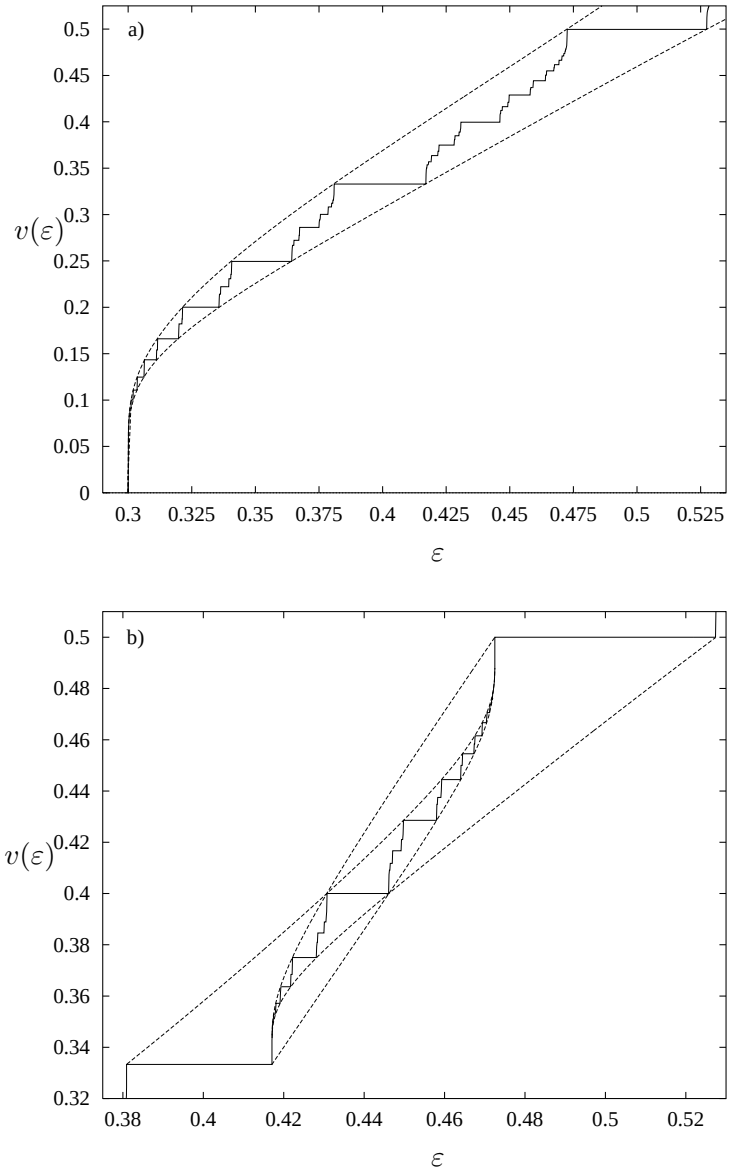

Figure 4.38: Upper and lower envelopes for $v(\varepsilon, 0.4)$. a) The envelopes for the first order plateaus. b) The envelopes of the second order plateaus between $v(\varepsilon) = 1/3$ and $v(\varepsilon) = 1/2$.

In figure 4.38.a we display the first order plateaus for $a = 0.4$. We only plotted the left family ($v \leq 1/2$) since the right family ($v \geq 1/2$) is symmetrical from (2.24). An example of a second order family, for the same value of a, is shown in figure 4.38.b where we display the lower and upper envelopes for the left and right families of second order plateaus between $v = 1/2$ and $v = 1/3$.

With the method described above, it is possible to find the envelopes of any sequence of higher order plateaus via unimodular transformations. The self-similarity structure of the Devil's staircase, evident in figure 4.38, is then controlled by the unimodular transformations (4.48) and the envelopes.

Chapter 5

Higher order interface dynamics

In this chapter the mode-locking phenomenon for travelling fronts with more than one site in the interface is described. We also investigate the mode-locking for CMLs with smooth local maps and reduce the dynamics of the whole interface to a circle map via a delay map. The delay map is shown to account for the velocity of the travelling wave front and its mode-locking through its rotation number. We then study the dependence of the size of mode-locking plateaus on the number of sites in the interface as well on the range of the coupling of the CML.

5.1 High order dynamics of minimal states

In the previous chapter it was established that minimal 1-states for the piece-wise linear CML correspond to a non-negative gap size. Here we investigate the case of a negative gap where there is more than one site in the interface. The dynamics in the negative gap case is N-dimensional, where N is the eventual number of sites in the interface. We show how, in principle, one may find a N-dimensional toral map describing the N-dimensional dynamics of the interface. The velocity mode-locking of the travelling wave front comes from a N-dimensional gap in the same way that for the non-negative gap case.

5.1.1 Convergence to minimal states

When the gap size is non-negative, the dynamics of the whole lattice was reduced to one-dimensional dynamics via the auxiliary circle map. If the gap size is negative there may be more than one site in the interface at the same time. Thus a one-dimensional reduction of the whole lattice does not seem attainable. However, if the number of sites in the interface is still finite —less than or equal to N— one could reduce the dynamics of the whole lattice to a N-dimensional system containing the information of the interface sites.

Before reducing the dynamics, one has to find the parameter regions where a particular number of sites is present in the interface. Minimal 1-states were defined (section 4.2.1) to have $N = 0$ or 1 sites in the interface. Generalizing the idea, define a *minimal mass N-state* or *minimal N-state* to be a minimal mass state having, during its evolution, either $N - 1$

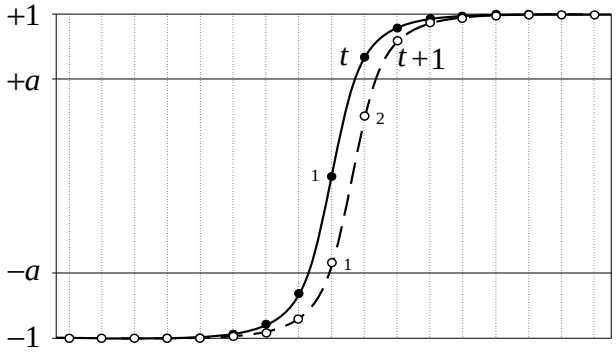

Figure 5.1: The space discretization induces a change on the number of sites in the interface for a travelling front whose shape remains unchanged. At time t (black sites) there is only one site in the interface, though at time $t+1$ (white sites) there are two.

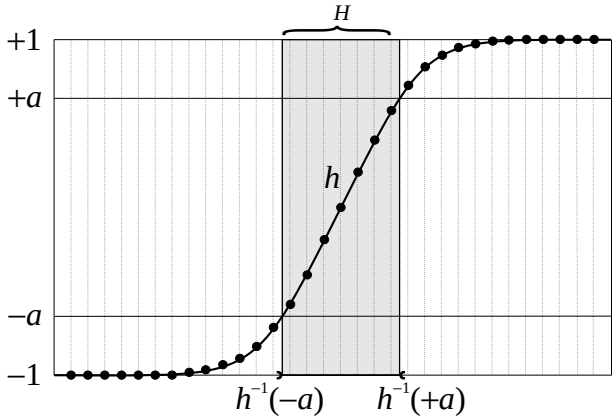

Figure 5.2: The sites belonging to the interface must lie between $h^{-1}(-a)$ and $h^{-1}(+a)$ (shaded area). The number of sites in the interface is determined by the shape h and position, at a particular time, of the propagating front.

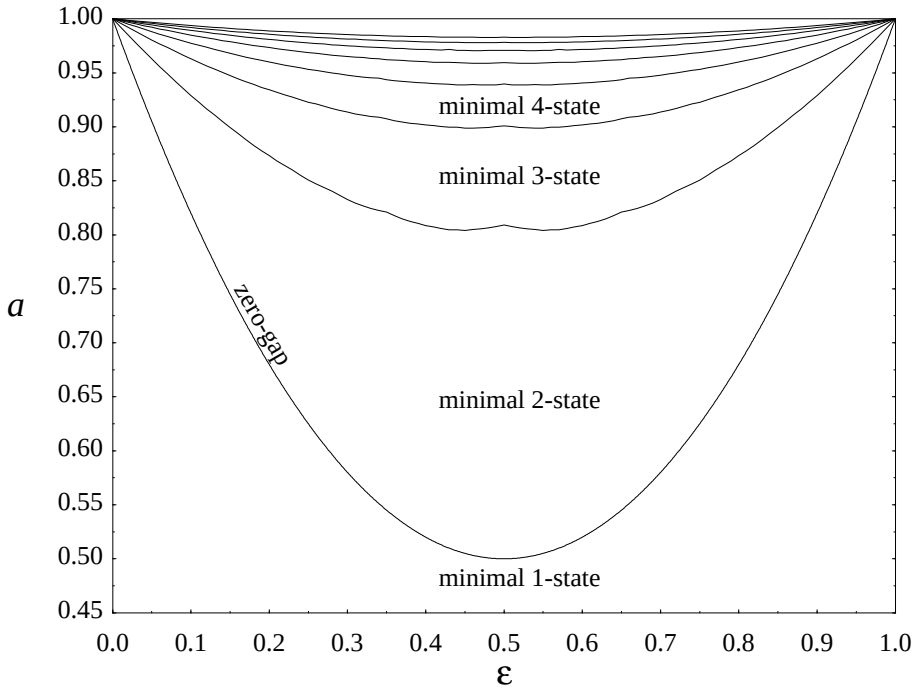

Figure 5.3: Minimal N-states layers in the parameter space. The minimal N-states layers where obtained by numerically iterating an initially minimal 1-state, dropping the transients (1 000 transients) and checking the number of sites in the interface during several iterations (500 iterations). This was done for the parameter range where the gap size is negative in a grid defined by the discretization $(\delta\varepsilon, \delta a) = (0.005, 0.0005)$.

or N sites in the interface. This apparent duality in the definition of a minimal N-state comes from the fact that the front shapes are embedded in a discrete space. Suppose that the shape of the front remains constant during the evolution —as happens for the stationary front in a diffusive CML with a symmetrical local map (section 3.3). Figure 5.1 illustrates how the number of sites may change as the front is shifted when iterating the CML. At time t (black sites) there is only one site present in the interface, while, at time $t+1$ (white sites), the number of sites increases to two. After a further iteration the number of sites in the interface will, eventually, be reduced to one again. This process repeats itself all along the front evolution. Let us explain how. If the front shape is given by the function h (figure 5.2), the sites falling in the interfacial zone, *i.e.* the interface itself, are the sites contained in the interval $H = (h^{-1}(-a), h^{-1}(+a))$ (shaded area). Thus the number of sites in the interface amounts to the number of nodes (black points) in H. Since the length of H and the distance between nodes remains constant, the number of sites in H can only vary by one during the evolution. In the case of a minimal N-state the number of sites in the interface is then N or $N-1$.

In figure 5.3 we depict the (ε, a) regions where the minimal N-states are present. In the calculations, the initial condition was set to be a minimal 1-state which evolved towards a minimal N-state. Numerical experimentation reveals that N does not depend on the initial condition. Any initial configuration we have tried in the interface (figure 5.4) converged to

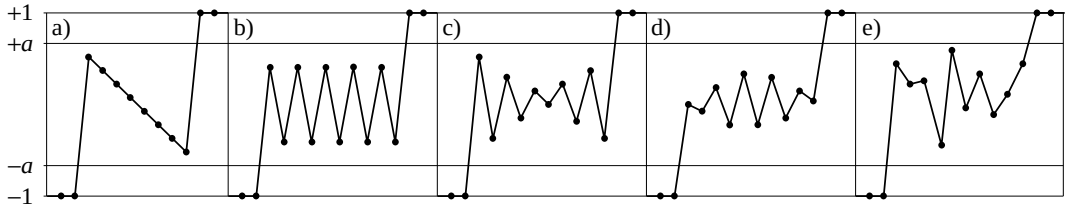

Figure 5.4: Set of initial configurations: a) decreasing, b) oscillatory, c) concave oscillatory, d) convex oscillatory and d) random. All of them tend, after transient, to a minimal N-state where N depends only on the (ε, a)-parameter value.

a minimal N-state depending only on the parameter value (ε, a). Obviously, the length of the transient needed to reach the final minimal N-state depends on the initial configuration. The parameter space is then divided into minimal N-states layers where the value of N is constant. The boundary between the first layer (minimal 1-state) and the second one (minimal 2-state) is the zero-gap curve. Above that curve, the gap is negative, and there appears to be an infinite family of layers, labeled by N, and separated by boundary curves. As it may be observed in figure 5.3, these boundary curves do not seem to be differentiable: they have a fractal-like structure.

5.1.2 Two-dimensional auxiliary map

Throughout this section consider the case $N = 2$, *i.e.* take (ε, a)-parameter values lying in the minimal 2-state layer. One would like to derive an auxiliary map that contains all the information of the interface dynamics as the auxiliary map $\Phi_{\varepsilon,a}$ does for the non-negative gap case. In order to find such a map one has to take into account all possible evolutions of a minimal 2-state. The various possibilities are summarized in figure 5.5. The general form

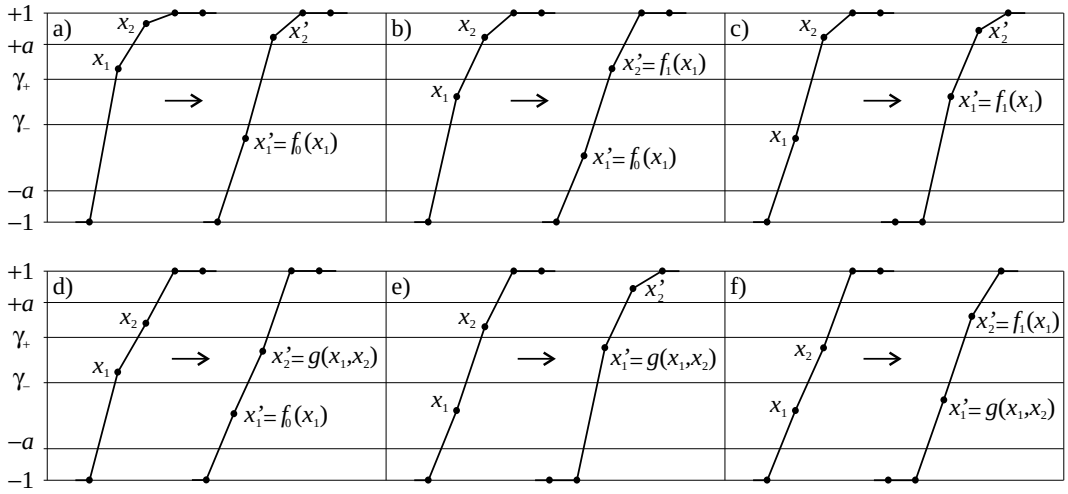

Figure 5.5: Possible evolution combinations of a minimal 2-state. The considered sites are denoted by the pair (x_1, x_2) and their images by (x'_1, x'_2).

for a minimal 2-state X_t is

$$X_t = (-1,\, x_1,\, x_2,\, 1, \ldots),$$

but because the size of the interface may be 1 or 2 one has the two possibilities $-a < x_1 < x_2 < a$ or $-a < x_1 < a \leq x_2$. Therefore, the first site x_1 is always in the interface while the second, x_2, may or may not be in the interface. If the second site is not in the interface one could assign to it any value between $+a$ and $+1$ and its image by the piece-wise linear map f_a would remain the same. In this case we choose to reduce $x_2 \geq a$ to $x_2 = a$. Iterating the state $X_t = (-1,\, x_1,\, x_2,\, 1, \ldots)$ will give one of the 6 possibilities depicted in figure 5.5 where the maps f_0 and f_1 are the same as before (cf. equation (4.6)) and the new map $g(x_1, x_2)$ is

$$g(x_1, x_2) = \frac{1-\varepsilon}{a} x_2 + \frac{\varepsilon}{a} x_1. \tag{5.1}$$

While the map f_0 (f_1) originates from the interaction between the left-most (right-most)

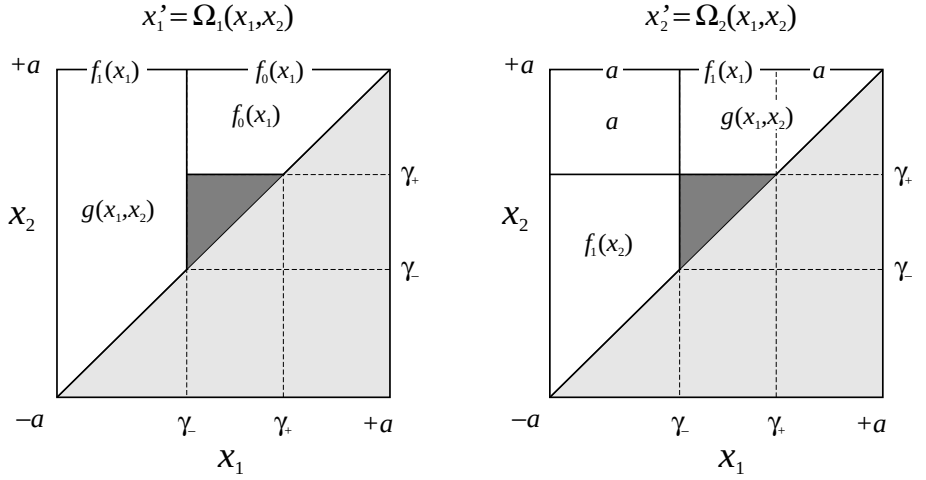

Figure 5.6: The auxiliary map Ω for the two-dimensional case. The pair of interfacial sites (x_1, x_2) is mapped to (x'_1, x'_2) using the indicated functions. The shaded areas are not reachable, see text.

site of the interface with the homogeneous region, the map g originates from the interaction

between the two sites in the interface. Take any of the cases d), e) or f) in figure 5.5 where the pair (x_1, x_2) is in the interface. The image of $X_t = (-1, x_1, x_2, 1, \ldots)$ is then $X_{t+1} = (-1, f_0(x_1), g(x_1, x_2), f_1(x_2), 1, \ldots)$.

Therefore, the pair of interfacial sites (x_1, x_2) is mapped to (x_1', x_2') in 6 different ways depending on their value. The dynamics then induces a two-dimensional map $\Omega(x_1, x_2) = (x_1', x_2')$. The map Ω, obtained by considering the possibilities in figure 5.5, is depicted in figure 5.6 by separating it into its two components $x_1' = \Omega_1(x_1, x_2)$ and $x_2' = \Omega_2(x_1, x_2)$. The shaded areas in figure 5.6 correspond to unreachable situations for a minimal 2-state. Since X_t is a minimal mass state, x_1 has to be less or equal than x_2, thus we eliminate the area where $x_2 < x_1$ —light shaded area. On the other hand, if x_1 and x_2 are both at the same time in the interval $[\gamma_-, \gamma_+]$, the resulting state is a minimal 3-state (figure 5.7), and thus we eliminate this possibility —dark shaded area.

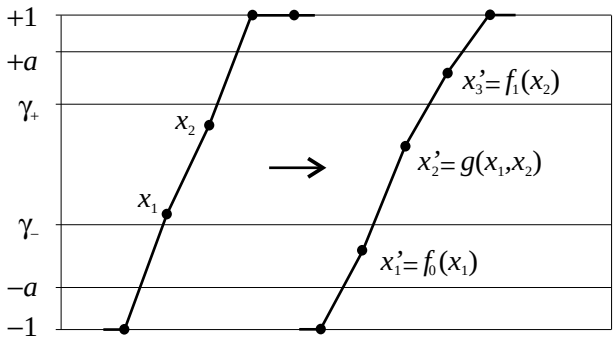

Figure 5.7: Three sites entering in the interface. When $\gamma_- < x_1 < x_2 < \gamma_+$ there is an extra site entering the interface. This does not happen in the minimal 2-state layer.

In the one-dimensional case the auxiliary map $\Phi_{\varepsilon,a}$ is a one-dimensional circle map whose rotation number gives the velocity of the travelling interface. For the 2-dimensional case (minimal 2-state layer) the auxiliary map Ω is a toral map in two dimensions —a toral map is the generalization of a circle map to more than one dimension (cf. [63]). In figure 5.8 we plot the maps $\Omega_1(x_1, x_2)$ and $\Omega_2(x_1, x_2)$ (they are from $\mathbb{R}^2$ to $\mathbb{R}$) separately.

Generalizing the idea of rotation number in more dimensions one could think of a *rotation vector* [63] whose entries correspond to the rotation number in every component. The rotation vector $\rho = (\rho_1, \rho_2)$ of $\Omega(x_1, x_2)$ is then two-dimensional. But since both sites (x_1, x_2) belong to the same interface, that is moving with a defined velocity, the two components of the rotation vector have to be equal ($\rho_1 = \rho_2$). This observation is the key point for reducing the dynamics of any interface to a one-dimensional map and will be addressed again in section 5.2.1. Therefore instead of taking the whole rotation vector one may use a single scalar to describe the rotation around $\Omega(x_1, x_2)$. Thus, the velocity of the travelling interface in the minimal 2-state layer is given by this scalar, which will be simply called from now, the rotation number of $\Omega(x_1, x_2)$.

5.1.3 The tongues for the two-dimensional case

The two-dimensional auxiliary map Ω is piece-wise linear —it is a combination of planes— and possesses the equivalent of the gap Γ for the one-dimensional case: the region $[-a, \gamma_-] \times [\gamma_+, a]$,

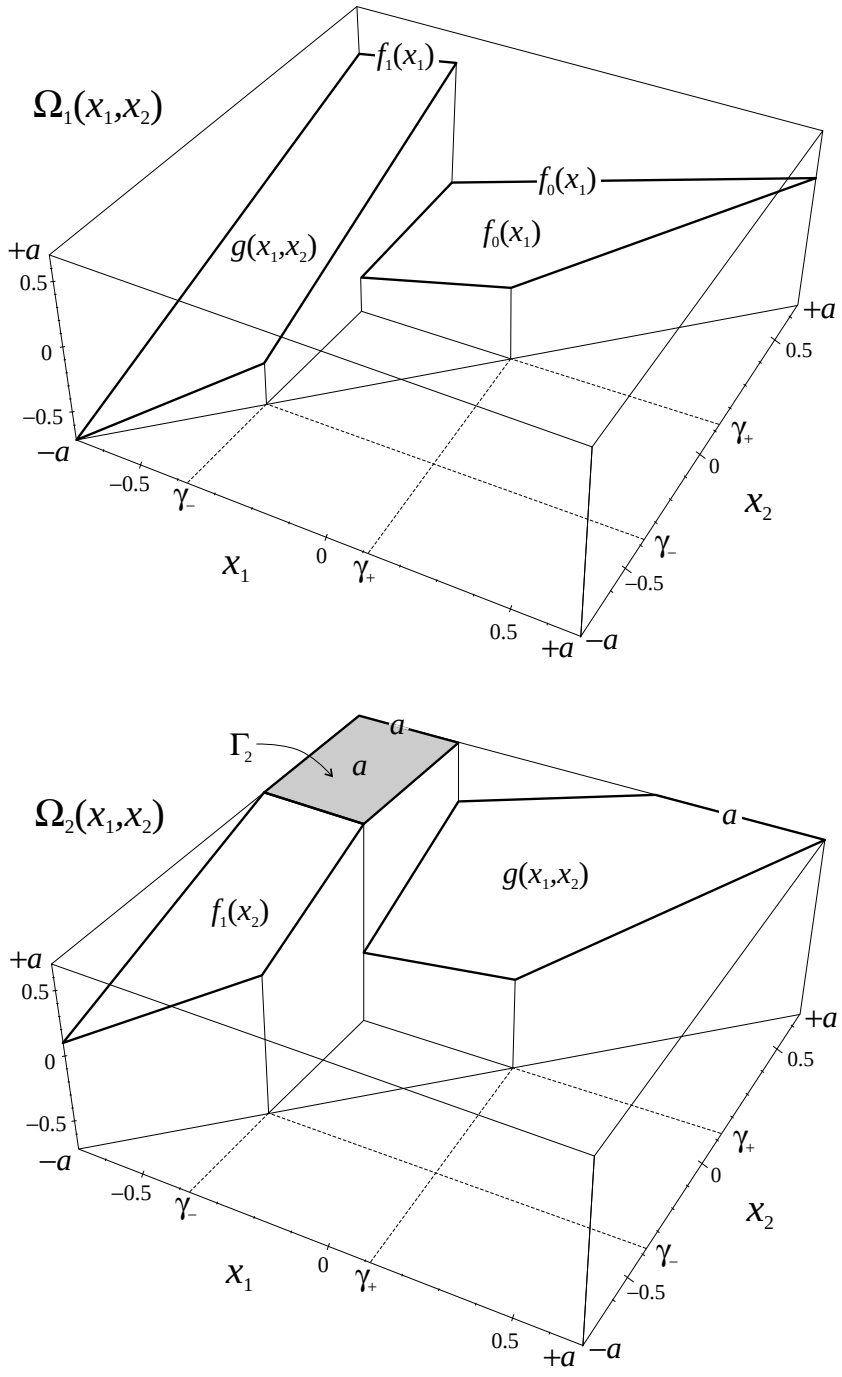

Figure 5.8: Plot of the two-dimensional auxiliary map $\Omega(x_1, x_2) = (\Omega_1(x_1, x_2), \Omega_2(x_1, x_2))$ in three dimensions for $(\varepsilon, a) = (0.365, 0.7)$.

see shaded region in figure 5.8. This region, which we refer to as the *two-dimensional gap* and denote by Γ_2, acts in the same way as its one-dimensional analogue. Any (x_1, x_2)-orbit falling into Γ_2 —a gap orbit— is superstable and therefore is parametrically stable to perturbations. This parametric stability gives rise to the mode-locking of the velocity. Thus one expects the minimal 2-state layer to contain Arnold's tongues in the same way the minimal 1-state layer does.

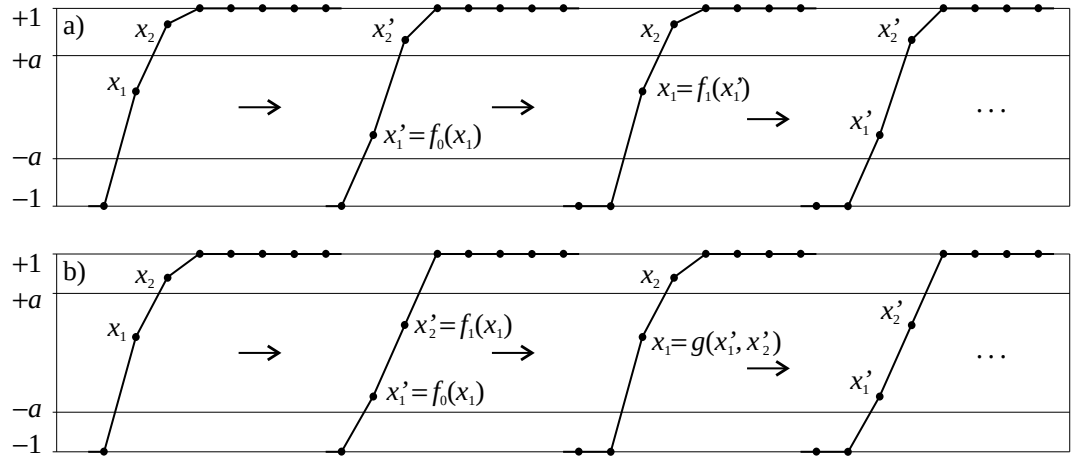

Figure 5.9: The two possible orbits giving $v = 1/2$ in the two-dimensional case.

Let us derive the tongues for $v = 1/2$ in the two-dimensional case. First of all one has to choose the orbit. In the one-dimensional case the orbit was uniquely determined by the symbolic coding of the velocity for fixed values of (ε, a). However, in the two-dimensional case, there are different possible evolutions for a given velocity. This is due to the fact that with more sites in the interface a wider selection of orbits is possible. Two such orbits of a minimal 2-state giving a velocity $v = 1/2$ are depicted in figure 5.9, that is, a) with $x_2 > a$ all the time and b) alternating one and two sites inside the interface. First of all the orbit has to be periodic (period two). Therefore we must have a) $f_1(x_1' = f_0(x_1)) = x_1$ and b) $g(x_1' = f_0(x_1), x_2' = f_1(x_1)) = x_1$, *i.e.*

$$\begin{aligned} &\text{a)} \qquad x_1 = \frac{a(a(1-\varepsilon)-\varepsilon^2)}{a^2-\varepsilon(1-\varepsilon)}, \\ &\text{b)} \qquad x_1 = \frac{a(1-2\varepsilon)}{a^2+2\varepsilon(\varepsilon-1)}. \end{aligned} \tag{5.2}$$

Now, one has to verify that the sites fall in the right intervals. From figure 5.9 is easy to check that the conditions on the orbit a) and b) are

$$\begin{aligned} &\text{a)} \qquad f_1(x_1) > a \quad \text{and} \quad f_0(x_1' = f_0(x_1)) < -a, \\ &\text{b)} \quad f_0(x_1' = f_0(x_1)) < -a \quad \text{and} \quad f_1(x_2' = f_1(x_1)) > a. \end{aligned} \tag{5.3}$$

Combining equations (5.2) and (5.3) gives the conditions that ε and a must satisfy in order to have the period-2 orbits of figure 5.9. In figure 5.10 we display the regions where these conditions are satisfied in the minimal 2-state layer.

The same procedure may be applied to find the tongues for any rational velocity in the minimal 2-state layer. From the numerical experiments it is seen that for every chosen

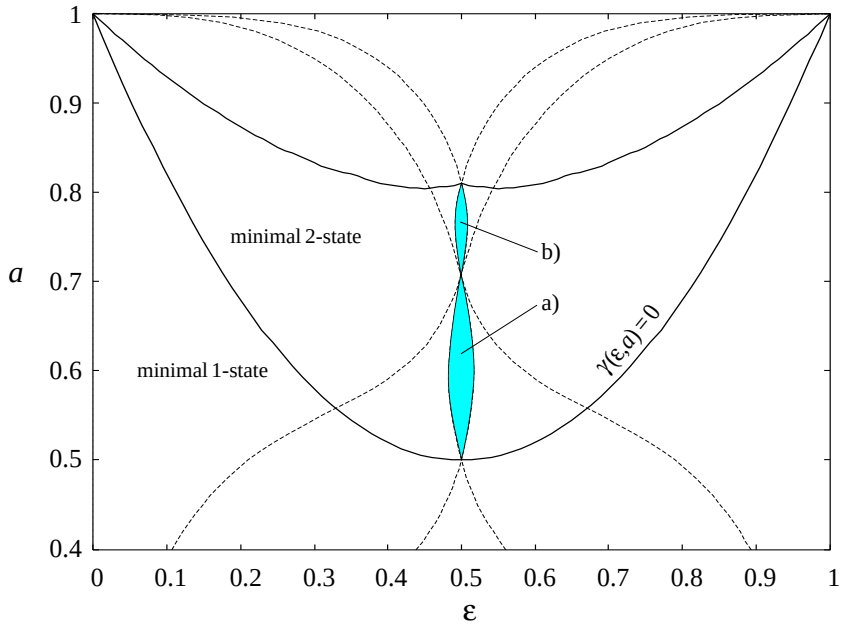

Figure 5.10: The $v = 1/2$ tongues in the minimal 2-state layer. The tongues a) and b) are obtained by solving the inequalities (5.3) corresponding to the two period-2 orbits in figure 5.9.

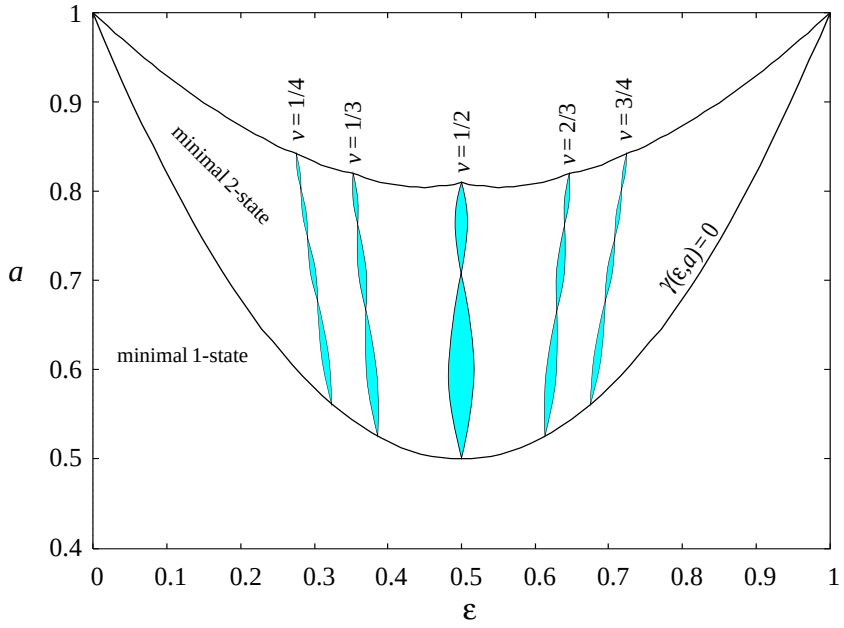

Figure 5.11: Principal mode-locking tongues in the minimal 2-state layer. One verifies that the number of tongues in this layer corresponds to the denominator of the velocity.

$0 < v = p/q < 1$ there are q possible different orbits, by combining 1 and 2 sites in the interface, each one has a corresponding tongue in the minimal 2-state layer. In figure 5.11 we present the computed tongues for the principal rational velocities. The number of tongues for a given velocity corresponds to the denominator of the latter.

5.1.4 Higher order dynamics

Now let us consider the case of a minimal N-state layer for $N > 2$. The dynamics in that layer may be reduced to a N-dimensional auxiliary toral map that controls the N-tuplet of sites in the interface. Again, thanks to the superstable regions of the local map, this N-dimensional toral map will have a N-dimensional gap Γ_N such that any N-tuplet in Γ_N is mapped unto a by the N-dimensional auxiliary map. The parametric stability is again induced by the presence of the gap Γ_N when the latter exists.

Thus, in every minimal N-state layer there are q tongues corresponding to the velocity $v = p/q$ given by the q possible combinations for the periodic-q orbit, of the N-dimensional auxiliary map. The regions where each tongue exists are given by a system of inequalities that the N-tuplet has to satisfy for the orbit to undergo the right combination of N and $N-1$ sites in the interface. In figure 5.12 we show the tongues for the velocities $v = 1/2$, $2/5$, $1/3$, $2/7$ and $1/4$ in the minimal N-state layers for $N = 1, \ldots, 8$. We call the tongues in the minimal N-state layer the *sub-N-tongues* since they emanate from the principal mode-locking tongues, the *principal tongues*, for the one-dimensional case. Therefore, every principal tongue has q sub-N-tongues in each N-layer. Observing carefully the enlargement in figure 5.12 one notices that the structure of these sub-tongues is self-similar and repeats itself in every layer. Besides of the self-similarity in the a-axis, there is a self-similarity in the ε direction inherited from the principal tongues (the fractal Devil's staircase).

It is interesting to notice that because of the continuity of $v(\varepsilon, a)$ all the sub-N-tongues touch each other. Another point to be addressed is that the sub-N-tongues touch in a single point, *i.e.* in that particular point the width of the ε-plateau (for a fixed value of a) is zero. This phenomenon is repeated all along each family of sub-N-tongues and it happens every time a site of the interface touches the boundary of the superstable region when varying the (ε, a)-parameters in order to go from one of the q possible combinations of the interface orbit to the next. In figure 5.13 we show the state of the lattice at different stages of the $v = 1/3$ tongue. The ε-width of the latter is zero in the transitional case between two different interfacial orbits (cases b), d), f) and h)). One may consider this switch from one interfacial orbit to the next as a bifurcation of the attracting cycle of the N-dimensional auxiliary map [64]. In order to illustrate when this bifurcation takes place we show the bifurcation diagram of the attracting cycle of the interface in figure 5.14 as the parameter a is varied. From the figure it is possible to observe that when a stable point of the interface touches the boundary of the superstable region (dashed diagonal lines a and $-a$) the attracting cycle changes and one site is added to it. Where this happens (vertical dashed lines) the ε-width of the tongue is zero (see figure 5.13).

With these remarks our study of the one-way CML with the piece-wise local map f_a is concluded. In the rest of these thesis we present further results, mainly numerical, showing the mode-locking phenomenon in a wider range of CMLs.

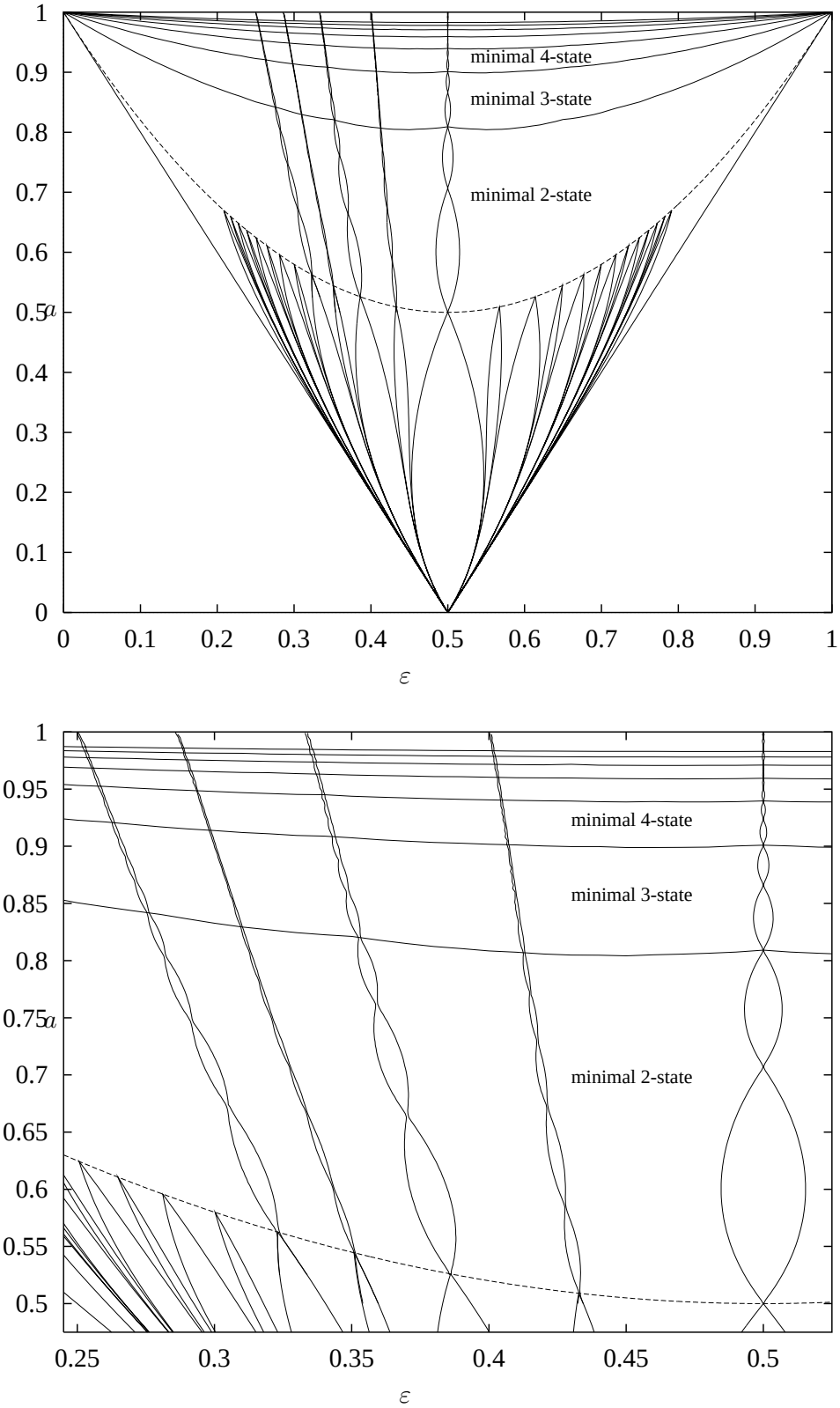

Figure 5.12: a) Tongues in the high dimensional minimal N-state layers. The tongues for the velocities $v = 1/2,\ 2/5,\ 1/3,\ 2/7$ and $1/4$ in the minimal N-state layers for $N = 1, \ldots, 8$ are presented. b) Enlargement of the upper-left section of a).

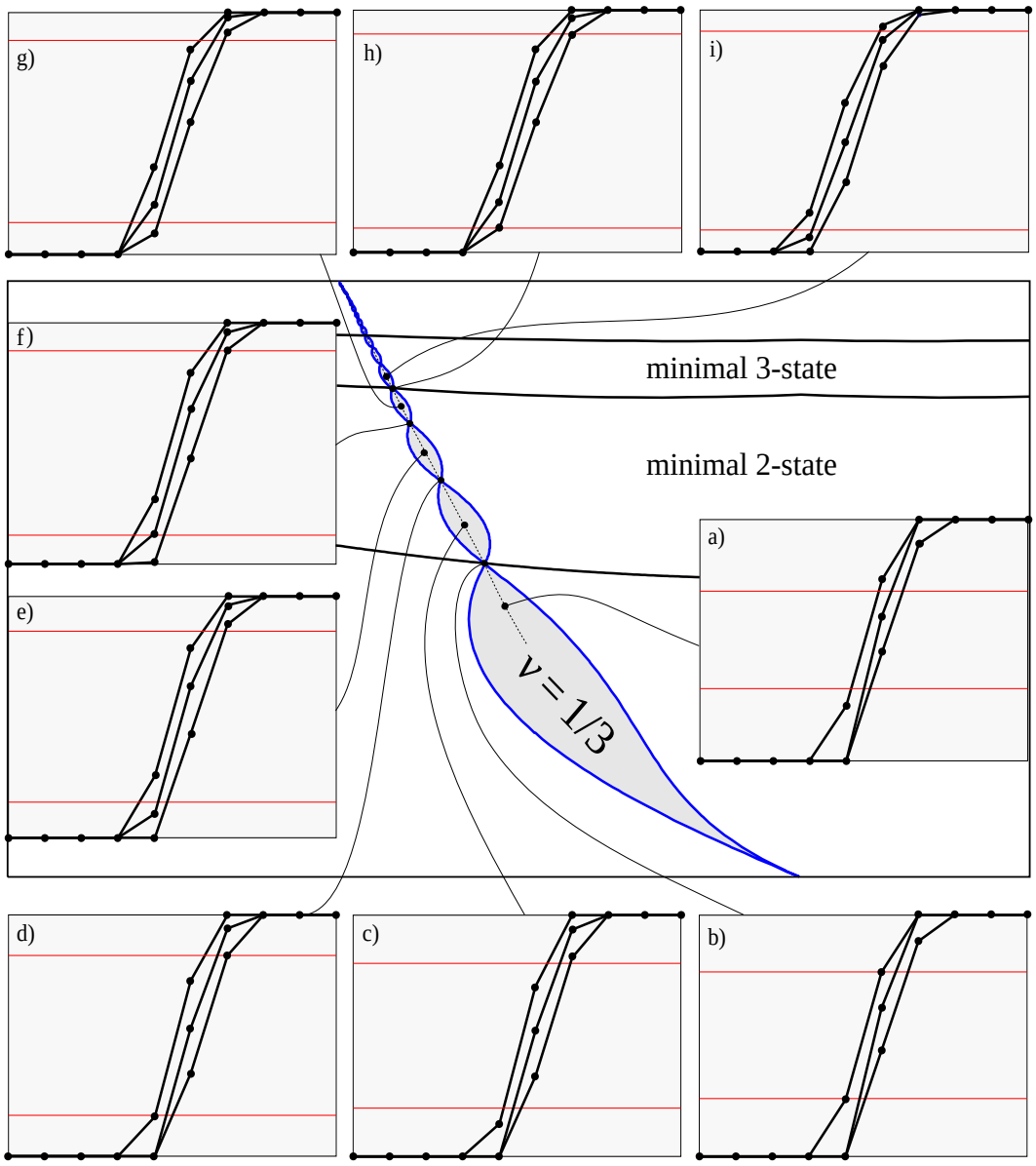

Figure 5.13: Successive states of the lattice in the $v = 1/3$ tongue. Every time a site touches the boundary of the superstable region, in order to pass to a new configuration, the tongue ε-width is zero. The states from a) to i) correspond to increasing values of a inside the $v = 1/3$ tongues. The state a) is a minimal 1-state while the state b) is the transitional state to a minimal 2-state (zero gap). The states c), e) and g) correspond to the three different possibilities for a minimal 2-state and d) and f) correspond to the transition points between these three states. State i) is already is a minimal 3-state and h) is the transition point between the minimal 2-state to the minimal 3-state.

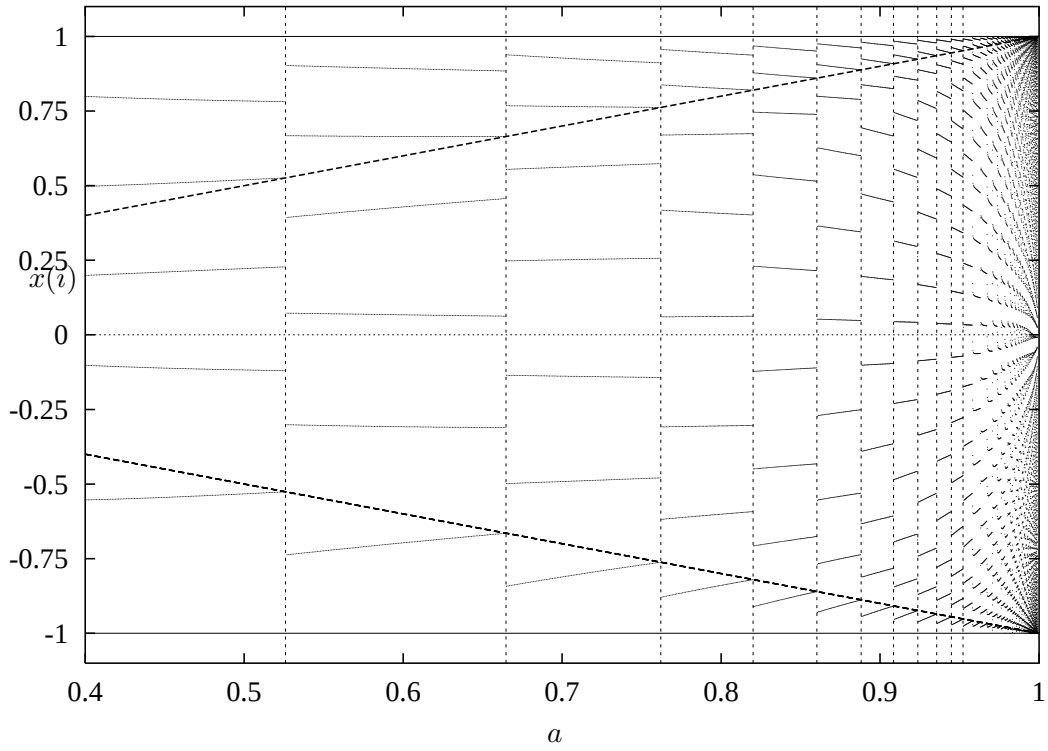

Figure 5.14: Bifurcation diagram of the attracting cycle of the interface sites in the $v = 1/3$ tongues. We plot the stable periodic 3 orbit of the interfacial sites as a function of the parameter a after 10 000 transients.

5.2 Mode-locking for smooth maps

The goal of this section is to generalize the previous results by providing evidence that the mode-locking phenomenon is common in the propagation of fronts in both one-way and diffusive CMLs. The basic task is to understand the mode-locking process for the case of a smooth local map that does not possess a superstable gap —recall that the gap is responsible for the parametric stability for the piece-wise linear local map case.

5.2.1 Mode-locking in one-way CMLs

Let us consider again the example given in section 3.4 where the local map is the hyperbolic tangent $\tanh(x/\nu)$. The whole picture of the parameter space in given in figure 5.15 where we depict the principal Arnold's tongues for the one-way CML with $f(x) = \tanh(x/\nu)$. As it may be observed from the figure the mode-locking regions rapidly shrink as ν tends to 1 — with the exception of the plateaus $v = 0/0$ and $v = 1/1$ which remain considerably large even for $\nu \simeq 1$. The same remark can be noticed from figure 3.14 where the mode-locking plateaus tend to disappear as ν increases. The question that now arises is that of the existence of mode-locking plateaus for large ν. In figure 5.16 we have the velocity for $\nu = 2/5$, the curve appears to be smooth for $\varepsilon_c < \varepsilon < 1/2$, at least at the observable scale. Do the mode-locking plateaus really disappear as ν tends to 1? In figure 5.17 we show a magnification of the velocity curve for $\nu = 2/5$ around $v = 1/3$. The plateau around $v = 1/3$, which was invisible in figure 5.16, now appears clearly.

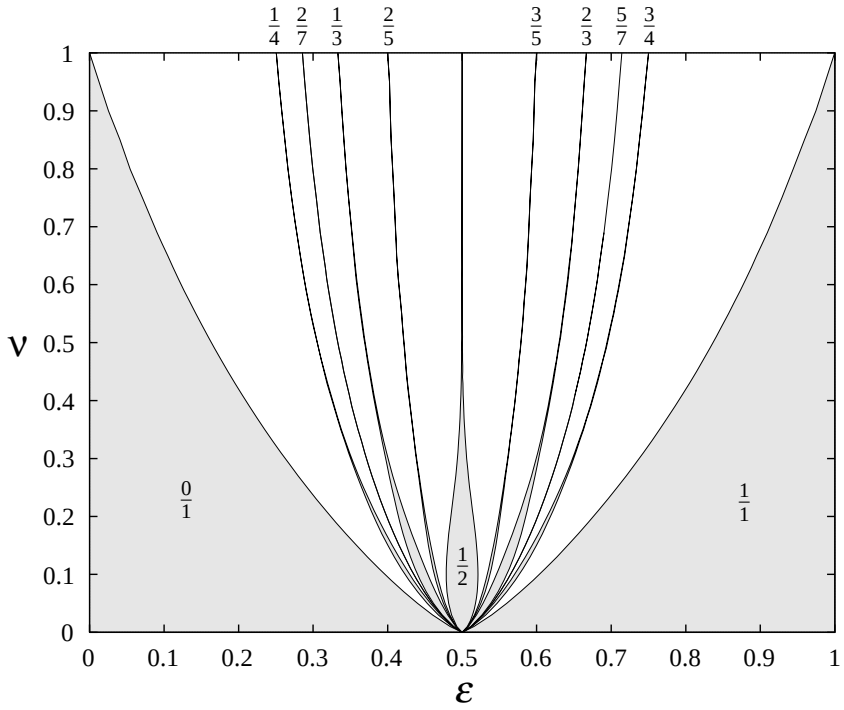

Figure 5.15: Arnold's tongues for the one-way CML with the hyperbolic tangent local map $f(x) = \tanh(x/\nu)$.

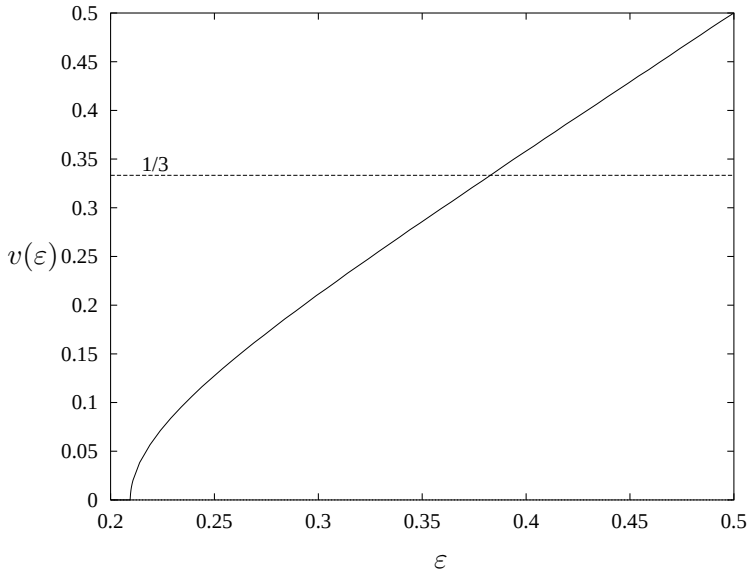

Figure 5.16: Velocity curve for the hyperbolic tangent local map with $\nu = 2/5$. At this scale no mode-locking plateau for the velocity is observable.

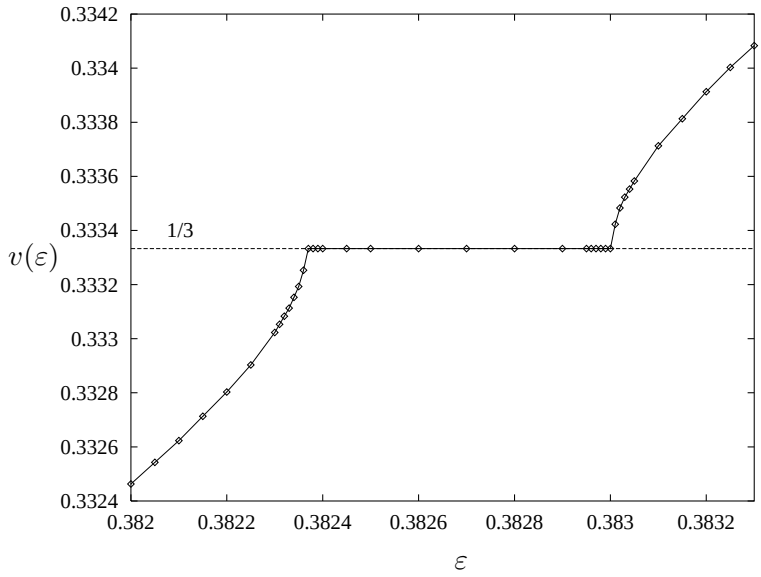

Figure 5.17: Enlargement of figure 5.16 around $v = 1/3$. The $v = 1/3$ plateaus is now clearly observable.

This numerical experiment gives evidence that the mode-locking may be present on a small scale. In order to understand this mode-locking for smooth maps and the mechanism whereby the plateaus tend to disappear, one could try to find the corresponding auxiliary map for the given local map. The number of sites N in the interface for smooth local maps is typically infinite because there is not, in general, a superstable region. For the piece-wise linear local map, a site falling in the superstable regime is set to the stable point after one iteration, whereas for an smooth map the tendency towards the superstable point may take an infinite time. Therefore it would be unpractical to find the associated N-dimensional auxiliary map since it would be infinite. Thus, in order to have a simpler picture of the interface dynamics one could try to reduce further the dynamics.

Suppose there are N sites in the interface, where N could be infinite, and that the front is mode-locked in the $v = p/q$ plateau. The orbit of the interface N-tuplet is then periodic with period q and so is every one of its components. Thus one may focus on the dynamics of a single site of the interface, since all the other interfacial sites are slaved to the same period. The dynamics of the chosen site is then periodic with period q and the mode-locking phenomenon should be reflected in its dynamics. Let us choose the j-th site of the interface (*i.e.* $1 \leq j \leq N$) and denote by $x_j(t)$ its dynamics. It is important to notice that the global index of this site advances, as the CML is iterated, since the interface advances through the lattice (for $v \neq 0$).

From the N sites of the interface choose, for the following numerical examples, the site whose dynamics is closer to the unstable point x_0^* of f. In the case of symmetrical f the unstable point is $x_0^* = 0$ and thus the dynamics of the chosen site happens around the origin. We call this site the *central site* since, because of symmetry, it is at the centre of the interface. We then reconstruct its dynamics, denoted $x_c(t)$, by taking the delay map $x_c(t+1)$ vs. $x_c(t)$. The orbit $x_c(t)$ is periodic of period q (because $v = p/q$) and the delay map of $x_c(t)$ consists of q points. If q is small it is impossible to reconstruct a continuous map giving the global dynamics of $x_c(t)$. However, by considering a small perturbation of ε one could change the period of the orbit without affecting much the front dynamics. Suppose that the $v = p/q$

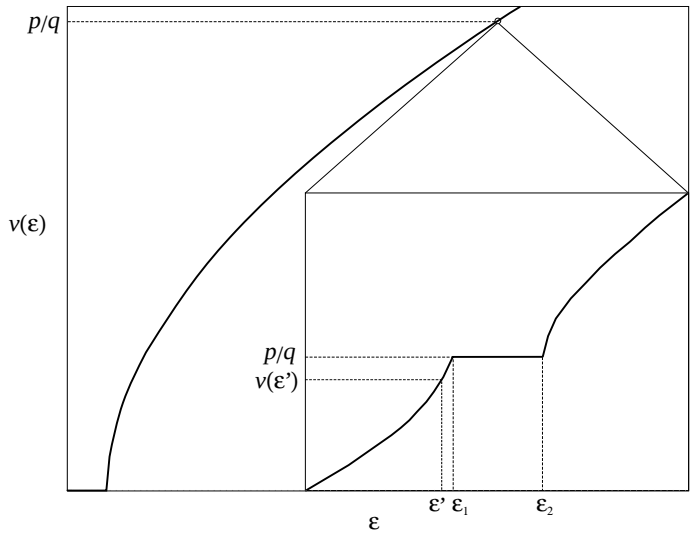

Figure 5.18: Taking an ε-value near a mode-locking plateau allows a better reconstruction of the interface dynamics without changing considerably the front velocity.

plateau happens in the interval $(\varepsilon_1, \varepsilon_2)$, take a value ε' such that $\varepsilon' < \varepsilon_1$ and $|\varepsilon' - \varepsilon_1| \ll 1$ (figure 5.18). If $v(\varepsilon)$ is continuous, $v(\varepsilon')$ can be made as close as desired to p/q by choosing ε' close enough to ε_1. The same procedure could also be applied near ε_2, *i.e.* $\varepsilon' > \varepsilon_2$ and $|\varepsilon' - \varepsilon_2| \ll 1$. The resulting reconstructed dynamics for the central site, now denoted $\tilde{x}_c(t)$, at this new ε-value has a large period but the velocity of the front remains close to p/q, *i.e.* $\tilde{x}_c(t) \simeq x_c(t)$. The large period permits us to visualize the shape of the auxiliary map.

As an example consider again the $v = 1/3$ plateau of the travelling interface for the hyperbolic tangent auxiliary map when $\nu = 2/5$. From the enlargement of the velocity (figure 5.17) one could give and approximation of the interval $(\varepsilon_1, \varepsilon_2) \simeq (0.38237, 0.383)$ and we choose $\varepsilon' = 0.3823$ such that $\varepsilon_1 - \varepsilon' \simeq 0.00007$ and $|v(\varepsilon') - 1/3| \simeq 0.000377$. In figure 5.19 we plot the delay map of the central site for $\varepsilon = \varepsilon' = 0.3823$. We can see that the dynamics for this reconstructed delay map is very close to a period-3 orbit (see the 3 orbits in figure 5.19). The clue for the mode-locking phenomenon relies on this delay map. The delay map contains the information of the dynamics of the central site, it is equivalent to the auxiliary map for the piece-wise linear CML and it is a circle map. The delay map plays then the same role as the auxiliary map and thus if there is a mode-locking in the travelling velocity it should come from the mode-locking of its rotation number. If the local map is nonlinear we expect the delay map to be nonlinear as well. Therefore the mode-locking of the rotation number for a smooth map in a one-way CML is a strictly nonlinear phenomenon triggered by the nonlinearity of the delay map in the same way as the mode-locking in the standard circle map [57].

5.2.2 Mode-locking in diffusive CMLs

The same delay map reconstruction may be carried out for a diffusive CML. As an example, let us consider as local map the second iterate of the logistic map $f(x) = \mu x(1-x)$, see figure 5.20, restricted to the interval between its superstable points $x^*_\pm$ for $\mu = 1 + \sqrt{5}$. The local map is then asymmetric with respect to the repeller x^*_0 and thus can propagate

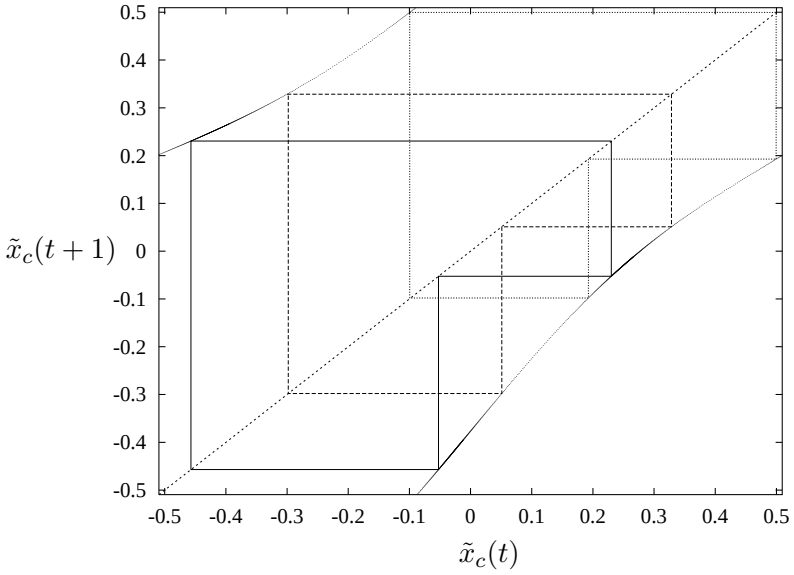

Figure 5.19: Reconstructed delay map of the central site of the interface of the travelling wave front for the hyperbolic tangent local map with $\nu = 2/5$ and $\varepsilon = 0.3823$. The parameter value $\varepsilon = 0.3823$ is nearby the $v = 1/3$ plateau so the dynamics mimics very closely the one for the $v = 1/3$ plateau: the orbits have period-3.

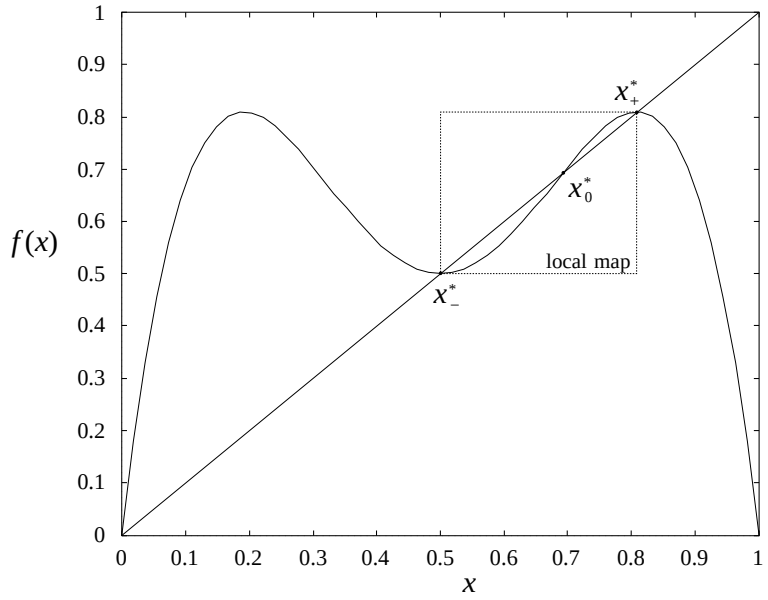

Figure 5.20: The second iterate of the logistic map with $\mu = 1 + \sqrt{5}$. For this value of the parameter μ the second iterate of the logistic map possesses a suitable local map —the one inside the dashed square— for the propagation of a travelling interface in a diffusive CML, *i.e.* it has two superstable points $x_\pm^*$ separated by the unstable one x_0^* and it is not symmetric.

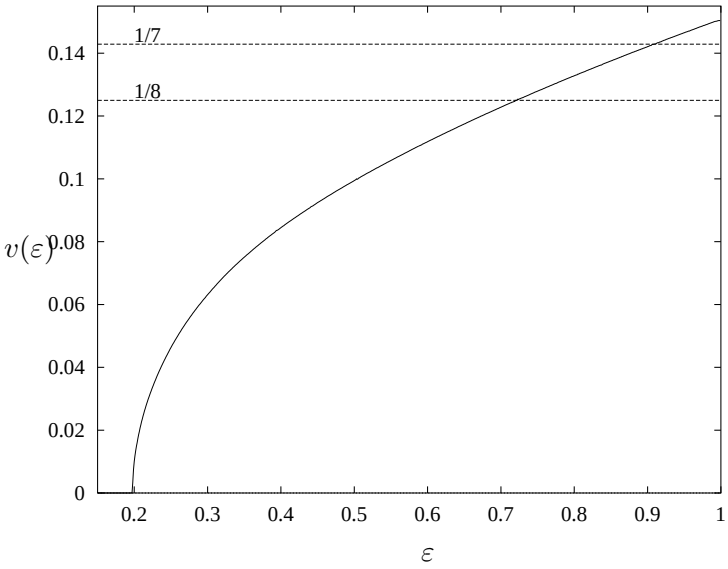

Figure 5.21: Velocity of the travelling interface for the second iterate of the logistic map in a diffusive CML. The curve seems to be smooth without any apparent mode-locking plateaus.

interfaces in a diffusive CML. The velocity of the travelling interface is shown in figure 5.21. It exhibits an apparently smooth dependence on the coupling parameter without mode-locking plateaus. Nonetheless, magnifications around $v = 1/7$ and $v = 1/8$ clearly show plateaus on a smaller scale (figure 5.22). Therefore, the mode-locking phenomenon is also present under magnification from a curve that appeared to be smooth at the first glance.

Following the same procedure as in the previous section, we reconstruct the delay map for an ε-value near the $v = 1/7$ plateau of figure 5.22.a. We take the value $\varepsilon' = 0.9075$ and reconstruct the delay map of the central site (figure 5.23). In this case the reconstructed delay map is almost linear, which is the reason why the mode-locking plateaus are barely detectable. Nonetheless, the delay map is nonlinear —compare the lower part of the reconstructed delay map with the fine straight line— and as such displays a weak mode-locking w.r.t. ε as seen in figure 5.22.

It should be clear now that one-way or diffusive CMLs, whose local map is nonlinear in order to propagate wave fronts, are likely to display velocity mode-locking with respect to the coupling parameter. The size of the plateaus may be, however, very small. The goal of the next section is to study the dependence of the plateaus size on the features of the local map and the range of the coupling.

5.3 Width of the mode-locking plateaus

In this section we relate the size of the mode-locking plateaus to the number of sites present in the interface and, finally, we turn around the problem to the range of the coupling for an exponentially decaying interaction.

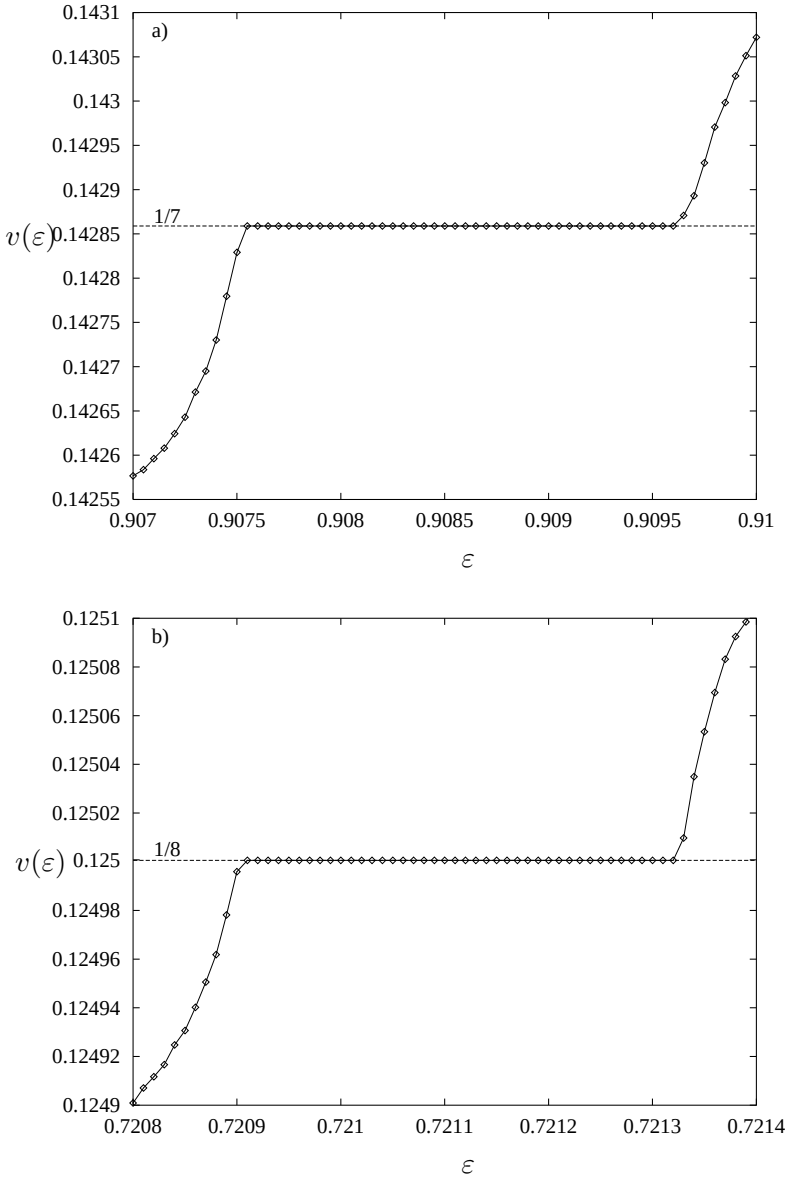

Figure 5.22: Enlargement of the velocity for the second iterate of the logistic map in a diffusive CML. The plateaus of a) $v = 1/7$ and b) $v = 1/8$ are clearly observable at this scale.

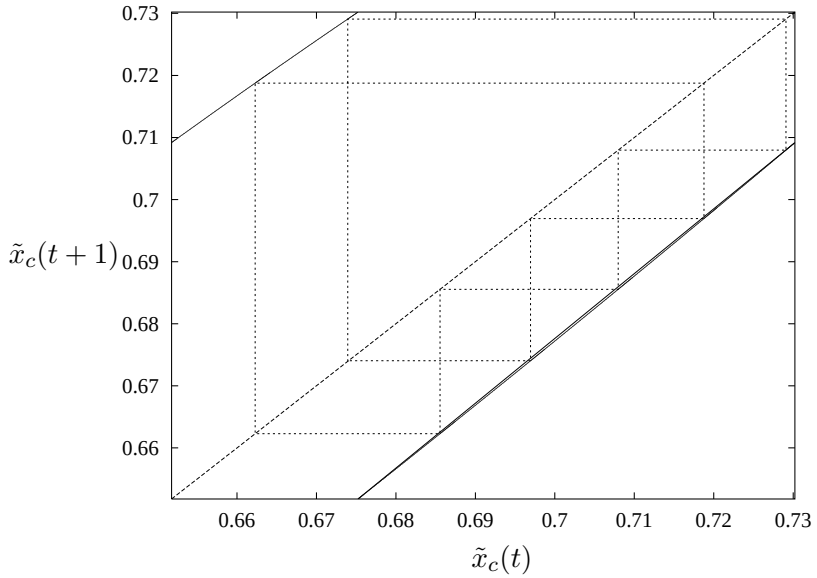

Figure 5.23: Reconstructed delay map of the central site of the interface of the travelling wave front for the second iterate of the logistic map with $\mu = 1 + \sqrt{5}$ and $\varepsilon = 0.9075$ in a diffusive CML. The parameter value $\varepsilon = 0.9075$ is nearby the $v = 1/7$ plateau so the dynamics mimics very closely the one for the $v = 1/7$ plateau: the orbit has almost period-7.

5.3.1 Mode-locking versus number of sites in the interface

As noticed in section 5.2.1 the mode-locking plateaus tend to disappear as ν increases (figure 5.15) in the one-way CML with local map $f(x) = \tanh(x/\nu)$. For large values of ν ($\nu \simeq 1$) the plateaus are almost imperceptible and they become more evident as ν is decreased. In order to understand this behaviour we shall monitor the average number of sites in the interface as a function of ν. In figure 5.24 we have the dependence of the average number of sites in the interface $\overline{N}$ on the parameter ν. It is important to say that the interface in such smooth maps is very difficult to characterize since it typically involves infinitely many sites. One could try to use the width σ^2 (cf. section 2.1) of the travelling interface (see figure 5.25) whose size is finite. But as we shall see, for the purpose of the interface dynamics, it is more useful to think of the number of sites in the interface.

Let us understand how the interfaces are infinite. Far from the localized region of the interface, the sites tend to x^*_- (left) and to x^*_+ (right). The specific tendency towards the stable points depends on the nature of the coupling and the local map. Far from the central region of the interface, *i.e.* near the stable points $x^*_\pm$, the lattice is almost homogeneous. In other words $x(i) \simeq x(i+1) \simeq x(i-1) \simeq x^*_\pm$ if $i \to \pm\infty$, thus the dynamics of these sites could be rewritten as

$$\begin{aligned} x_{t+1}(i) &= (1-\varepsilon) f(x_t(i)) + \tfrac{\varepsilon}{2}\left(f(x_t(i-1)) + f(x_t(i+1))\right) \\ &\simeq (1-\varepsilon) f(x_t(i)) + \tfrac{\varepsilon}{2}\left(f(x_t(i)) + f(x_t(i))\right) \\ &\simeq f(x_t(i)) \end{aligned}$$

for a diffusive CML and the same result is obtained for a one-way CML. Therefore the dynamics far from the central part of the interface is mainly governed by the attraction of the local map towards the stable points. Hence the decay very near the attractors follows

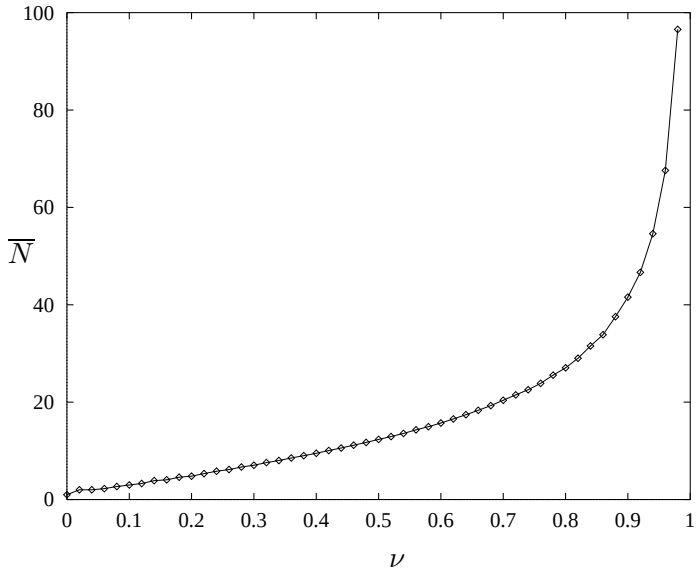

Figure 5.24: Average number of sites in the interface of the travelling wave front. We used a one-way CML with the hyperbolic tangent local map $f(x) = \tanh(x/\nu)$. We set $\varepsilon = 0.45$ and averaged the number of sites in the region $[x_-^* + \delta, x_+^* - \delta]$, with $\delta = 10^{-12}$, over 100 iterations.

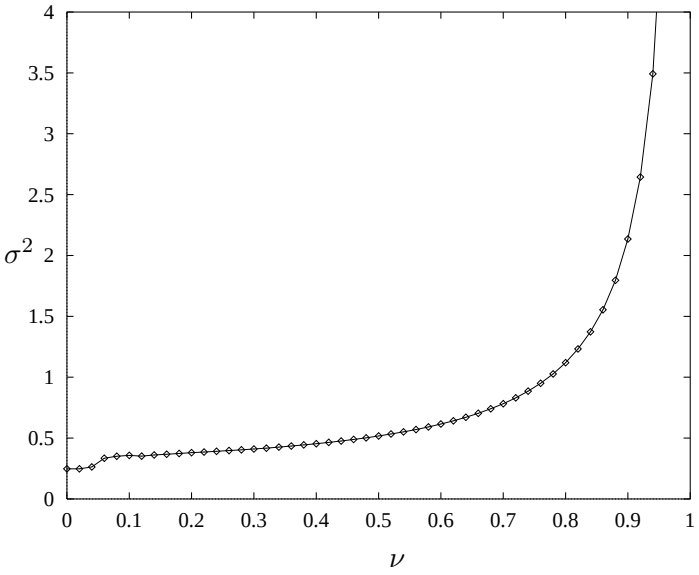

Figure 5.25: Width of the travelling interface for the hyperbolic tangent local map with $\nu = 0.45$ as in figure 5.24.

the decay of the dynamics of the local map. For a linear attractor the decay is exponential, thus the decay rate for a typical nonlinear stable point will be at least exponential. The only way to avoid an infinite interface is to give a superstable region to the stable points, like the piece-wise linear map used in the previous chapter. Such kind of maps possess flat regions around $x^*_\pm$ that 'artificially' collapse trajectories that get close enough to $x^*_\pm$. For smooth local maps without such superstable regions, the convergence towards $x^*_\pm$ is an infinite process giving rise to an infinite interface. Nevertheless, any numerical analysis has a limited accuracy producing an artificial superstable convergence towards an attracting point. Imagine we are numerically iterating a local map near a stable point, after a finite number of iterations the distance of our trajectory from the stable point gets smaller than the accuracy of our calculations and thus the trajectory is instantaneously set at the stable point. In this case, the accuracy of our calculations defines the size of the artificial superstable region around the stable point. Thanks to that, interfaces for smooth local maps, that in theory are infinite, become finite. Therefore, from now on, to have a finite and manageable size of the interface, we use a truncated interface $[x^*_- + \delta, x^*_+ - \delta]$ with $\delta \ll 1$, *i.e.* the number of sites contributing to the interface are the ones in this truncated interval.

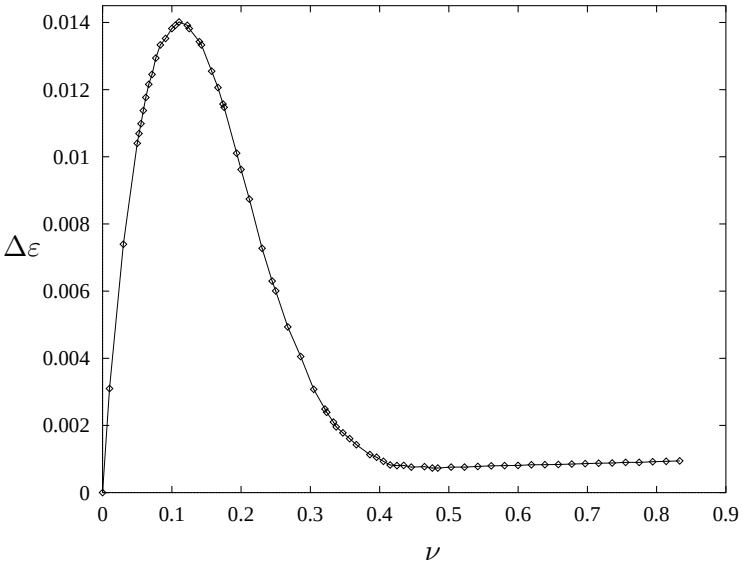

Figure 5.26: Size of the $v = 1/3$ plateau, $\Delta\varepsilon = \varepsilon_2 - \varepsilon_1$, for the hyperbolic tangent local map as a function of ν.

Using figure 5.15 with figures 5.24 and 5.25 one can conclude that for this example the size of the plateaus decreases as the number of sites in the interface gets larger. To obtain a clearer picture we computed the left (ε_1) and right (ε_2) extremes of the $v = 1/3$ plateau as a function of ν and calculated its size size $\Delta\varepsilon = \varepsilon_2 - \varepsilon_1$ (figure 5.26). Peculiar behaviour occurs at the right extreme of the ν spectrum. We expected $\Delta\varepsilon$ to be a decreasing function of ν for large ν ($\nu \simeq 1$) but the figure shows an increasing tendency of $\Delta\varepsilon$ for $\nu > 0.45$. We show now that the problem is strictly numerical: when ν is close to 1 the plateaus are so small that we are at the limit of the computational accuracy for the velocity —we took for this example 999 iterations plus 100 transients and we used a dichotomy method to obtain $\varepsilon_{1,2}$. In figure 5.27 we refine the calculations of $\Delta\varepsilon$ for large ν by computing the velocity with more iterations. As it may be noticed from this figure, when the number of iterations used is increased, *i.e.* the accuracy is increased, the behaviour of $\Delta\varepsilon$ tends to what we expect: $\Delta\varepsilon$ decreases, apparently to zero, as ν tends to 1.

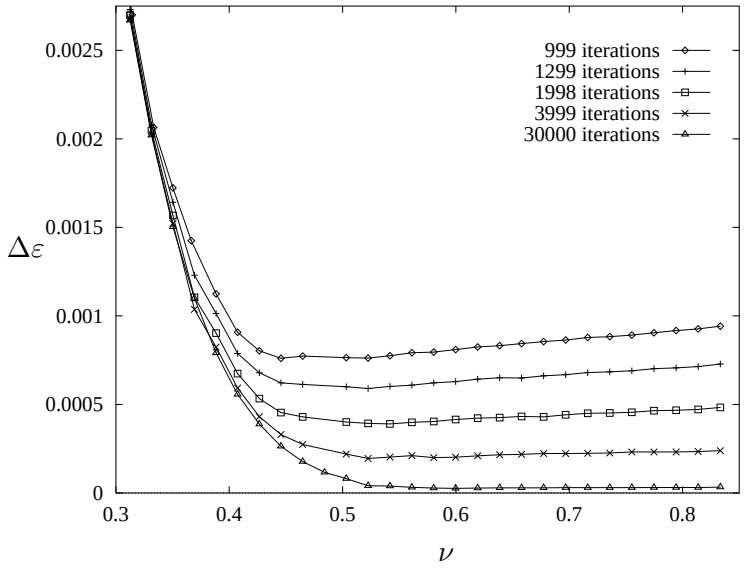

Figure 5.27: Size of the $v = 1/3$ plateau for the hyperbolic tangent local map as a function of ν for several number of iterations taken for computing the velocity. As the number of iterations is increased, one obtains a more precise result saying that the plateau tends to disappear as ν tends to one.

On the other hand, for $\nu < 0.11$ the plateau do not continue to get larger as ν tends to 0 since the $v = 0/1$ and $v = 1/1$ plateaus occupy a large portion of the ε-space, see figure 5.15. This is because $\varepsilon_c \to 0.5$ $(1 - \varepsilon_c \to 0.5)$ as $\nu \to 0$. In the limit when $\nu = 0$ the local map $f(x) = \tanh(x/\nu)$ is a square step (figure 5.28) and so is the velocity (*i.e.* $\varepsilon_c = 1 - \varepsilon_c = 0.5$). Therefore, for small ν, the non-trivial propagating region $\varepsilon_c < \varepsilon < 1 - \varepsilon_c$ becomes small and then, because of this space constraint, all the non-trivial plateaus $(0 < v(\varepsilon) < 1)$ shrink.

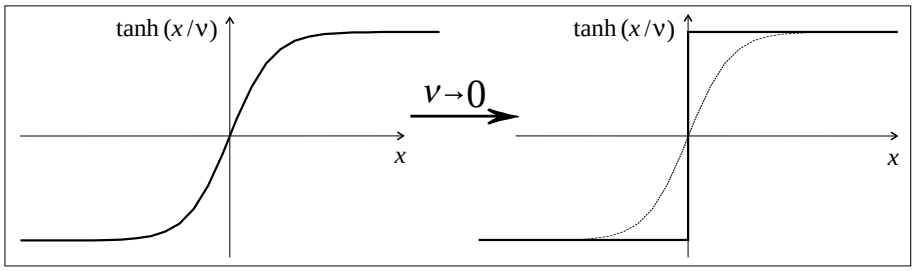

Figure 5.28: As ν tends to zero the hyperbolic tangent $\tanh(x/\nu)$ tends to a square step function. At the same time the velocity tends to a square step function.

The tendency of the plateaus to get smaller as the number of sites in the interface increases is due to the increasing constriction on the movement of sites. In a minimal 1-state the only site in the interface has its possible dynamics contained in the whole range $[x^*_-, x^*_+]$, whereas for a minimal N-state the story is quite different. As the number of sites in the interface is increased, the dynamics of each site is restricted to a smaller interval —as is schematically depicted in figure 5.29. Therefore, when the number of sites in the interface is very large one may think of the delay map of a single site in the interface as a small portion of the whole dynamics in $[x^*_-, x^*_+]$ and thus it has to be almost linear. This effect is the same as considering a sharp curve and focusing on a small portion (zooming in) where it may be approximated by a linear function.

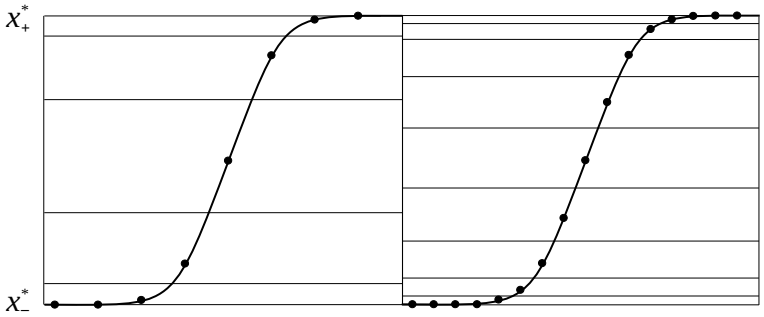

Figure 5.29: As the number of sites in the interface is increased the dynamics of each site is restricted to a smaller interval.

5.3.2 Mode-locking versus range of interaction

It should now be clear that by introducing more sites to the interface the mode-locking of the travelling velocity is diminished. In order to increase the number of sites in the interface we changed the shape of the local map; here we reverse this procedure by leaving the local map unchanged and by modifying the coupling interaction. Up to now we have dealt with CMLs with nearest neighbour coupling. We now consider a coupling with a broader range.

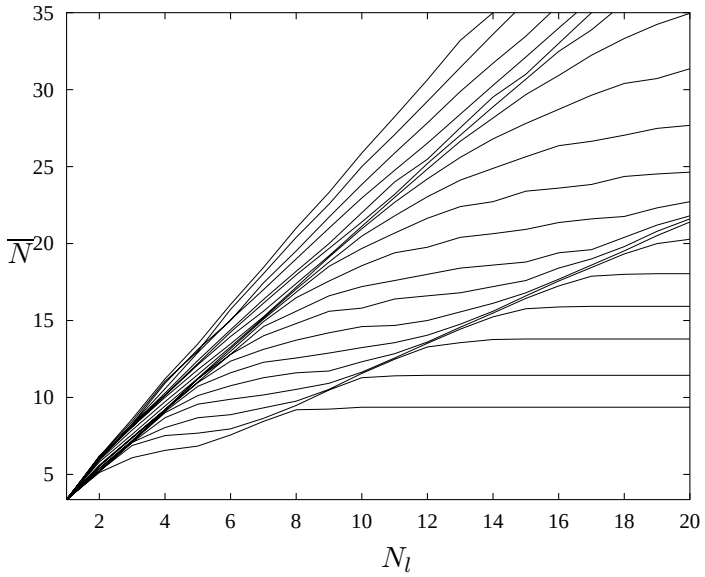

Figure 5.30: Average number of sites $\overline{N}$ in the interface $[x^*_- + \delta, x^*_+ - \delta]$ ($\delta = 10^{-10}$) as a function of the range of the coupling N_l for different values of the exponential decay $\tilde{\alpha}$ of the coupling ($\tilde{\alpha} = 0.05, 0.1, 0.15, \ldots, 1.0$ from bottom to top). We used the CML (5.5) with the tangent local map $f(x) = \tanh(7\,x)$ and with ε=0.45.

In the first chapter we introduced the general form of a homogeneous CML with l left neighbours and r right neighbours (cf. (0.4)). Let us consider one-way coupling ($r = 0$) with exponentially decreasing coupling coefficients ($\varepsilon_k = e^{-\alpha|k-1|}$). Normalizing the coupling

yields to the following one-way CML

$$x_{t+1}(i) = (1-\varepsilon) f(x_t(i)) + \frac{\varepsilon \sum_{k=1}^{N_l} e^{-\alpha|k-1|} f(x_t(i-k))}{\sum_{k=1}^{N_l} e^{-\alpha|k-1|}}, \tag{5.4}$$

where N_l is the number of left neighbours coupled and α is a non-negative real coefficient measuring the decay rate of the exponential coupling. For $N_l = 1$, equation (5.4) recovers the original form of a one-way CML (cf. (0.6)). From now on we will call N_l the *range* of the coupling. By defining the new parameter $\tilde{\alpha} = e^{-\alpha}$ equation (5.4) now reads

$$x_{t+1}(i) = (1-\varepsilon) f(x_t(i)) + \frac{\varepsilon \sum_{k=1}^{N_l} \tilde{\alpha}^{|k-1|} f(x_t(i-k))}{\sum_{k=1}^{N_l} \tilde{\alpha}^{|k-1|}}, \tag{5.5}$$

where $\tilde{\alpha} \in [0,1]$ gives a measure of the extent of the exponential coupling, *i.e.* small values of $\tilde{\alpha}$ correspond to rapid decay and values of $\tilde{\alpha}$ near 1 to slow decay.

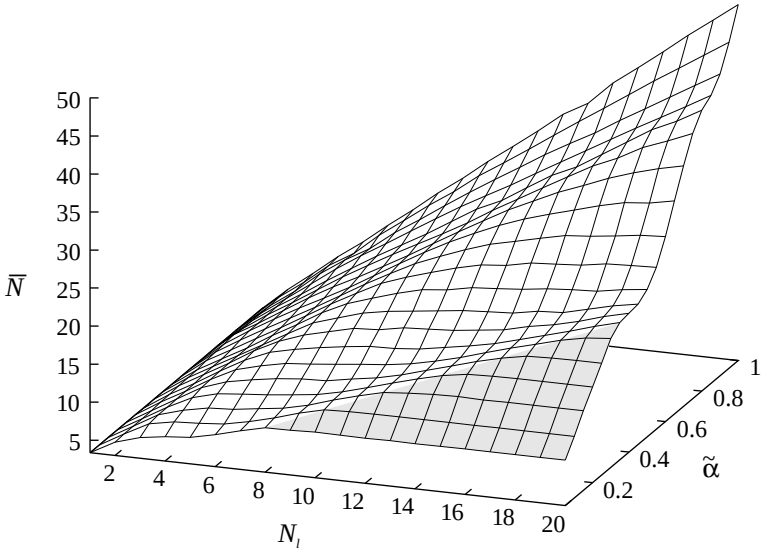

Figure 5.31: Average number of sites $\overline{N}$ in the interface as a function of the range of the coupling N_l and its exponential decay $\tilde{\alpha}$. We used the same parameters as in figure 5.30. The shaded area corresponds to the saturation region of $\overline{N}$.

In figure 5.30 we plotted the average number of sites $\overline{N}$ in the interface $[x^*_- + \delta, x^*_+ - \delta]$ ($\delta \ll 1$) as a function of the range of the coupling N_l for different values of the exponential decay $\tilde{\alpha}$ with $\varepsilon = 0.45$. The first observation is that, as expected, the number of sites in the interface increases as the number of coupled sites increases and as the exponential decay gets slower. On the other hand a very interesting phenomenon happens for the curves corresponding to $\tilde{\alpha} < 0.3$: $\overline{N}$ cease to increase for large N_l. The observed saturation of $\overline{N}$ for large N_l and small $\tilde{\alpha}$ is due to the fact that the exponential decay is so strong that far neighbours, even if N_l is large, do not contribute. In fact, for any value of $\tilde{\alpha}$ the same behaviour is observed but, obviously, the saturation point happens for larger N_l if ones

increases $\tilde{\alpha}$. In our figure we plotted $\overline{N}$ for $N_l \in [1, 20]$ and it is only possible to observe the saturation when $\tilde{\alpha} < 0.3$, for larger $\tilde{\alpha}$ the saturation occurs for values of N_l larger than 20. In figure 5.31 we present a 3-dimensional plot of $\overline{N}$ vs. N_l and $\tilde{\alpha}$ giving a global picture of the behaviour of $\overline{N}$.

From these figures one sees that it is possible to vary the number of sites in the interface by changing the range of the coupling and leaving the local map and the coupling parameter ε fixed. One could increase the number of sites in the interface by increasing $\tilde{\alpha}$ and/or increasing N_l —though one ought to be careful since only varying N_l could lead to saturation of $\overline{N}$ before reaching the desired value.

Now let us see the dependence of the size of the mode-locking plateaus as the number of sites in the interface is increased by means of increasing the range of the exponential coupling, *i.e.* by varying N_l. Take the CML with exponential coupling (5.5) with the hyperbolic tangent local map $f(x) = \tanh(x/\nu)$ with $\nu = 1/7$. We choose a slow exponential decay rate ($\tilde{\alpha} = 0.9$) in order to avoid saturation of the number of sites in the interface as N_l is increased. The results are shown in figure 5.32 where we plotted the velocity curves as a function of ε for different values of N_l. Before commenting on the width of the plateaus there are two interesting points worth to mention. First, since the coupling now involves N_l left neighbours it is possible for the velocity to be larger than 1 since the information could now propagate up to speeds equal to N_l; in fact, the maximum reachable velocity would be $v_{\max} = N_l$. In figure 5.32 all the curves for $N_l > 1$ reach a velocity greater than 1 for large ε.

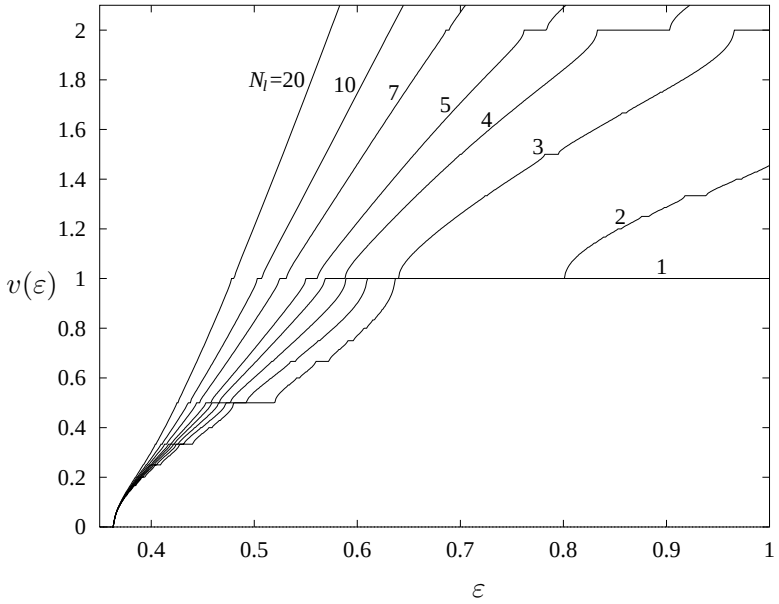

Figure 5.32: Effect of the range of the coupling N_l onto the mode-locking plateaus. For the experiment we took the CML (5.5) with the local map $f(x) = \tanh(7\,x)$ and with an exponential decay $\tilde{\alpha} = 0.9$, in order to avoid saturation of the number of sites in the interface. We averaged the velocity over 1 260 iterations after dropping 150 transients. The mode-locking plateaus clearly shrink as N_l is increased.

The maximum observed speed in our numerical computations was slightly larger than 6 for $N_l = 20$ when $\varepsilon = 1$, nevertheless it is possible to increase the velocity as much as desired by increasing N_l whilst being careful that $\tilde{\alpha}$ is large enough to avoid saturation of the number of sites in the interface. The second interesting point is that all the velocity curves take off

from zero at the same point, *i.e.* ε_c is independent of N_l and $\tilde{\alpha}$.

Now let us concentrate on the mode-locking plateaus in figure 5.32. First of all notice that there are mode-locked plateaus for velocities larger than 1. In this case the plateaus occur at $v = p/q$ where now $p > q$ and the same mode-locking mechanism as for $0 \leq v \leq 1$ prevails. The most important point to notice from this figure, for our purpose, is that the plateaus tend to shrink as the range of the coupling is increased. The plateaus corresponding to the principal mode-locking ratios, small denominator q, tend to prevail as N_l is increased —more evident plateaus in the figure. On the other hand, the plateaus corresponding to large denominator q, that are very small even for $N_l = 1$, are imperceptible, at least at the plotting scale, for large N_l (see for example the plateaus between $v = 1/2$ and $v = 1$). Therefore, we observed how the mode-locking tends to be diminished as the range of the coupling is increased. This tendency is caused by the same mechanism explained in the previous section, namely the fact that the mode-locking tends to disappear as the number of sites in the interface is increased —recall that by increasing N_l one is increasing the number of sites in the interface (cf. figures 5.30 and 5.31).

Chapter 6

Conclusions and final remarks

This thesis presents the analysis of coherent propagation of signals through bistable CMLs. By focusing our attention on the simplest propagating mechanism we discover a very peculiar phenomenon: the mode-locking of the travelling velocity with respect to the coupling parameter. We introduced a piece-wise linear local map in order to understand the mode-locking mechanism. This map allows us to select a parameter region for which there is only one site in the interface —sites of the signal lying between the two stable points of the local map. Thus it is possible to reduce the dynamics of the whole lattice to a one-dimensional map, the auxiliary map, that accounts for the dynamics of the single interfacial site. The auxiliary map is a map of the circle whose rotation number gives the travelling velocity of the interface. In this framework the velocity mode-locking is caused by a superstable region (the gap) of the auxiliary map which is responsible for collapsing nearby trajectories to the same periodic orbit. The mode-locking is shown to occur for every rational velocity stressing the fact that the piece-wise linear CML presents a very strong mode-locking reflected at any scale of the velocity graph. In other words, the graph of the velocity represents a Devil's staircase, a fractal staircase. The fractal structure of the Devil's staircase is described by means of a symbolic dynamics description of the auxiliary map orbit. The end points of the plateaus are given by envelopes corresponding to a Farey-like construction of the rationals using simple rules of symbolic sequences concatenations. Using this procedure one can find the symbolic sequence associated to a rational velocity by concatenating the symbolic sequences associated to the two previous Farey rationals to that particular velocity.

Even though the auxiliary map deals with signals with only one site in the interface, the mode-locking of its rotation number gives the first step towards the understanding of the mode-locking of the travelling velocity. For more general values of the local map parameters and coupling, the piece-wise linear CML propagates signals with more than one site in the interface, up to N in the case of a minimal N-state. The study of these minimal N-states could be approached by reducing the dynamics of the whole lattice to a N-dimensional map of the torus. For the piece-wise linear CML it is possible, in principle, to find such N-dimensional map. In this case the N-dimensional map of the torus possesses a N-dimensional gap that again collapses the orbits causing the generalized rotation number to be mode-locked to rational values as the coupling parameter is varied. Although this method is impossible to visualize in more than two dimensions it explains the mode-locking of the travelling velocity in a very straightforward manner.

The mode-locking phenomenon is not a particular feature of the piece-wise linear CMLs whose associated auxiliary map possesses a N-dimensional gap. The mode-locking is shown to appear in more general CMLs, one-way or diffusive, with smooth local maps. Inspired by the reduction of the dynamics on the piece-wise linear CML one may try to reduce the dynamics for the more general kinds of local maps. While the piece-wise linear map propagates signals with few sites in the interface, generic bistable CMLs give rise to signals with an infinite number of sites in the interface. The construction of the associated N-dimensional auxiliary map is then unpractical. Nevertheless we show how the reduction of the interface dynamics is possible via a delay map of a single site. This delay map plays the role of the auxiliary map and the mode-locking should be reflected in its dynamics. Interestingly, the delay map is a map of the circle and its rotation number gives the travelling velocity. The mode-locking of the travelling velocity is again a consequence of the mode-locking of the rotation number of the delay map. Although the basic mechanism for the mode-locking is the same as for the piece-wise linear CML there is one important subtlety. While the mode-locking in the piece-wise linear CML is built on the collapse of orbits induced by the gap of the auxiliary map, the mode-locking for a generic CML relies on the mode-locking of the rotation number through a purely nonlinear effect. The nonlinearity of the local map of a generic CML is inherited by the delay map and causes the rotation number to be mode-locked to rational values in a manner akin to rational mode-locking for circle maps. Therefore the mode-locking is more the rule rather than the exception in signal propagation through bistable CMLs.

The occurrence of velocity mode-locking in CMLs has not been reported in the literature before because generic CMLs could present the mode-locking at a microscopic scale and therefore not visible for the naked eye. In this work we relate the size of the mode-locking plateaus to the number of sites in the interface. The results show how the mode-locking tends to be diminished as the number of sites in the interface is increased. This effect is understood by considering the available dynamic space for each site in the interface: as the number of sites in the interface is increased, the available space for each site is reduced and therefore any nonlinear effect is diminished. The number of sites in the interface depends on the chosen local map, although it is possible to turn around the problem towards the range of the coupling of the CML. By coupling a larger number of neighbours it is possible to increase the number of sites in the interface and by those means abate the nonlinear mode-locking.

When coupling a large number of neighbouring sites one is approaching the continuum limit. In the limit, when the separation between sites tends to zero, it is possible to consider the discrete space signal as an approximation of the continuous case. The continuous analogue of these CMLs would be a particular class of partial differential equations (PDE). If one tries to solve numerically this class of PDEs one has to rely on discrete methods, such as the finite difference methods [14, 65]. Such methods are based on a space-time discretization, the result is a collection of sites, in one or more dimensions, coupled together via a deterministic formula resembling the structure of a CML. Thus when numerically solving this class of PDEs one is really iterating a discrete system and finding an approximate solution for the propagating front. Recall that the mode-locking of the travelling velocity in CMLs is a nonlinear effect strictly generated by the discrete nature of the space-time. Therefore one has to be careful when numerically solving PDEs since we are discretizing the space and one could introduce some spurious mode-locking of the travelling wave front, although the effect is expected not to be observed at macroscopic levels unless the discretization is too coarse. Nonetheless, as observed in the numerical experiments showed in section 5.3, the mode-locking tends to disappear as we approach the continuum limit.

The mode-locking occurrence in CMLs provides structural stability of the travelling velocity. It may be very important in systems under the influence of external noise to be able to rely on a specific travelling velocity. The mode-locking enables the travelling velocity to remain mode-locked, *i.e.* constant, under the presence of external noise. The amount of external noise to be applied in order to displace the travelling velocity out from a mode-locked plateau depends on the size of the latter. The more structurally stable cases for a particular choice of local map and coupling are the plateaus corresponding to the principal mode-locking ratios given by Farey series of low order. On the other hand, if we think of the mode-locking mechanism as a spurious effect one could try, on top of changing the local map and increasing the range of the coupling, to take values of the coupling parameter such that the resulting travelling velocity is near an irrational. In doing so we are choosing a velocity whose approximation by a rational gives a large denominator and thus it corresponds to a microscopic plateau.

We expect this kind of velocity mode-locking to occur in a widespread range of nonlinear coupled systems. Coupling together different subsystems could give rise to an information propagation through the whole system. From the work presented here one could expect mode-locking of the mean information velocity propagation to happen with respect to some of the coupling parameters. This could be helpful in trying to understand existing mode-locking behaviour of coupled systems as well as to design new coupled systems with structural stability of the information propagation velocity under the influence of external noise.

References

[1] K. Kaneko, editor. *Theory and applications of coupled map lattices.* John Wiley & Sons 1993.

[2] E. Atlee Jackson. *Perspective of nonlinear dynamics.* Volume 2, Cambridge Univ. Press1991. Chap. 10.

[3] D. Keeler and J.D. Farmer. Robust space-time intermittency and $1/f$ noise. *Physica D* **23** (1986) 413–435.

[4] V.M. Gundlach and D.A. Rand. Spatio-temporal chaos. *Nonlinearity* **6** (1993) 165–230.

[5] L.A. Bunimovich, A. Lambert and R. Lima. The emergence of coherent structures in coupled map lattices. *J. Stat. Phys.* **61** (1990) 253.

[6] L. Ying-Cheng and C. Grebogi. Synchronization of spatiotemporal chaotic systems by feedback control. *Phys. Rev. E* **50** (1994) 1894–1899.

[7] R. Kapral and G.-L. Oppo. Competition between stable states in spatially-distributed systems. *Physica D* **23** (1986) 455–463.

[8] R. Kapral, R. Livi, G.-L. Oppo and A. Politi. Dynamics of complex interfaces. *Phys. Rev. E* **49**, 3 (1994) 2009–2022.

[9] K. Kaneko. Chaotic travelling waves in a coupled map lattice. *Physica D* **68** (1993) 299–317.

[10] R.E. Amritkar, P.M. Gade and A.D. Gangal. Stability of periodic orbits of coupled map lattices. *Phys. Rev. A* **44**, 6 (1991) 3407–3410.

[11] P.M. Gade and R.E. Amritkar. Spatially periodic orbits in coupled map lattices. *Phys. Rev. E* **47**, 1 (1993) 143–153.

[12] H. Chaté and P. Manneville. Coupled map lattices as cellular automata. *J. Stat. Phys.* **56**, 3/4 (1989) 357–370.

[13] H. Chaté and P. Manneville. Using coupled map lattices to unveil structures in the space of cellular automata. *Springer proceedings in physics, Cellular automata and modeling of complex physical systems* **46** (1990) 298–309.

[14] A.R. Mitchell and D.F. Griffiths. *The finite difference method in partial differential equations.* John Wiley & Sons1980.

[15] K. Kaneko. Transition from torus to chaos accompanied by frequency lockings with symmetry breaking. *Prog. Theor. Phys.* **69**, 5 (1983) 1427.

[16] K. Kaneko. Period-doubling of kink-antikink patterns, quasiperiodicity in anti-ferro-like structures and spatial intermittency in coupled logistic lattice. *Prog. Theor. Phys.* **72**, 3 (1984) 480–486.

[17] S. Yukawa and M. Kikuchi. Density fluctuations in traffic flow. Preprint, 1996.

[18] H. Leung and T. Lo. A spatial temporal dynamical model for multipath scattering from the sea. *IEEE Transactions on Geoscience and Remote Sensing* **33**, 2 (1995) 441–448.

[19] M.P. Hassell, O. Miramontes, P. Rohani and R.M. May. Appropriate formulations for dispersal in spatially structured models. *Journal of Animal Ecology* **64** (1995) 662–664.

[20] R.V. Solé and J. Bascompte. Measuring chaos from spatial information. *J. theo. Biol.* **175** (1995) 139–147.

[21] D.A. Rand. Measuring and characterizing spatial patterns, dynamics and chaos in spatially extended dynamical systems and ecologies. *Phil. Trans. R. Soc. Lond. A* **348** (1994) 497–514.

[22] D.A. Rand and H.B. Wilson. Using spatio-temporal chaos and intermediate-scale determinism to quantify spatially extended ecosystems. *Proc. R. Soc. Lond. B* **259** (1995) 111–117.

[23] A.V. Holden and H. Zhang. Modelling propagation and re-entry in anisotropic and smoothly heterogeneous cardiac tissue. *J. Chem. Soc. Faraday. Trans.* **89**, 15 (1993) 2833–2837.

[24] G. Martinez-Mekler, G. Cocho, A. Gelover-Santiago and R. Bulajich. Modelling genetic evolution with coupled map lattices. *Revista Mexicana de Física* **38**, 1 (1992) 127–141.

[25] G. Cocho, A. Gelover-Santiago, G. Martinez-Mekler and A. Rodin. Nonlinear modeling of the aids virus genetic sequence evolution. *Int. J. Modern Phys. C* **5**, 2 (1994) 321–324.

[26] A.V. Holden, J.V. Tucker, H. Zhang and M.J. Poole. Coupled map lattices as computational systems. *Chaos* **2**, 3 (1992) 367–375.

[27] T. Yanagita and K. Kaneko. Coupled map lattice model for convection. *Phys. Lett. A* **175** (1993) 415–420.

[28] K. Kaneko. Spatiotemporal chaos in one- and two-dimensional coupled map lattices. *Physica D* **37** (1989) 60–82.

[29] C. Beck. Chaotic cascade model for turbulent velocity distribution. *Phys. Rev. E* **49**, 5 (1994) 3641–3652.

[30] F.H. Willeboordse and K. Kaneko. Pattern dynamics of a coupled map lattice for open flow. *Physica D* (1995) 101–128.

[31] K. Kaneko. Spatial Period-doubling in open flow. *Phys. Lett.* **111**, 7 (1985) 321–325.

[32] P.M. Gade and R.E. Amritkar. Wavelength-doubling bifurcations in one-dimensional coupled logistic maps. *Phys. Rev. E* **49**, 4 (1994) 2617–2622.

[33] Q. Zhilin and H. Gang. Spatiotemporally periodic states, periodic windows, and intermittency in coupled map lattices. *Phys. Rev. E* **49**, 2 (1994) 1099–1108.

[34] Q. Zhilin, H. Gang, M. Benkun and T. Gang. Spatiotemporally periodic patterns in symmetrically coupled map lattices. *Phys. Rev. E* **50**, 1 (1994) 163–170.

[35] B. Fernandez. Existence and stability of steady fronts in bistable CML. Preprint, 1995.

[36] R.S. MacKay and J.-A. Sepulchre. Multistability in networks of weakly coupled bistable units. *Physica D* **82** (1995) 243–254.

[37] S. Aubry and G. Abramovici. Chaotic trajectories in the standard map. The concept of anti-integrability. *Physica D* **43** (1990) 199–219.

[38] R.S. MacKay. Dynamics of Networks: Features which persist from the uncoupled limit. Preprint, 1996.

[39] B. Fernandez. Kinks dynamics in one-dimensional coupled map lattices. Preprint, 1995.

[40] S.N. Chow and W. Shen. Stability and bifurcation of travelling wave solutions in coupled map lattices. Preprint, 1994. (ftp://ftp.math.gatech.edu/pub/preprints/CDSNS/-94-177.ps.Z)

[41] A. Nitzan, P. Ortoleva and J. Ross. Nucleation in systems with multiple stationary states. *Faraday Symposium of the Chemical Society* **9** (1974) 241–251.

[42] A.M. Albano, N.B. Abraham, D.E. Chyba and M. Martelli. Bifurcations, propagating solutions and phase transitions in nonlinear chemical reactions. *Am. J. Phys.* **52**, 2 (1984) 161–167.

[43] J.S. Rowlinson and B. Windom. *Molecular theory of capillarity.* Clarendon, Oxford 1982.

[44] R. Carretero-González, D.K. Arrowsmith and F. Vivaldi. Reduction dynamics for travelling fronts in coupled map lattices. In preparation, 1997.

[45] V.S. Afraimovich, S.N. Chow and W. Shen. Hyperbolic homoclinic points of $\mathbb{Z}^d$-actions in lattice dynamical systems. *Int. J. Bifurcation and Chaos* **6**, 6 (1996) 1059–1075.

[46] S.N. Chow and J. Mallet-Paret. Pattern Formation and Spatial Chaos in Lattice Dynamical Systems. *IEEE Transactions on circuits and systems I* **42**, 10 (1995) 746–751.

[47] S.N. Chow, J. Mallet-Paret and E.V. Vleck. Dynamics of lattice differential equations. *Int. J. Bifurcation and Chaos* **6**, 9 (1996) 1605–1621.

[48] F. Schlögl and R.S. Berry. Small roughness fluctuations in the layer between two phases. *Phys. Rev. A* **21**, 6 (1980) 2078–2081.

[49] W.V. Saarloos. Front propagation into unstable states: Marginal stability as a dynamical mechanism for the velocity selection. *Phys. Rev. A* **37**, 1 (1988) 211–229.

[50] J.M. Gambuado, O Lanford and C. Tresser. Dynamique symbolique des rotations. *C. R. Acad. Sc. Paris* **299 I**, 16 (1984) 823–826.

[51] P. Veerman. Symbolic dynamics and rotations numbers. *Physica A*, **134** (1986) 543–576.

[52] R.L. Devaney. *An introduction to dynamical systems.* Addison-Wesleysecond edition, 1989.

[53] P. Glendinning. Bifurcations and rotation numbers for maps of the circle associated with flows on the torus and models of cardiac arrhythmias. *Dynamics and Stability of Systems* **10**, 4 (1995) 367–386.

[54] E.A. Coddington and N. Levinson. *Theory of ordinary differential equations.* Mc Graw-Hill1955.

[55] J.H. Hubbard and C.T. Sparrow. The classification of topologically expansive Lorenz maps. *Comm. on Pure and Appl. Maths.* **43** (1990) 431–443.

[56] P.A. Glendinning and C.T. Sparrow. Prime and renormalizable kneading invariants and the dynamics of expanding Lorenz maps. *Physica D* **62** (1993) 22–50.

[57] G.L. Baker and J.P. Gollub. *Chaotic Dynamics, an introduction.* Cambridge Univ. Press1990. Chap. 4.

[58] P. Bak. The Devil's staircase. *Physics Today* December (1986) 38–45.

[59] M. Schroeder. *Fractals, Chaos, Power Laws.* W.H. Freeman and Company 1991. Chap. 7.

[60] J.J.P. Veerman. Hausdorff dimension of order preserving sets. *Commun. Math. Phys.*, **127** (1990) 313–317.

[61] R.L. Graham, D.E. Knuth and O. Patashnik. *Concrete mathematics, a foundation for computer science.* Addison-Wesley1989. Chap. 4.5.

[62] G.H. Hardy and E.M. Wright. *An introduction to the theory of numbers.* Cambridge Univ. Press4$^{\text{th}}$ edition, 1960. Chap. 3.

[63] C. Baesens, J. Guckenheimer, S. Kim and R.S. Mackay. Three coupled oscillators: mode-locking, global bifurcations and toroidal chaos. *Physica D* **49** (1991) 387–475.

[64] Y.L. Maistrenko, V.L. Maistrenko, S.I. Vikul and L.O. Chua. Bifurcations of attracting cycles from the delayed Chua's circuit. *Int. J. Bifurcation and Chaos* **5**, 3 (1995) 653–671.

[65] G.D. Smith. *Numerical solution of partial differential equations: finite difference methods.* Oxford Univ. Presssecond edition, 1978.